Mathematical tools and signal processing algorithms for the study of gravitational waves polarization

Cyril Cano

Université Grenoble Alpes

THÈSE

Pour obtenir le grade de

DOCTEUR DE L' UNIVERSITÉ GRENOBLE ALPES

Spécialité : **SIGNAL IMAGE PAROLE TELECOMS**

Arrêté ministériel : 25 mai 2016

Présentée par

Cyril CANO

Thèse dirigée par **Nicolas LE BIHAN**, Directeur de recherche, CNRS, Gipsa-lab, Université Grenoble Alpes et
codirigée par **Éric CHASSANDE-MOTTIN**, Directeur de recherche, CNRS, APC, Université Paris Cité

préparée au sein du **Laboratoire Grenoble Images Parole Signal Automatique**
dans **l'École Doctorale Electronique, Electrotechnique, Automatique, Traitement du Signal (EEATS)**

Outils mathématiques et de traitement du signal pour l'étude polarimétrique des ondes gravitationnelles

Mathematical tools and signal processing algorithms for the study of gravitational waves polarization

Thèse soutenue publiquement le **28 octobre 2022**,
devant le jury composé de :

Monsieur Nicolas LE BIHAN
Directeur de recherche, CNRS, Gipsa-lab, Directeur de thèse
Monsieur Éric CHASSANDE-MOTTIN
Directeur de recherche, CNRS, APC, Co-Encadrant de thèse
Monsieur André FERRARI
Professeur des universités, Université Côte d'Azur, Rapporteur
Monsieur Antoine ROUEFF
Professeur des universités, Université de Toulon, Rapporteur
Monsieur Olivier MICHEL
Professeur des universités, Université Grenoble Alpes, Président
Madame Sandrine ANTHOINE
Chargée de recherche, CNRS, I2M, Examinatrice
Monsieur Stanislav BABAK
Directeur de recherche, CNRS, APC, Examinateur
Monsieur Julien FLAMANT
Chargé de recherche, CNRS, CRAN, Invité

Thèse de doctorat

Spécialité Signal, Image, Parole, Télécom

Outils mathématiques et de traitement du signal pour l'étude polarimétrique des ondes gravitationnelles

Cyril Cano

Jury:

Directeur de thèse
Nicolas Le Bihan, Directeur de recherche, CNRS, Gipsa-lab

Co-directeur de thèse
Éric Chassande-Mottin, Directeur de recherche, CNRS, APC

Rapporteur
André Ferrari, Professeur des universités, Université Côte d'Azur

Rapporteur
Antoine Roueff, Professeur des universités, Université de Toulon

Examinateur
Stanislav Babak, Directeur de recherche, CNRS, APC

Examinatrice
Sandrine Anthoine, Chargée de recherche, CNRS, I2M

Examinateur
Olivier Michel, Professeur des universités, Université Grenoble Alpes

Invité
Julien Flamant, Chargé de recherche, CNRS, CRAN

Université Grenoble Alpes
28 octobre 2022

Résumé

Cette thèse est un projet interdisciplinaire visant à proposer de nouvelles méthodologies et de nouveaux algorithmes pour caractériser la polarisation des signaux non-stationnaires polarisés et à appliquer ces nouveaux outils au contexte de l'astronomie des ondes gravitationnelles. L'observation directe des ondes gravitationnelles rendue possible par les détecteurs avancés LIGO et Virgo constitue un changement de paradigme pour l'étude des objets astrophysiques compacts tels que les trous noirs et les étoiles à neutrons. L'analyse du grand volume de données provenant de ces détecteurs s'est jusqu'à présent concentrée sur la morphologie de la forme d'onde enregistrée, à partir de laquelle des informations sur la nature de la source peuvent être extraites. La polarisation des ondes a reçu moins d'attention car le nombre de détecteurs était insuffisant pour tirer des conclusions précises. Cependant, l'information de polarisation présente un intérêt pour certaines sources astrophysiques. Par exemple, pour les fusions de systèmes binaires d'étoiles compactes, la précession du plan orbital se traduit par une évolution spécifique du schéma de polarisation. Cette thèse part des aspects théoriques fondamentaux de la représentation et la caractérisation des signaux polarisés pour ensuite développer des outils d'analyse et de synthèse adaptés au contexte de l'application considérée. Les résultats présentés sont de trois ordres. Les différentes représentations des signaux modulés en amplitude, en fréquence et en polarisation d'abord sont passées en revue, en évaluant leur utilité pour l'analyse et la synthèse de ces signaux. Cette revue met en lumière les problèmes causés par la dégénérescence de certaines représentations, précise les conditions d'apparition de celle-ci et propose des moyens d'y remédier. Sur la base de cette étude, des modèles génératifs d'apprentissage automatique sont construits, et appliqués au calcul rapide de forme d'ondes gravitationnelles, permettant ainsi l'accélération de l'inférence des paramètres des sources. Ce modèle génératif est proposé à la fois pour les sources de trous noirs binaires sans précession et avec précession, et sa précision est évaluée dans chaque cas. Finalement, de nouveaux principes de régularisation basés sur des a priori de polarisation sont introduits afin d'améliorer la reconstruction des deux composantes du signal à partir des données observationnelles. La méthode est évaluée sur des données synthétiques réalistes. Elle permet de cibler l'analyse sur certaines catégories de source associées à une polarisation particulière.

Mots Clés: Polarisation - Traitement statistique du signal - Ondes gravitationnelles

Abstract

This thesis is an interdisciplinary project aiming at proposing new methodologies and algorithms to characterize the polarization of non-stationary polarized signals and to apply these new tools to the context of gravitational wave astronomy. The direct observation of gravitational waves made possible by the advanced LIGO and Virgo detectors constitutes a paradigm shift for the study of compact astrophysical objects such as black holes and neutron stars. Analysis of the large volume of data from these detectors has so far focused on the morphology of the recorded waveform, from which information about the nature of the source can be extracted. The polarization of the waves has received less attention because the number of detectors was insufficient to draw accurate conclusions. However, polarization information is of interest for some astrophysical sources. For example, for mergers of compact binary star systems, the precession of the orbital plane results in a specific evolution of the polarization pattern. This thesis starts from the fundamental theoretical aspects of the representation and characterization of polarized signals to develop analysis and synthesis tools adapted to the context of the considered application. The results presented are of three kinds. First, the different representations of amplitude, frequency and polarization modulated signals are reviewed, evaluating their usefulness for the analysis and synthesis of these signals. This review highlights the problems caused by the degeneracy of certain representations, specifies the conditions of its occurrence and proposes ways to remedy it. On the basis of this study, generative machine learning models are built, and applied to the fast computation of gravitational waveforms, thus allowing the acceleration of the inference of the source parameters. This generative model is proposed both for binary black hole sources without precession and with precession, and its accuracy is evaluated in each case. Finally, new regularization principles based on polarization a priori are introduced to improve the reconstruction of the two signal components from observational data. The method is evaluated on realistic synthetic data. It allows to target the analysis on certain source categories associated with a particular polarization.

Keywords: Polarization - Statistical signal processing - Gravitational waves

Remerciements

Les travaux de cette thèse s'inscrivent dans le cadre d'une collaboration ayant débuté avec Éric Chassande-Mottin, Nicolas Le Bihan, Pierre Chainais, Julien Flamant et Fangchen Feng sur le sujet de l'analyse polarimétrique des ondes gravitationnelles. Je tiens à remercier chacun d'entre eux pour leur accueil et leur avis éclairés, du stage de master au doctorat. Je suis heureux que cette collaboration soit désormais organisée autour du projet ANR RICOCHET. Je pense ne pas me tromper en prédisant que de ce projet découlerons des résultats originaux et particulièrement intéressants, autant pour la communauté signal que pour les différents cadres applicatifs envisagés.

À Nicolas et Éric, un grand merci pour m'avoir permis de réaliser ce travail et m'avoir accompagné durant ces trois années. Ce fut non pas seulement une collaboration scientifique, mais surtout une initiation à tous les aspects de la recherche. Un de mes plus grands plaisirs aura été d'avoir les ondes gravitationnelles comme sujet d'étude ainsi que d'intégrer la collaboration Virgo. Merci pour le temps passé à la préparation de mes présentations, aux retours sur le manuscrit et tous les autres conseils. J'espère que nous continuerons d'échanger sur les problématiques soulevées dans cette thèse.

Merci aux enseignants d'Aix-Marseille Université m'ayant transmis leur amour pour les mathématiques en addition de connaissances fondamentales lors de mon parcours universitaire. En particulier, je suis heureux que l'équipe Signal de l'I2M eu été représentée dans le jury par Sandrine Anthoine. Merci à Bruno Torrésani pour avoir contacté quelques-unes des personnes citées précédemment et m'avoir permis d'avoir l'opportunité de faire cette thèse.

Merci aux rapporteurs Antoine Roueff et André Ferrari, ainsi qu'à Stanislav Babak, Sandrine Anthoine et Olivier Michel d'avoir accepté et pris le temps d'examiner ce travail. Je tiens à vous remercier pour la qualité des échanges lors de la soutenance et pour votre bienveillance.

Un grand merci à mes collègues du Gipsa-lab, pour les discussions, les conseils et les repas partagés. Même si cela ne représente qu'un paragraphe, c'est bien ici que le plus de personnes doivent être remerciées. Merci aux doctorants de ma génération, Gaëlle, Sara, Roza, Yigit, Tayeb, Charles et les autres doctorants et post-doctorants du Gipsa-lab, ainsi que ceux rencontrés à l'APC. Comme il n'est pas souhaitable de faire une liste exhaustive de noms, je remercie chaleureusement toutes les personnes qui ont de près ou de loin participé à cette aventure.

Merci à mes parents, vous m'avez conduit jusqu'ici. Merci à ma sœur, pour l'inspiration apporté par ta carrière sportive au plus haut niveau. Merci à ma fiancée, Célia, pour tout.

Contents

Introduction

Multivariate signals are ubiquitous in physical science, whenever several quantities are related and jointly measured, and for which interrelations between coupled observables are often governed by physical phenomena. A central topic in data science is to represent and extract the common information of the two variables. The case of bivariate signals is of particular interest. Those appear in many fields, such as oceanography (position of freely-drifting instruments), optics (transverse coordinates of the electric field) and seismology (horizontal and vertical ground velocities), to name but a few.

The notion of polarization, usually used for waves, lies in a geometrical description of the intercorrelation of the two variables. By analogy with optics, the same notion is used to describe trajectories of an oscillatory bivariate signal in a 2D plane. A worth noticing example is that of gravitational waves. Those are perturbations of spacetime metric due to the coalescence of astrophysical compact bodies, e.g. black holes and neutron stars. Gravitational waves are characterized by two degrees of freedom, forming a non stationary bivariate signal whose properties depend on the source dynamics.

The direct observation of gravitational waves made possible by the advanced LIGO and advanced Virgo detectors constitutes a paradigm shift for the study of compact astrophysical objects such as black holes and neutron stars. The analysis of the large volume of data from these detectors has so far focused on the gravitational waveform morphology from which information about the nature of the source can be extracted. The polarization of the waves has received less attention because the number of detectors was insufficient to draw precise conclusions. To fully characterize the two polarizations predicted by the Theory of General Relativity, it is necessary to observe the gravitational wave signal with, at least three detectors, each collecting a substantial signal-to-noise ratio, which has not been the case so far. This situation will change in the near future with the improved sensitivity of LIGO and Virgo and the inception of new detectors (KAGRA in Japan and LIGO India). It will then become possible to measure the polarization of gravitational waves, allowing the exploration of new astrophysical questions.

This thesis, at the interface between data science and astrophysics, aims at proposing new methodologies and algorithms to characterize the polarization of non stationary bivariate signals and apply those tools to the context of gravitational-wave astronomy. The goal is to build new techniques to infer on the dynamics of the sources. For the mergers of binary compact star systems, a primary source of gravitational waves, this is of interest for investigating dynamical phenomena such as the presence of precession of the orbital plane which results in a specific evolution of the polarization pattern. Extracting this information can therefore help to understand the formation mechanisms of these sources.

The field of the polarimetric analysis of non stationary bivariate signals is still not well developed and a wide range of tools remain to be imagined and built along this avenue. In this topic, and by means of a newly introduced quaternion formalism, the representation problem of non stationary bivariate signals is addressed. From this study, a generative model of surrogate gravitational waveform is proposed in order to shorten the inference of the

source parameters. The reconstruction method is proposed, adding polarization constraint when reconstructing a bivariate signal. A polarimetric analysis of gravitational waves is conducted, showing that gravitational waves are a sum of non stationary components whose polarizations depend on the line of sight of the observer with respect to the orbital plane. A polarization modulation is thus found to be characteristic of the precession of the orbital plane. Based on this status and from the perspective of detecting a precession phenomenon, statistics are constructed to measure the detectability of precession effects on the waveform.

This thesis is organized in four chapters.

- Chapter 1 reviews several representations of amplitude, frequency and polarization modulated bivariate signals (AM-FM-PM signals) through quaternion formalism, regarding possible interpretations and ambiguities when trying to estimate the related parameters. Expressions of the instantaneous frequency and first instantaneous moments of the quaternionic Fourier transform are given for a generic AM-FM-PM signal. A non degenerate interpretable parameterization of AM-FM-PM signals is presented.

- Chapter 2 provides the basics of gravitational-wave astronomy, going from notions of general relativity and detector design, to actual and future observations.

- Chapter 3 relates to the fast and accurate generation of gravitational waveforms through machine learning algorithms. Based on a judicious choice of waveform attributes, two generative models are proposed for different cases of coalescing compact binaries.

- Chapter 4 addresses the polarimetric analysis of gravitational-wave signals. A regularization term is introduced in order to incorporate a polarization-based prior when reconstructing a bivariate signal. An application is given on a realistic gravitational-wave simulated signal. It is shown that gravitational waveforms are the sum of AM-FM-PM signals whose parameters are derived. Finally, indicators are built in order to quantify the measurability of the polarization state of a signal embedded in an additive Gaussian noise and to quantify the detectability of precession-induced polarization modulations.

1 Non-stationary bivariate signals analysis

1.1 Introduction

Bivariate signals are a particular case of multivariate signals. They can be represented as complex signals[1] $z(t) = x(t) + \boldsymbol{i}y(t)$ with given real and imaginary components $x(t)$ and $y(t)$. Such signals appear in many applications e.g. optics, seismology, oceanography and in many area of physics. A domain of specific interest to this thesis is gravitational-wave astronomy. A simulated gravitational wave is presented in Figure 1.1. In all of these applications there is a notion of common information carried by the two oscillatory components. This common information is embedded in cross-correlations between x and y such that it can only be accessed by a joint analysis of the two components.

1: We could have considered a real valued vectorial signal $z(t) = [x(t), y(t)]^T$, where the subscript T denotes the vector transpose, since the two representations are isomorphic. Of course, depending on the representation, analysis methods will not be the same. This will be discussed thereafter.

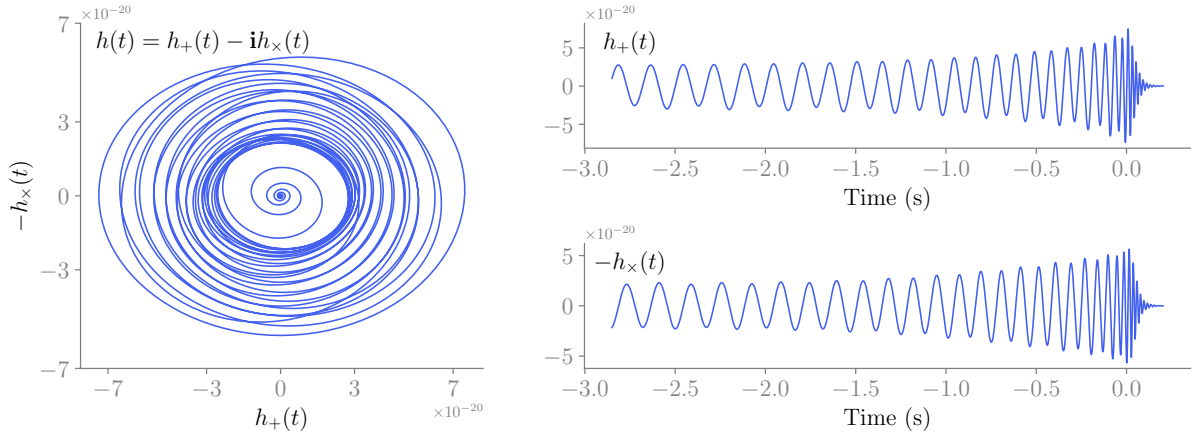

Figure 1.1: Simulated gravitational wave $h(t) \in \mathbb{C}$ from a precessing black hole binary. $t = 0$ corresponds to the merger of the two objects. Gravitational waves are bivariate signals evolving on (possibly) time varying ellipses. At each time the shape of the ellipse is fully determined by the orientation of the orbital plane with respect to the observer. Precession is a physical phenomenon which corresponds to variations of the orbital plane inducing variations of the elliptic trajectory. In Section 1.1.2 such signal is called an amplitude, frequency and polarization modulated signal.

The fact that bivariate signals can be represented in the complex plane allows a geometric interpretation. In this chapter we develop a bivariate signal analysis framework based on a geometric interpretation. We address question related to the representation of bivariate signals, and their computation.

Our interpretation is related to the concept of polarization, which connects to the oscillation of transverse waves such

as electromagnetic waves [1]. The polarization of an electromagnetic wave is a property linked to its direction or mode of oscillation in the plane transverse to the propagation direction. For example, polarized light waves oscillating along a single direction in the transverse plane are said to be linearly polarized. Waves oscillating along two different directions are elliptically or circularly polarized, depending on the angle between the axes along which the field oscillates. Thanks to this connection to wave optics we can benefit from the theoretical development in the domain of physics as we will see later.

[1]: Brosseau (1998), *Fundamentals of polarized light : a statistical optics approach*

The concept of polarization has been formalized for stochastic bivariate signals in [2]. In this chapter we concentrate on deterministic signals. We use a recently introduced formalism which enables to extend classical notions of real-valued non-stationary signal analysis to the bivariate case [3].

[2]: Schreier et al. (2010), *Statistical Signal Processing of Complex-Valued Data: The Theory of Improper and Noncircular Signals*

[3]: Flamant (2018), *A general approach for the analysis and filtering of bivariate signals*

1.1.1 Monochromatic bivariate signals

The simplest case of oscillatory bivariate signal is certainly the case of a monochromatic bivariate signal such as monochromatic light wave. Usual examples of monochromatic signals come from the family of pure harmonic oscillations (real-valued, univariate)

$$x(t) = a \cos \varphi(t) \tag{1.1}$$

and the associated complex-valued, bivariate wave

$$z(t) = a e^{i\varphi(t)} \tag{1.2}$$

with $\varphi(t) = \omega_0 t + \varphi_0$. For both $x(t)$ and $z(t)$, $a > 0$ is said to be the amplitude of the waveform, ω_0 its (angular) frequency and φ_0 its initial phase.

The concept of polarization allows to interpret the former and the latter in a unified manner as two respectively linear[2] and circular polarized signals carrying the same frequency ω_0. Expressions "linear" and "circular" are associated to the trajectory of these signals in the complex plane. From now on and by analogy with optics, we refer to complex elliptical signals[3] as polarized signals.

2: This can be done considering $x(t)$ as a complex signal with a constant imaginary part $\Im\{x(t)\} = 0$.

3: That is, signals with elliptical trajectory in the complex plane, either if the trajectory is constant over time (which is the case in this section) or if it is a local property (as presented in Section 1.1.2).

Definition 1.1.1 *We define the general model of monochromatic polarized signal as the following:*

$$z(t) = ae^{i\theta}\left(\cos\chi\cos\varphi(t) + \boldsymbol{i}\sin\chi\sin\varphi(t)\right) \in \mathbb{C} \tag{1.3}$$

where the constant triplet $[a,\ \theta,\ \chi]$ *lies in*

$$\mathbb{R}_+ \times \left[-\frac{\pi}{2},\ \frac{\pi}{2}\right[\times \left[-\frac{\pi}{4},\ \frac{\pi}{4}\right] \tag{1.4}$$

and $\varphi(t) = \omega_0 t + \varphi_0 \in \mathbb{R}$.

Definition 1.1.1 generalizes the case of monochromatic univariate signal. It defines a variety of signals with various trajectories in the complex plane. For a given frequency ω_0, different values of a, θ and χ correspond to different elliptical trajectories in the complex plane. They correspond to monochromatic polarized signals with the same angular speed $\dot{\varphi}(t)$ but different polarizations (different ellipses).

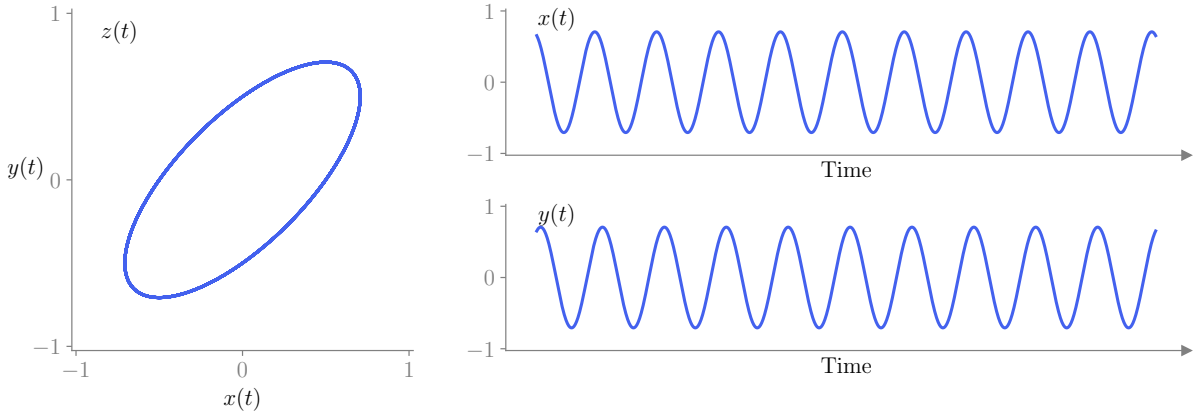

Figure 1.2: Monochromatic polarized signal $z(t) = x(t) + \boldsymbol{i}y(t)$ generated with (1.5). This signal has a fixed elliptical trajectory defined by the triplet $[a,\ \theta,\ \chi]$. The time-varying phase $\varphi(t)$ determines the position of $z(t)$ on the ellipse.

Figure 1.2 illustrates the trajectory of a monochromatic polarized signal in the complex plane generated for

$$a = 1,\ \theta = \frac{\pi}{4},\ \chi = \frac{\pi}{8} \quad \text{and} \quad \varphi(t) = 20\pi t. \tag{1.5}$$

The trajectory of such signal is elliptic and the newly introduced parameters θ and χ define the orientation and the shape of the ellipse as presented in Figure 1.3. For $\theta = \chi = 0$ we end up with the real valued monochromatic model (1.1). For $\chi = \pi/4$ we get the associated monochromatic complex wave $z(t) = ae^{i\varphi(t)}$ such that Definition 1.1.1 generalizes the previous cases of monochromatic signals. a, θ and χ are respectively the amplitude, the orientation and the ellipticity

of $z(t)$. a corresponds to the size of the scanned ellipse, θ is the orientation of its great axis and χ correspond to its shape. $\varphi(t)$ is the instantaneous phase of $z(t)$ which is the position of $z(t)$ with respect to the great axis. ω_0 is the rate at which the ellipse is scanned. Fixing $\omega_0 > 0$, $z(t)$ is said to be counterclockwise circular if $\chi > 0$ and clockwise circular if $\chi < 0$.

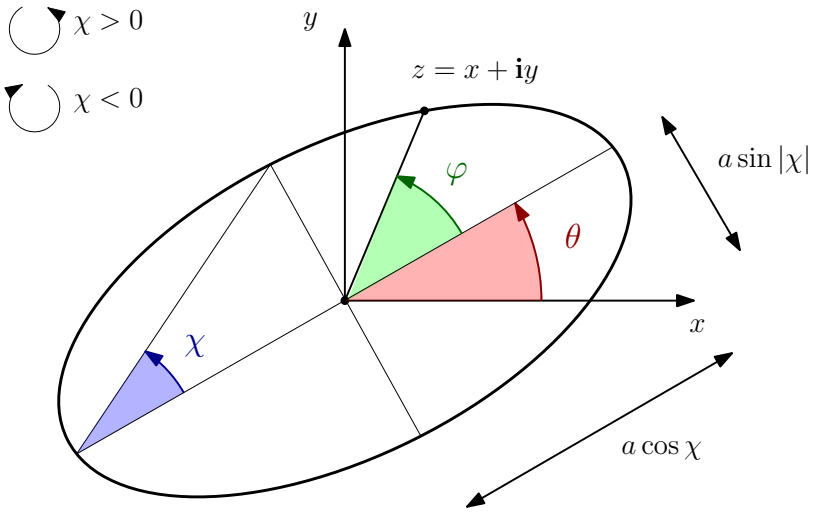

Figure 1.3: Parametrization of a monochromatic polarized signal z. The model (1.3) defines a polarized signal with a unique triplet $[a, \theta, \chi]$ characterizing the trajectory of z in the complex plane and a time-evolving phase $\varphi(t)$ which gives the time varying position of z on the ellipse.

In optics, polarized light is commonly characterized using the Stokes parameters, a set of 4 observables [1]. Those are intensities measurements corresponding to time-averaged values of cross-correlations between the two stochastic signals $x(t)$ and $y(t)$ [1]. Stokes parameters can be defined in the context of deterministic monochromatic bivariate signals analysis [3]. For $z(t)$ a monochromatic polarized signal and a, θ, χ identified in (1.3), the associated Stokes parameters at frequency ω_0 are[4]

$$\begin{aligned} S_0 &= a^2, \\ S_1 &= a^2 \cos 2\chi \cos 2\theta, \\ S_2 &= a^2 \cos 2\chi \sin 2\theta, \\ S_3 &= a^2 \sin 2\chi. \end{aligned} \tag{1.6}$$

4: See Appendix A.2 for a proper introduction of the spectral Stokes parameters.

For $i = 1, 2, 3$ we denote s_i the normalized Stokes parameter $s_i = S_i/S_0$.
The polarization state of $z(t)$ is characterized by the *polarization axis* $\boldsymbol{\mu}_z = (s_1, s_2, s_3) \in \mathbb{R}^3$.

The Stokes parameters do not incorporate the phase nor the frequency information ; they are purely geometric. Since the physical notion of polarization came from oscillatory signals, it is linked to the notion of cycles when scanning the ellipse[5]. This is why the notion of frequency and Fourier transform is particularly important for polarized signals. Key

5: Here we focused on monochromatic signals but one can anticipate that if z is built as a combination of monochromatic polarized signals with different frequencies $\omega_0, \omega_1, \ldots$ then it exhibits a different polarization at each one of these frequencies. This means that z scans different ellipses but each with a different speed.

analysis tools we use in order to analyse these kind of signals (such that the quaternion Fourier transform) are presented in Appendix A.2.

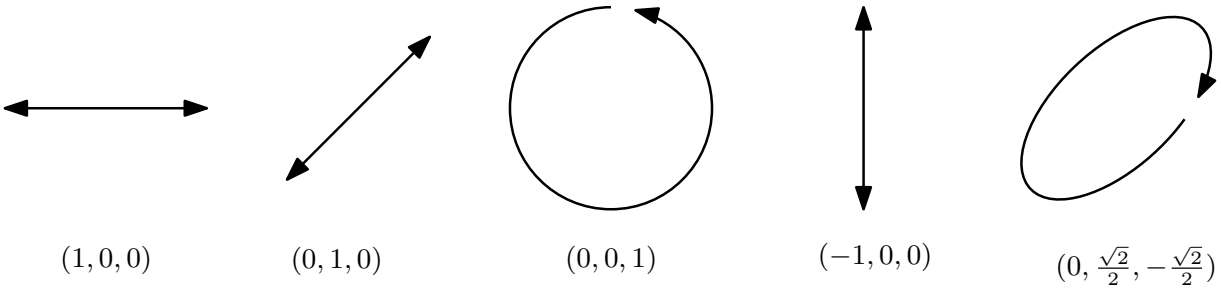

Figure 1.4: Trajectory/polarization ellipse associated to the polarization state $\boldsymbol{\mu}_z = (s_1, s_2, s_3)$. It is a geometric description of the trajectory of z in the complex plane.

As an illustration Figure 1.4 provides examples of polarization axes which derive directly from (1.6) and (1.3). By construction we have[6] $S_0 = \sqrt{{S_1}^2 + {S_2}^2 + {S_3}^2}$. Also, $s_3 = 0$ ($\chi = 0$) if z is linearly polarized and $s_3 = \pm 1$ ($\chi = \pm\pi/4$) for counterclockwise circular and clockwise circular states repectively[7]. The third normalized Stokes parameter s_3 measures the amount of circularity of z i.e. the more s_3 is near ± 1 (the more χ is near $\pi/4$), the more the trajectory is circular. Values of s_1, s_2 balance depending on the orientation of the great axis of the ellipse. s_1 is attached to the x and y axes and s_2 to diagonal axes.

6: Since the signal is deterministic, the degree of polarization $\Phi_z = \sqrt{{S_1}^2 + {S_2}^2 + {S_3}^2}/S_0$ is equal to one.

7: Here we took the convention $\omega_0 > 0$. If $\omega_0 < 0$ then $\chi = \pi/4$ and $\chi = -\pi/4$ correspond to clockwise and counterclockwise circular states respectively.

1.1.2 AM-FM-PM signals

What happens if we relax the constraints on the parameters involved in Definition 1.1.1 ? If we allow a, θ and χ to vary with time[8], clearly the ellipse scanned by z will evolve with time. We would also relax assumptions on φ to consider other phase evolutions e.g. linear, power laws etc.. This generalization is the subject of this section.

8: As we will see in Definition 1.1.2, they should be slowly varying with respect to φ.

AM-FM signals Real-valued non-stationary signals are signals $x(t)$ with time varying spectral properties. They appear in many applications such as audio processing [4, 5]. Indeed speech or music are highly non stationary time series with a spectral content subject to frequent changes over time. Amplitude and frequency modulated signals (AM-FM) is a class of non-stationary signals of particular interest in signal processing, appearing as generalization of pure harmonic

[4]: McAulay et al. (1986), *Speech analysis/Synthesis based on a sinusoidal representation*
[5]: Flandrin (2018), *Explorations in Time-Frequency Analysis*

oscillations [5]. Such signals are modelled as

$$x(t) = a(t)\cos\varphi(t). \tag{1.7}$$

$a(t) > 0$ has slow variations with respect to $\varphi(t)$ and characterizes the slowly evolving envelope of the signal i.e. low frequency part. $\cos\varphi(t)$ characterizes the oscillating behaviour and local spectral content i.e high frequency part.

Equation (1.7) describes a signal in terms of time varying instantaneous parameters namely the *instantaneous amplitude* $a(t)$ and the *instantaneous phase* $\varphi(t)$ [5, 6]. They are local properties encapsulating the time evolving oscillatory behaviour of x.

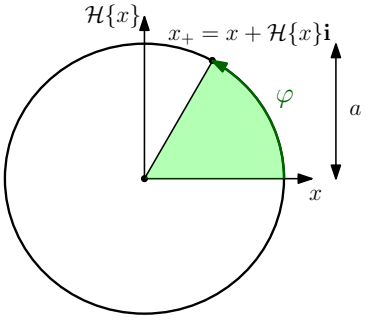

Figure 1.5: Instantaneous parameters of the AM-FM signal (1.7) in the complex plane. The circle represents the instantaneous trajectory of x_+ in the complex plane which is an augmented version of x with its quadrature part.

For a given x there is an infinite number of solutions to (1.7), showing that the pair $[a(t),\ \varphi(t)]$ is not well defined [6]. In order to define this pair without ambiguity, a classical approach consists in considering that $x(t)$ is the real part of a complex-valued signal $x_+(t) = a(t)e^{i\varphi(t)}$. This is a complex augmented version involving a $\frac{\pi}{2}$ phase shifted version of $x(t)$: $a(t)\sin\varphi(t)$. As $a(t)$ is supposed to be low frequency compared to $\varphi(t)$, the instantaneous trajectory of $x_+(t)$ in the complex plane is nearly circular and thus the instantaneous parameters $a(t)$ and $\varphi(t)$ are directly interpretable geometrically as presented in Figure 1.5.

A proper definition of the canonical pair $[a(t),\ \varphi(t)]$ involves the introduction of the Hilbert transform $\mathscr{H}_{\boldsymbol{i}}$ defined as the filtering operator with the frequency response $-\boldsymbol{i}\,\mathrm{sign}(\omega)$. A key property is that the Hilbert transform preserves the instantaneous amplitude while creating a quadrature counterpart of the cosinusoidal part through the Bedrosian theorem[9]. When the following two conditions are satisfied[10]: the amplitude varies slowlier than the phase, i.e. $|\dot\varphi(t)| \gg |\dot a(t)|\,/|a(t)|$, and the *instantaneous frequency*[11] $\dot\varphi(t)$ is itself slowly varying, i.e. $1 \gg |\ddot\varphi(t)|\,/\left|\dot\varphi^2(t)\right|$, then the Hilbert transform of $a(t)\cos\varphi(t)$ preserves the amplitude and transforms the cosine in a sine, i.e. $\mathscr{H}_{\boldsymbol{i}}\left\{a(t)\cos\varphi(t)\right\} = a(t)\sin\varphi(t)$ [6]. It naturally leads to the definition of the *analytic signal* $x_+(t) = x(t) + \mathscr{H}_{\boldsymbol{i}}\left\{x\right\}(t)\boldsymbol{i}$ of the form

$$x_+(t) = a(t)e^{\boldsymbol{i}\varphi(t)}. \tag{1.8}$$

The pair $[a(t),\ \varphi(t)]$ obtained with (1.8) is the so-called canonical pair [6]. Under the above assumptions, the instantaneous amplitude and phase of an AM-FM signal $x(t)$ can thus be

9: The Bedrosian theorem requires $a(t)$ and $\cos\varphi(t)$ to be low and high frequency respectively, with disjoint spectral supports.

10: These conditions are only heuristic, we skip technical conditions notably on the structure of $\varphi(t)$ [6].

11: From now on, we denote by a dot the temporal derivative and a double dot the second temporal derivative.

[6]: Picinbono (1997), *On Instantaneous Amplitude and Phase of Signals*

recovered by taking the modulus and phase of its associated analytic signal $x_+(t)$.

AM-FM-PM signals Non-stationary oscillating signal and the various concepts introduced above for univariate signals can be generalized to the bivariate case. This extension rests on the notion of quaternionic spectral analysis based on an analogous augmentation [3]. The approach we use leads to the introduction of meaningful quantities describing instantaneous properties of non-stationary bivariate signals and allows to generalize standard signal processing techniques to the bivariate case.

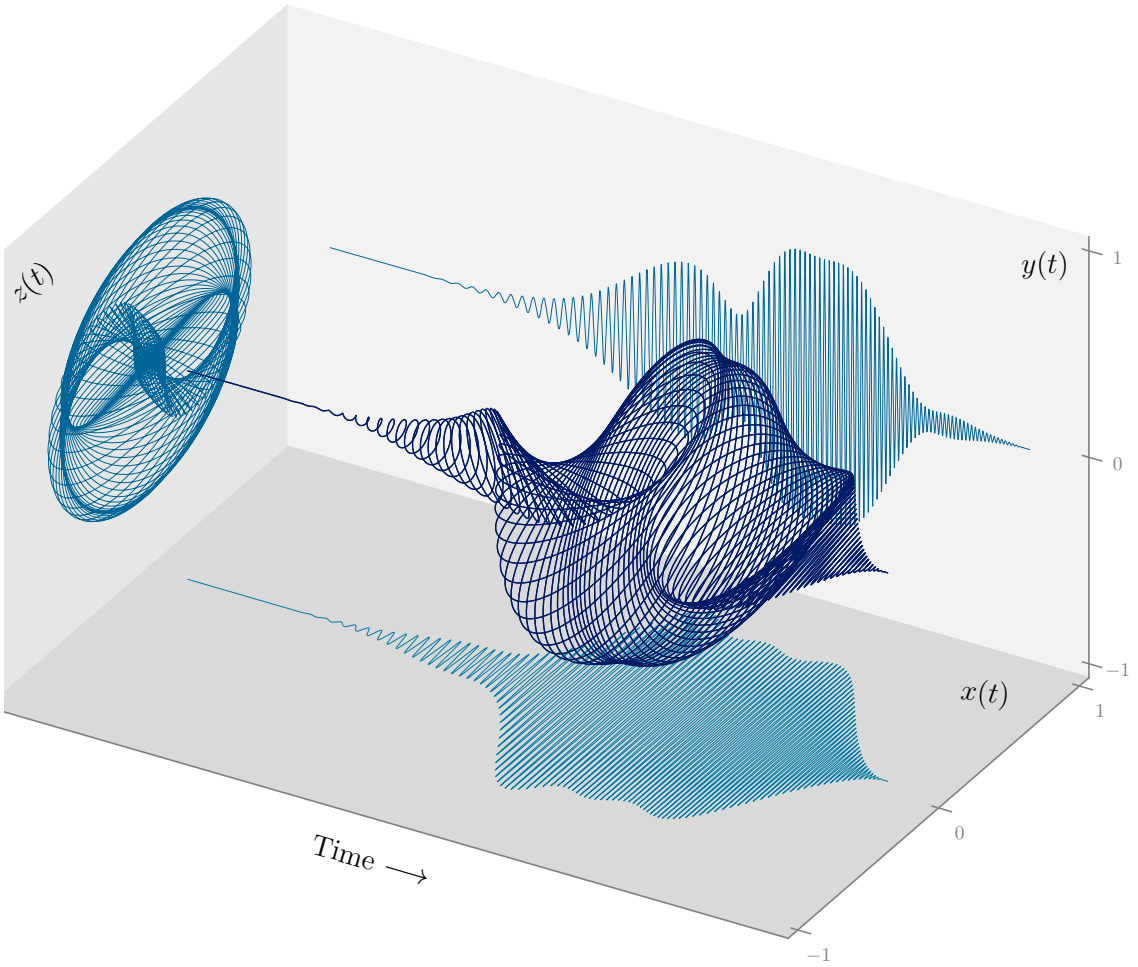

Figure 1.6: AM-FM-PM signal generated with the quadruplet (1.11) presented in Figure 1.7. It is an oscillatory signal evolving on a time-varying ellipse determined by $[a(t),\ \theta(t),\ \chi(t)]$. The scanning frequency of the ellipse $\dot{\varphi}(t)$ gives the rate at which the ellipse is scanned.

For a bivariate signal with real-valued components $x(t)$ and $y(t)$, we make use of the complex representation $z(t) = x(t) + \boldsymbol{i}y(t)$. The model (1.9) is a relaxed version of the previous model of monochromatic polarized signal (1.3).

Definition 1.1.2 *An amplitude, frequency and polarization modulated signal (AM-FM-PM) is given as the complex-valued signal of the form*

$$z(t) = a(t)e^{i\theta(t)}\left(\cos\chi(t)\cos\varphi(t) + \boldsymbol{i}\sin\chi(t)\sin\varphi(t)\right), \tag{1.9}$$

assuming

$$|\dot{\varphi}(t)| \gg \left|\dot{\theta}(t)\right|, \left|\dot{\chi}(t)\right|, \left|\frac{\dot{a}(t)}{a(t)}\right| \quad \text{and} \quad \left|\frac{\ddot{\varphi}(t)}{\dot{\varphi}^2(t)}\right| \ll 1. \tag{1.10}$$

In (1.9) and (1.10) we have added to the previous instantaneous amplitude $a(t) \geq 0$ and instantaneous phase $\varphi(t)$, the *instantaneous orientation* $\theta(t)$ and *instantaneous ellipticity* $\chi(t)$. $\dot{\varphi}(t)$ is here called the instantaneous scanning frequency of the ellipse[12]. As shown in Figure 1.6, such AM-FM-PM signal $z(t)$ describes a time evolving elliptical trajectory in the complex plane. Figure 1.7 presents the corresponding parameters used for its synthesis. They are defined as

$$\begin{aligned} a(t) &= 4\sin^2(\pi t)\, t^3, \\ \theta(t) &= 2\pi t + \sin(3\pi t), \\ \chi(t) &= \frac{\pi}{8}\sin(5\pi t + \pi) + \frac{\pi}{8}, \\ \varphi(t) &= \frac{\omega_1 - \omega_0}{2}t^2 + \omega_0 t + \varphi_0 \end{aligned} \tag{1.11}$$

with ω_0, ω_1 the starting and final elliptic frequencies and φ_0 a given initial phase. Compared to (1.7), this model allows for a much larger variability in terms of geometry of the signal trajectory.

12: In this definition the derivative of the instantaneous phase used for the synthesis of the signal is called the instantaneous ellipse scanning frequency. This is a departure from the work of Flamant et al. [7]. We will show latter that the concept of instantaneous frequency is a little bit tricky for polarized bivariate signals. The instantaneous frequency of z is defined later and is different from $\dot{\varphi}(t)$.

[7]: Flamant et al. (2019), *Time–frequency analysis of bivariate signals*

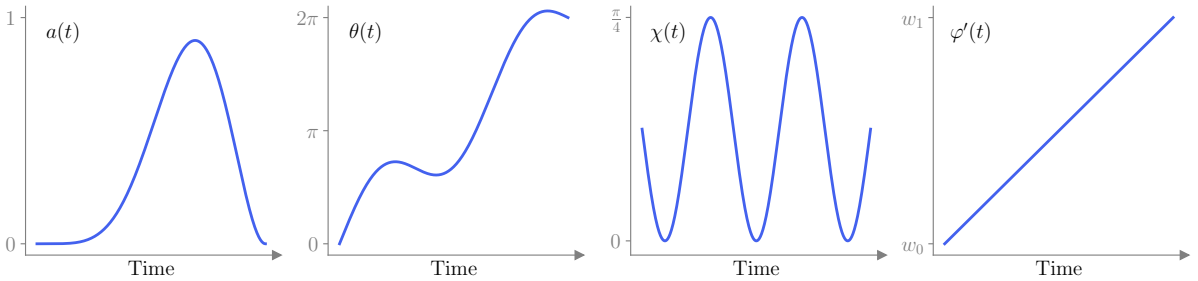

Figure 1.7: Quadruplet of instantaneous parameters used to synthetize the AM-FM-PM signal of Figure 1.6. The quadruplet is defined as (1.11).

This model implicitely describe the signal as a continuous sequence of ellipses whose shape and orientation vary with time. The instantaneous phase $\varphi(t)$ gives the position of the

signal on the ellipse with respect to its great axis. $a(t)$, $\theta(t)$ and $\chi(t)$ are geometrical parameters characterizing the ellipse drawn by the signal in the complex plane, which evolves over time. $\theta(t)$ and $\chi(t)$ are called *instantaneous polarization parameters*. The instantaneous amplitude $a(t)$ defines the size of the ellipse. The instantaneous orientation $\theta(t)$ corresponds to the angle of the great axis with respect to the real axis. The instantaneous ellipticity $\chi(t)$ determines the ratio between the minor and the major axis of the ellipse. The sign of $\chi(t)$ determines the direction in which the ellipse is scanned, counter-clockwise for $\chi(t) > 0$ and clockwise for $\chi(t) < 0$. In particular, $\chi(t) = \pi/4$ and $\chi(t) = -\pi/4$ corresponds to a counter-clockwise and clockwise circular instantaneous polarization respectively[13] whereas $\chi(t) = 0$ corresponds to a linear instantaneous polarization.

13: As before, $\dot{\varphi}(t) > 0$ by convention.

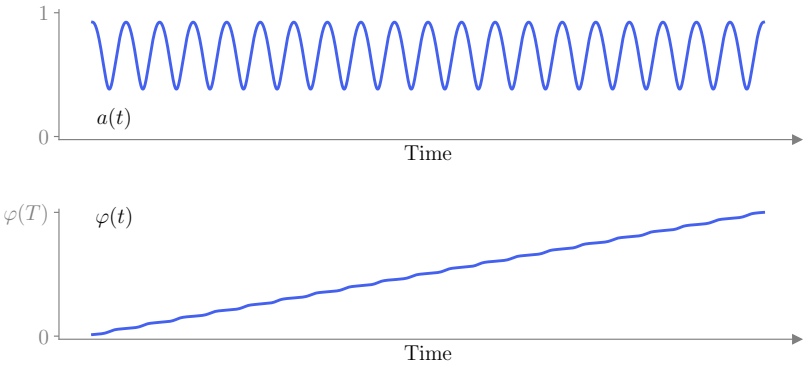

Figure 1.8: Modulus $a(t)$ and argument $\varphi(t)$ of a complex-valued monochromatic signal $z(t)$ defined with (1.5). Although the synthesis polarization parameters are constant, the modulus and phase time-series of $z(t)$ are not interpretable.

Introduction of the model (1.9) by Flamant [3] and Lilly [8] allows to go behond the classical model $a(t)e^{i\varphi(t)}$ used for the analytic signal (1.8). This new model allows to overcome the limitation of (1.8) in the description of non-circular bivariate signals. As a simple example, Figure 1.8 presents the case of a monochromatic elliptical signal $z(t)$ defined as (1.9) with constant parameters a, θ, χ and a linear phase $\varphi(t) = 2\pi\omega_0 t + \varphi_0$. χ is fixed to a value $\neq \pi/4$ such that the polarization is strictly elliptical (non-circular). We decompose $z(t)$ into its modulus $a(t) = |z(t)|$ and its argument $\varphi(t) = -\boldsymbol{i} \ln z(t)$. Because of the underlying assumption of circular polarization in (1.8), both $a(t)$ and $\varphi(t)$ exhibit high frequency oscillations and offer a complicated description of the signal intrinsic geometry with inflating circles and oscillatory phase). Indeed the amplitude and phase parametrization seems not adapted since it does not rely on any notion of polarization. Instead, (1.9) offers a simpler representation of bivariate signals with interpretable parameters in terms of instantaneous trajectory.

[8]: Lilly et al. (2006), *Wavelet ridge diagnosis of time-varying elliptical signals with application to an oceanic eddy*

1.1.3 Issues and limitations of the AM-FM-PM model

Unfortunately, the representation (1.9) given by the four degrees of freedom introduced above is degenerate in certain limiting cases. This is intimately related to the degeneracy of the mapping from the data to the representation parameters. This problem is well known in the case of real-valued AM-FM signals [9] in particular for signals with vanishing amplitude. As the phase triplet $[\theta(t), \chi(t), \varphi(t)]$ corresponds to Euler angle parametrization of 3D rotations [3], the nature of the indeterminacy is in the Euler angle singularity. The mapping between 3D rotations and Euler angles is degenerated. This chapter reviews and investigates alternatives representations in order to find another representation not affected by the same limitation. We address the following questions:

[9]: Cohen et al. (1999), *On an ambiguity in the definition of the amplitude and phase of a signal*

1. Is there a general representation of AM-FM-PM signals with interpretable parameters in terms of instantaneous trajectory which is not limited to some particular polarization cases ?
2. How to estimate the degrees of freedom of AM-FM-PM signals from the data ? More precisely, we want to seek robust and numerically stable methods to do so.

In this context, quaternions offer an appealing solution, better suited than complex numbers used so far. They have 4 dimensions, equal to the number of degrees of freedom of AM-FM-PM signals. The quaternionic formalism used in this chapter was recently introduced by Flamant et al. [7]. We focus here on the practical estimation steps and their impact on the model degeneracy . We investigate specificities of bivariate signal processing when trying to estimate the instantaneous parameters of the AM-FM-PM model (1.9).

1.2 Instantaneous parameters of AM-FM-PM signals

In the first place, Section 1.1 introduced the concept of amplitude, polarization and frequency modulated signals as a particular case of non-stationary bivariate signals that holds a geometric information. We saw that the instantaneous parameters of real-valued AM-FM signals are obtained unequivocally thanks to the introduction of the associated analytic signal. Section 1.2.2 presents the quaternionic formalism

introduced by Flamant et al. [3, 7] for the analysis of AM-FM-PM signals[14]. Section 1.2.3 defines relevant quantities for the analysis of such signals, namely the instantaneous Stokes parameters. The three polarization parameters $a(t)$, $\theta(t)$ and $\chi(t)$ derive from these quantities. Contrarily to the univariate case, Section 1.2.4 shows that the polarized model (1.9) leads to intrinsic indeterminacies. Section 1.3 enumerates possible alternative representations in order to circumvent those limitations, and discusses their pros and cons.

14: Appendix A.1 gives basic elements on quaternion algebra. In particular, q is said to be "pure" if $a = 0$. The quaternion conjugate of q is defined as $\overline{q} = a - \boldsymbol{i}b - \boldsymbol{j}c - \boldsymbol{k}d$. The modulus is defined as $|q|^2 = a^2 + b^2 + c^2 + d^2$ and q is said to be a unit quaternion if $|q| = 1$.
We define $\mathbb{C}_{\boldsymbol{i}} = \{a + \boldsymbol{i}b, b \in \mathbb{R}\} \subset \mathbb{H}$ as the space generated by the couple $\{1, \boldsymbol{i}\}$. In the same way we note $\mathbb{C}_{\boldsymbol{j}}$ and $\mathbb{C}_{\boldsymbol{k}}$ the spaces generated by the couples $\{1, \boldsymbol{j}\}$ and $\{1, \boldsymbol{k}\}$ respectively. $\mathbb{C}_{\boldsymbol{i}}$, $\mathbb{C}_{\boldsymbol{j}}$ and $\mathbb{C}_{\boldsymbol{k}}$ are isomorphic to $\mathbb{C}$. In these subsets, the multiplication is commutative.

1.2.1 Basics of quaternions and quaternionic harmonic analysis

The set of quaternions $\mathbb{H}$ is an extension of complex numbers in dimension 4. It forms an associative algebra over the real numbers but the multiplication is not commutative which complicates manipulations. A specificity of quaternions is the existence of 3 differents roots of -1: $\boldsymbol{i}$, $\boldsymbol{j}$ and $\boldsymbol{k}$. These roots are different axes of $\mathbb{H}$ with which we define the cartesian form of any quaternion $q \in \mathbb{H}$ as

$$q = a + \boldsymbol{i}b + \boldsymbol{j}c + \boldsymbol{k}d,$$

where $a \in \mathbb{R}$ is its real part and $b, c, d \in \mathbb{R}$ are coefficients of its imaginary (or vector) part. Multiplications can be computed through associativity by respecting the following cyclic rules for the multiplication of imaginary components:

$$\begin{aligned}
\boldsymbol{i}^2 = \boldsymbol{j}^2 = \boldsymbol{k}^2 &= -1, \\
\boldsymbol{i}\boldsymbol{j} = -\boldsymbol{j}\boldsymbol{i} &= \boldsymbol{k}, \\
\boldsymbol{k}\boldsymbol{i} = -\boldsymbol{k}\boldsymbol{i} &= \boldsymbol{j}, \\
\boldsymbol{j}\boldsymbol{k} = -\boldsymbol{k}\boldsymbol{j} &= \boldsymbol{i}.
\end{aligned}$$

For each axis $\boldsymbol{\mu} = \boldsymbol{i}, \boldsymbol{j}, \boldsymbol{k}$ the quaternion exponential is defined as[15] $e^{\boldsymbol{\mu}\phi} = \cos\phi + \boldsymbol{\mu}\sin\phi$ for a given $\phi \in \mathbb{R}$. Other basic notions on quaternion algebra needed for this chapter are detailed in Appendix A.1.

15: This definition is valid for any pure quaternion $\boldsymbol{\mu}$ i.e. for all $\boldsymbol{\mu} \in \mathbb{H}$ such that $\boldsymbol{\mu}^2 = -1$.

In particular, the canonical involution of axis $\boldsymbol{j}$ is such that $\overline{q}^{\boldsymbol{j}} = -\boldsymbol{j}q\boldsymbol{j} = a - \boldsymbol{i}b + \boldsymbol{j}c - \boldsymbol{k}d$ (respectively for $\boldsymbol{j}$ and $\boldsymbol{k}$). We denote $q^{*\boldsymbol{j}} = \overline{\overline{q}}^{\boldsymbol{j}} = a + \boldsymbol{i}b - \boldsymbol{j}c + \boldsymbol{k}d$ the combination of an involution and a conjugation of axis $\boldsymbol{j}$ (respectively for $\boldsymbol{i}$ and $\boldsymbol{k}$).

The various concepts of spectral analysis, filtering etc. can be extended using quaternions. A brief introduction of quaternion spectral analysis is done in Appendix A.2. For a square integrable bivariate signal $z(t) = x(t) + \boldsymbol{i}y(t)$ the quaternion Fourier transform is defined as

$$Z(\omega) = \frac{1}{\sqrt{2\pi}} \int z(t) e^{-j\omega t} \mathrm{d}t. \tag{1.12}$$

Manipulations of this object is tricky because of the non-commutativity of quaternion multiplication. For example, moving the quaternion exponential to the left side of the analyzed signal would define an other object.

(1.12) differs from the complex transform by the choice of its axis: $\boldsymbol{j}$. The choice of the orthogonal axis $\boldsymbol{j}$ compared to $\boldsymbol{i}$ permits to analyse each signal component separately (compute Fourier transforms along each axis at once). The polarization analysis can be derived using the quaternion algebra [3] as elaborated in the next section.

1.2.2 Quaternion embedding of bivarate signals

Let us consider an arbitrary bivariate signal $z(t) = x(t) + \boldsymbol{i}y(t)$ which is not necessarily a polarized monochromatic signal nor an AM-FM-PM signal. As $z(t) \in \mathbb{C}_i$ the $\boldsymbol{i}$-symmetry property holds[16] i.e. $Z(-\omega) = \overline{Z(\omega)}^{\boldsymbol{i}}$. This means that the frequency content of the quaternionic Fourier transform is symmetrically distributed around the zero frequency. Thus, negative frequencies carry redundant information compared to positive frequencies and removing them from the Fourier transform of z can be done without loss of information. The classic complex Fourier transform applied to a complex-valued signal does not obey the same properties. Similarly with the complex Fourier transform in the univariate case, this is the first clue motivating the use of the quaternionic formalism for complex-valued signals analysis. This observation leads to the definition of the quaternion embedding [7]

$$z_{\mathbb{H}}(t) = z(t) + \mathscr{H}_j \{z\}(t)\boldsymbol{j}. \tag{1.13}$$

The practical computation procedure is depicted in Appendix A.3. It is the equivalent of the analytic signal associated to a real-valued signal but in the bivariate case with $\mathscr{H}_j$ the quaternionic Hilbert transform defined as a linear filter operator of frequency response $-\boldsymbol{j}\,\mathrm{sign}(\omega)$. The spectral

16: This is the equivalent of the Hermitian symmetry of the complex Fourier transform. See Appendix A.2 for further explanation of this statement. The proof is straightforward: remarks that for $z(t) = x(t) + \boldsymbol{i}y(t)$ we get $Z(\omega) = X(\omega) + \boldsymbol{i}Y(\omega)$ by linearity of the QFT (quaternion Fourier transform), as $x(t)$ and $y(t)$ are real-valued, $X(\omega)$ and $Y(\omega)$ are $\mathbb{C}_j$-valued. Being the Fourier transform of real-valued signals, $X(\omega)$ and $Y(\omega)$ verify the Hermitian symmetry, such that $Z(-\omega) = \overline{X(\omega)} + \boldsymbol{i}\overline{Y(\omega)}$. The proof ends by noting that $\overline{Z(\omega)}^{\boldsymbol{i}} = \overline{X(\omega)} + \boldsymbol{i}\overline{Y(\omega)}$.

content of the quaternionic embedding is by construction $Z_{\mathbb{H}}(\omega) = 0 \,\forall\, \omega \in \mathbb{R}^*_-$ and $Z_{\mathbb{H}}(\omega) = 2Z(\omega) \,\forall\, \omega \in \mathbb{R}_+$. It follows immediately that $\hat{z}_{\mathbb{H}}(t) \in \mathbb{H} \,\forall\, t \in \mathbb{R}$ and that $\hat{z}_{\mathbb{H}}$ is encapsulating the energetic and polarization content of z such that

$$\int |z(t)|^2 \,\mathrm{d}t = \int |z_{\mathbb{H}}(t)|^2 \,\mathrm{d}t, \tag{1.14}$$

$$\int z(t) z(t)^{*j} \mathrm{d}t = \int z_{\mathbb{H}}(t) z_{\mathbb{H}}(t)^{*j} \mathrm{d}t. \tag{1.15}$$

(1.14) implies that the energy z is conserved as well as (1.15) shows that its geometric content is conserved in $z_{\mathbb{H}}$.

A classical interpretation of the action of the complex Hilbert transform involves AM-FM signals. For a given AM-FM signal $x(t) = a(t)\cos\varphi(t)$ one remarks that $\mathscr{H}_i\{x\}(t) = a(t)\sin\varphi(t)$, showing that the Hilbert transform creates a quadrature counterpart of the analyzed signal [6]. The same applies to the quaternionic Hilbert transform. For z a bivariate AM-FM-PM signal defined as (1.9), assuming (1.10) and further technical assumptions on the phase structure[17], the Bedrosian theorem implies[18]

$$\mathscr{H}_j\{z\}(t) = a(t) e^{\boldsymbol{i}\theta(t)} \left(\cos\chi(t)\sin\varphi(t) - \boldsymbol{i}\sin\chi(t)\cos\varphi(t)\right). \tag{1.16}$$

Showing that the Hilbert transform does not affect the polarization parameters $[a(t),\ \theta(t),\ \chi(t)]$ and creates a $\pi/2$ phase shifted version of z.

As in the real-valued case, we use the Hilbert transform as an instrument to access instantaneous parameters of AM-FM-PM signals. In particular Section 1.2.3 uses it to introduce the notion of instantaneous polarization state.

17: A particular structure of the phase is needed in order for the Hilbert transform to convert a cosine into a sine and conversely. The argument is strictly the same than for the complex Hilbert transform [6].

18: As in the real-valued case, (1.10) only defines heuristic conditions. Bedrosian theorem requires a disjoint spectral support for $\sin\varphi(t)$ and the different combinations of $a(t)$, $\theta(t)$, $\chi(t)$ involved in each real and imaginary part of (1.9) and $\sin\varphi(t)$ should be high frequency compared to other terms.

1.2.3 Instantaneous Stokes parameters

In optics, Stokes parameters are quadratic expectation quantities measuring the degree of polarization and the shape of the polarization ellipse [1]. Since we focus on deterministic non-stationary signals, we are interested in their time-varying version defining the instantaneous polarization state of non-stationary bivariate signals. We define the *instantaneous Stokes parameters* associated to a non-stationary bivariate signal z as

$$|z_{\mathbb{H}}(t)|^2 = S_0(t) \quad \text{and} \quad z_{\mathbb{H}}(t) z_{\mathbb{H}}(t)^{*j} = S_1(t) + \boldsymbol{i}S_2(t) - \boldsymbol{k}S_3(t) \tag{1.17}$$

where $z_{\mathbb{H}}(t)$ is the quaternionic embedding defined Section 1.2.2. Under technical conditions mentioned in Section 1.2.2, one can find the following expressions for the instantaneous Stokes parameters of an AM-FM-PM signal:

$$\begin{aligned} S_0(t) &= a(t)^2, \\ S_1(t) &= a(t)^2 \cos 2\chi(t) \cos 2\theta(t), \\ S_2(t) &= a(t)^2 \cos 2\chi(t) \sin 2\theta(t), \\ S_3(t) &= a(t)^2 \sin 2\chi(t). \end{aligned} \tag{1.18}$$

While they do not depend on the instantaneous phase $\varphi(t)$, they solely characterize the geometry of the instantaneous trajectory of z in the complex plane. That is, the instantaneous polarization ellipse. When focusing on the geometrical content, we rather consider their normalized version

$$s_1(t) = S_1(t)/S_0(t) \quad s_2(t) = S_2(t)/S_0(t) \quad s_3(t) = S_3(t)/S_0(t) \tag{1.19}$$

for $S_0(t) \neq 0$. They define the instantaneous polarization state of z which is characterized by the *instantaneous polarization axis*: $\boldsymbol{\mu}_z(t) = (s_1(t), s_2(t), s_3(t)) \in \mathbb{R}^3$. Figure 1.4 illustrates the interpretation of the instantaneous polarization axis which derives directly from (1.18). The interpretation is similar to monochromatic polarized signals except that the polarization axis is now a function of time. Polarization is now a "local" property.

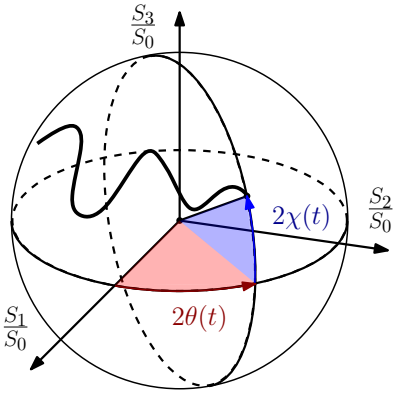

Figure 1.9: Polarization curve representing instantaneous polarization evolution of z along time on the Poincare sphere.

The normalized instantaneous Stokes parameters (1.19) are the Cartesian coordinates of the instantaneous polarization state of z on the Poincaré sphere. As opposed to the classical introduction of Stokes parameters, we restrict our analysis to deterministic signals which have the property to be fully polarized i.e. $\sqrt{S_1(t)^2 + S_3(t)^2 + S_3(t)^2} = S_0(t)$ (it is also valid in the spectral domain). This means that the instantaneous polarization state of z lies on the surface of the Poincaré sphere. $\boldsymbol{\mu}_z(t)$ draws a curve on the Poincaré sphere corresponding to the time evolution of the polarization state of an AM-FM-PM signal. Figure 1.9 illustrates the idea of seeing polarization modulation on the Poincaré sphere. For a circularly polarized signal it follows directly from (1.18) that Stokes parameters are such that $s_1(t) = s_2(t) = 0$ and $s_3(t) = \pm 1$, depending on $\chi = \pm\frac{\pi}{4}$. So the North and South hemispheres of the Poincaré sphere correspond to counterclockwise and clockwise polarization.

Stokes parameters do not offer a complete parameterization of the signal since they lack a phase term. It is not obvious how to

retrieve the phase term. We summarize some of our attempts in the next section. As we elaborate in Section 1.4, the addition of an instantaneous frequency information companion to the Stokes parameters may be a good solution to complete the parametrization.

1.2.4 The Euler angle polar form

The Euler angle polar form of the quaternion embedding is the cornerstone of the quaternionic formalism introduced by Flamant [3]. It motivates the use of a quaternionic formalism to build an extension of real-valued signals analysis and legitimate the previous work of Lilly and Olhede [8][10]. The Euler angle polar form is a particular decomposition of quaternions by four parameters associated to each axis of $\mathbb{H}$. In the case of elliptic AM-FM-PM signal, the four parameters of the Euler angle polar form

[10]: Lilly et al. (2010), *Bivariate Instantaneous Frequency and Bandwidth*

$$z_{\mathbb{H}}(t) = a(t)e^{\boldsymbol{i}\theta(t)}e^{-\boldsymbol{k}\chi(t)}e^{\boldsymbol{j}\varphi(t)} \tag{1.20}$$

are identified to those of (1.9). This is true under technical conditions on the phase [6, 7]. The quadruplet $[a(t), \theta(t), \chi(t), \varphi(t)]$ is then called the canonical quadruplet. So simply by reading its phase argument, the quaternionic Hilbert transform gives access to the instantaneous parameters of an AM-FM-PM bivariate signal.

The canonical quadruplet can be computed in several ways [7, 8]. One makes use of the instantaneous Stokes parameters defined in Section 1.2.3. Obviously the estimated instantaneous amplitude[19] $\hat{a}(t)$ is the modulus of $z_{\mathbb{H}}(t)$, which also corresponds to the square root of $S_0(t)$. From the three other instantaneous Stokes parameters we get $\hat{\theta}(t) = \arctan\left[\hat{s}_2(t)/\hat{s}_1(t)\right]/2$ and $\hat{\chi}(t) = \arcsin \hat{s}_3(t)/2$. Those are directly unwrapped in order to avoid discontinuity of the instantaneous orientation and phase resulting from the possible crossing between the major axis of the istantaneous ellipse and the y axis of the complex plane. The instantaneous phase $\hat{\varphi}(t)$ is then deduced by the logarithm of $\hat{a}^{-1}(t)e^{\boldsymbol{k}\hat{\chi}(t)}e^{-\boldsymbol{i}\hat{\theta}(t)}z_{\mathbb{H}}(t)$.

19: By convention, estimated quantities are denoted with a hat.

Representation degeneracies and the gimbal lock

Unlike the standard AM-FM model, that has no ambiguity between instantaneous parameters when conditions (1.10) are

satisfied [6], the AM-FM-PM model possesses two fundamental limitations. First, one can anticipate that the model (1.9) becomes degenerate when the instantaneous trajectory becomes circular i.e. when $\chi(t) = \pm\frac{\pi}{4}$. We have especially

$$e^{\boldsymbol{i}\theta(t)}e^{\mp\boldsymbol{k}\frac{\pi}{4}}e^{\boldsymbol{j}\varphi(t)} = e^{\boldsymbol{i}(\theta(t)+\Delta(t))}e^{\mp\boldsymbol{k}\frac{\pi}{4}}e^{\boldsymbol{j}(\varphi(t)\mp\Delta(t))} \tag{1.21}$$

for any $\Delta(t) \in \mathbb{R}$. The signal looses one degree of freedom and the decomposition (1.20) becomes redundant in the circular case. This degeneracy is known as the Euler angle singularity. Equation (1.21) emphasises the indeterminacy between the instantaneous orientation and instantaneous phase. In the counterclockwise circular case i.e. $\chi = \frac{\pi}{4}$ taking $\Delta(t) = -\theta(t)$ in (1.21) shows that the only valuable quantities are $a(t)$ and $\varphi(t) + \theta(t)$. In the clockwise circular case i.e. $\chi = -\frac{\pi}{4}$, they become $a(t)$ and $\varphi(t) - \theta(t)$. The parametrization $[a(t),\ \theta(t),\ \chi(t),\ \varphi(t)]$ is not adapted in the circular case because there is no great axis, and thus no instantaneous orientation $\theta(t)$. By analogy with classical mechanics we refer to this singularity as the *gimbal lock*, even though these are two different concepts [11]. In these cases it makes no sense to consider a great axis given by $\theta(t)$ because the instantaneous trajectory is circular, then the adapted polar decomposition is $z_{\mathbb{H}}(t) = a(t)e^{\mp\boldsymbol{k}\frac{\pi}{4}}e^{\boldsymbol{j}\varphi(t)}$.

[11]: Hemingway et al. (2018), *Perspectives on Euler angle singularities, gimbal lock, and the orthogonality of applied forces and applied moments*

In the case of continuous time signals, the gimbal lock is tractable if we accept to change the signal model on time intervals where the signal is circularly polarized. For a bivariate signal with a time varying polarization axis passing from an elliptical to a circular polarization state at time t_0, a quadruplet $\left[\hat{a}(t),\ \hat{\theta}(t),\ \hat{\chi}(t),\ \hat{\varphi}(t)\right]$ can always be computed but is no longer unique. One should first compute the instantaneous polarization parameters and the instantaneous phase on the time intervals $I \subset \mathbb{R}$ such that $\chi(t) \neq \pm\frac{\pi}{4} \quad \forall t \in I$, and otherwise use a circular parametrization $z(t) = a(t)e^{\boldsymbol{i}\varphi(t)}$. A quadruplet can be estimated along the whole time axis by imposing regularity conditions or an underlying model for $\theta(t)$ and $\varphi(t)$.

Discrete time and numerically induced degeneracies

The situation is further complicated in the case of discrete time signals. Due to numerical errors, the above degeneracy extends beyond the case where $\chi = \pm\pi/4$ exactly. The discretization of the quaternionic Hilbert transform causes approximation errors which could arise from a phenomenon

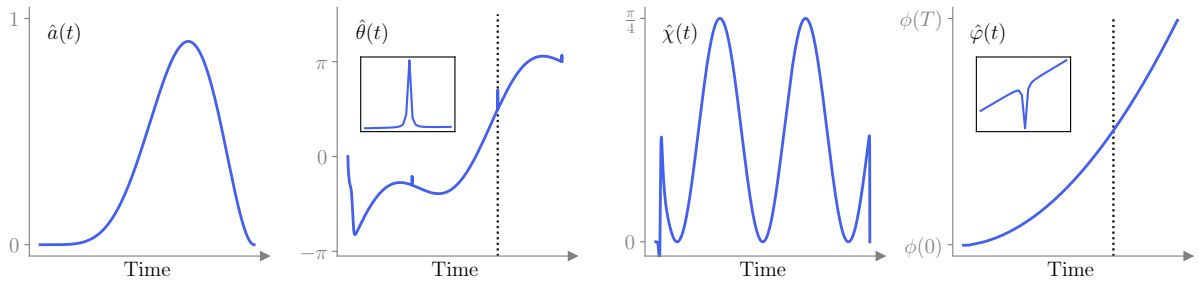

(a)

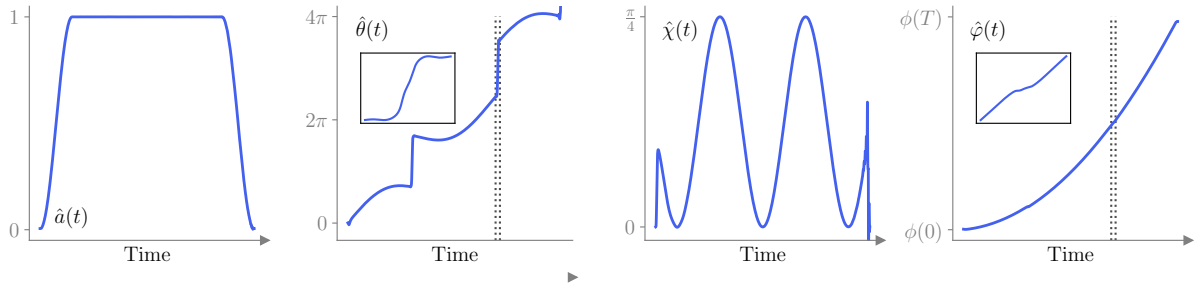

(b)

Figure 1.10: (a) is the estimated quadruplet $\left[\hat{a}(t), \hat{\theta}(t), \hat{\chi}(t), \hat{\varphi}(t), \right]$ from the signal presented in Figure 1.6. We expect to reconstruct the quadruplet presented in (1.11) and Figure 1.7, but we are limited by the instrumental gimbal lock (aside errors du to the vanishing amplitude) which causes estimations errors in time intervals when $z(t)$ is quasi-circular. Zooms on a problematic time region are presented for $\hat{\theta}(t)$ and $\hat{\chi}(t)$. The corresponding time region is reported by dashed lines. In this case the instantaneous frequency is near the edge of the frequency domain which amplifies the phenomenon. This time the instrumental gimbal lock induces typical spurious jumps (continuously) in $\hat{\theta}(t)$. The instantaneous amplitude is replaced by a Tukey window for **(b)**, which result in a more comon pattern of the estimated parameters.

we call *instrumental gimbal lock*, mixing $\hat{\theta}(t)$ and $\hat{\varphi}(t)$ estimates in the near circular case $\left|\chi(t) \mp \frac{\pi}{4}\right| \leqslant \epsilon$. It results that for discrete signals the intervals are much more difficult to handle. The proposed procedure creating surrogates instantaneous parameters is operable under hard constrained parameter models[20].

It is well known that the computation of the discrete-time complex Hilbert transform induces approximation errors impacting instantaneous frequency approximation. These limitations transfer to the discrete-time quaternionic Hilbert transform in a way that for some polarization patterns they lead to confusions between the instantaneous phase[21] $\varphi[n]$ and the instantaneous orientation $\theta[n]$. That is, for nearly circular polarizations, estimates $\hat{\theta}[n]$ exhibit fast variations, taking some part of the information normally supported by $\varphi[n]$. In other words, assuming $\theta[n]$, $\chi[n]$, $\varphi[n]$ are the "true" parameters of some bivariate signal and $\hat{\theta}[n]$, $\hat{\varphi}[n]$ their respective estimates[22], then for $\left|\chi[n] \mp \frac{\pi}{4}\right| \ll \epsilon$ (typically for $\epsilon \ll 1$) the numerical errors induce a non-zero term $\Delta[n]$ such that $\hat{\theta}[n] = \theta[n] + \Delta[n]$ and $\hat{\varphi}[n] = \varphi[n] - \Delta[n]$. Ap-

20: The instrumental gimbal lock has the effect of creating regions where $\chi(t) \neq \mp\frac{\pi}{4}$ but $\theta(t)$ and $\varphi(t)$ can't be disentangled from $z_{\mathbb{H}}$. Then, a choice has to be made to select intervals on which we are consciously "blind".

21: In this paragraph, the triplet $[\theta[n], \chi[n], \varphi[n]]$ is the discrete version of the previous $[\theta(t), \chi(t), \varphi(t)]$ and respectively for $z[n]$.

22: $\hat{\theta}[n]$ and $\hat{\varphi}[n]$ are estimated from $z_{\mathbb{H}}[n]$ with the procedure outlined in Section 1.2

proximation errors of the discrete-time quaternionic Hilbert transform induce what we call an instrumental (or analogic) gimbal lock. Figure 1.10 illustrates the instrumental gimbal lock on the synthetised signal presented in Section 1.1.2. It is different from the gimbal lock identified in Section 1.2.4 in the sense that there is no intrinsic indetermination since $\chi[n] \neq \pm\frac{\pi}{4}$ for all n. The phenomenon is even more visible for scanning frequency of the ellipse $\dot{\varphi}(t)$ near the edges of the frequency spectrum[23]. Such approximation errors when computing the discrete-time Hilbert transform does not influence the validity of the synthesis scheme i.e. we always have that[24] $\mathrm{Proj}_{\mathbb{C}_i}\{z_{\mathbb{H}}[n]\} = z[n]$, but the only damper is that $\hat{\theta}[n]$ and $\hat{\varphi}[n]$ are not the expected ones. It is amplified by Gibbs phenomenon and is more problematic for $|\dot{\varphi}(t)| \ll f_s/4$ and $|\dot{\varphi}(t)| \gg f_s/4$ where f_s is the sampling frequency.

23: This may result from coupled effects with separability conditions of the Bedrosian theorem.

24: For any subset $U \subset \mathbb{H}$, Proj_U is the projection operator on U. Thus for $q = a + \boldsymbol{i}b + \boldsymbol{j}c + \boldsymbol{k}d$, $\mathrm{Proj}_{\mathbb{C}_i}\{q\} = a + \boldsymbol{i}b$.

In practice, one must impose an underlying model for $\theta[n]$ and $\varphi[n]$ in order to elude the indetermination. We suggest a simple optimization procedure with possible constraints:

$$\theta_{\hat{\alpha}},\ \varphi_{\hat{\beta}} \text{ are such that } \hat{\alpha},\ \hat{\beta} = \arg\min_{\alpha,\beta} \sum_{n=0}^{N-1} \left| z_{\mathbb{H}}[n] - \hat{a}[n] e^{\boldsymbol{i}\theta_\alpha[n]} e^{\boldsymbol{i}\hat{\chi}[n]} e^{\boldsymbol{i}\varphi_\beta[n]} \right|^2 \tag{1.22}$$

where the instantaneous orientation θ_α and instantaneous phase φ_β follow a regular trend (e.g. a spline) associated with the parameters α and β respectively. The suggested procedure was tested on toy examples. The results show that it is not always possible to retrieve the synthesis parameters, and to do so, strong constraints should be applied to the parameter models.

1.3 Alternative representations of AM-FM-PM signals

Section 1.2 has shown that a well suited parametrization of a polarized signal z appears in the Euler angle polar decomposition of its quaternion embedding $z_{\mathbb{H}}$. Unfortunately this parametrization incorporates an intrinsic indeterminacy for certain polarization states, namely circular states, and thus is not adapted in a general analysis framework. In this section we debate other possible representations of the quaternionic embedding $z_{\mathbb{H}}$ in order to find a better suited one from

an analysis point of view. We are seeking an interpretable representation not limited to certain polarization cases.

1.3.1 Vector and complex representations

The quaternion Fourier transform defined in (1.12) consists in applying a complex Fourier transform to the real and imaginary parts of a complex-valued signal, the introduction of quaternion being motivated by the manipulation they allow. Moreover, the canonical quadruplet $[a(t),\ \theta(t),\ \chi(t),\ \varphi(t)]$ was first defined beside a quaternionic formalism [8]. These remarks appeal for different representations of polarized bivariate signals in the complex formalism. In the classical complex-valued Fourier framework, the definition of the quadruplet involves a first projection step of $z(t)$ into two orthogonal polarization states[25].

Vector representation One classic representation consists in considering $x(t)$ and $y(t)$ independently[26] [2, 10]. This approach is motivated by a vectorial representation of bivariate signals: $[x(t),\ y(t)]^T$, from which each component is analysed separately[27]. Considering $x(t)$ and $y(t)$ as two real-valued AM-FM signals, one can compute their associated analytic signals and decompose them as $x_+(t) = a_x(t)e^{\varphi_x(t)}$ and $y_+(t) = a_y(t)e^{\varphi_y(t)}$. This defines a parametrization of the bivariate signal $z(t) = x(t) + \boldsymbol{i}y(t)$ by the quadruplet $\big[a_x(t),\ a_y(t),\ \varphi_x(t),\ \varphi_y(t)\big]$. Expressions of this quadruplet according to parameters of the Euler angle polar form (1.20) are the following:

$$
\begin{aligned}
a_x(t) &= \frac{a(t)}{\sqrt{2}}\sqrt{1+s_1(t)}, \quad \varphi_x(t) = \varphi(t) + \arctan\left(\tan\theta(t)\tan\chi(t)\right),\\
a_y(t) &= \frac{a(t)}{\sqrt{2}}\sqrt{1-s_1(t)}, \quad \varphi_y(t) = \varphi(t) - \arctan\frac{\tan\chi(t)}{\tan\theta(t)}.
\end{aligned}
\tag{1.23}
$$

for $a_x^2(t) \neq a_y^2(t)$ (non-circular case). As this parametrization is associated to an orthogonal basis of $\mathbb{R}^2$, there are two linear polarization states for which the first amplitude $a_y(t)$ or the second $a_y(t)$ vanishes[28].

Complex representation Another approach consists in considering $z(t)$ and its complex conjugate[29] $\overline{z}(t)$ [2, 10]. This way we get two circular components $z_+(t) = a_+(t)e^{\varphi_+(t)}$

25: Two polarization axes $\boldsymbol{\mu}_1,\ \boldsymbol{\mu}_2 \in \mathbb{R}^3$ represent orthogonal states if they are anti-aligned: $\langle \boldsymbol{\mu}_1, \boldsymbol{\mu}_2 \rangle = -1$ where $\langle .,. \rangle$ stands for the usual scalar product of $\mathbb{R}^3$.

26: It corresponds to a projection of the signal on the two orthogonal linear polarization states $\boldsymbol{\mu}_1 = (1,\ 0,\ 0)$ and $\boldsymbol{\mu}_2 = (-1,\ 0,\ 0)$.

27: Here the subscript T stands for the vector transpose.

28: $a_y(t)$ and $a_y(t)$ vanish when $\boldsymbol{\mu}_z(t) = (1,\ 0,\ 0)$ and $\boldsymbol{\mu}_z(t) = (-1,\ 0,\ 0)$ respectively.

29: It corresponds to a projection of the signal on the orthogonal polarization states $\boldsymbol{\mu}_1 = (0,\ 0,\ 1)$ and $\boldsymbol{\mu}_2 = (0,\ 0,\ -1)$.

and $z_-(t) = a_-(t)e^{\varphi_-(t)}$ which are called the counterclockwise and clockwise rotary components respectively. They are the analytic signals associated to the original bivariate signal $z(t)$ and its complex conjugate $\overline{z(t)}$. This way we build the decomposition $z(t) = (z_+(t) + \overline{z_-(t)})/2$ parametrized by $[a_+(t), a_-(t), \varphi_+(t), \varphi_-(t)]$. Each of these parameters has a non-linear dependence on the previous Euler angle parameters:

$$\begin{aligned} a_+(t) &= a(t)\sqrt{1+s_3(t)}, \quad & \varphi_+(t) &= \varphi(t) + \theta(t), \\ a_-(t) &= a(t)\sqrt{1-s_3(t)}, \quad & \varphi_-(t) &= \varphi(t) - \theta(t). \end{aligned} \tag{1.24}$$

By construction $z_+(t)$ and $z_-(t)$ vanish for clockwise and counterclockwise circular polarization states respectively[30].

30: Remark that $s_3(t) = -1$ and thus $a_+(t) = 0$ for a clockwise circular polarization state, and respectively for counterclockwise circular polarization state with $s_3(t) = 1$ which implies $a_-(t) = 0$.

Clearly the vector and complex representations lie in some particular projection of $z(t)$ on two orthogonal polarization states while the quaternionic approach does not. Aside technical assumptions these projections are not motivated since the instantaneous parameters are not attached to any polarization state. Separately none of the introduced parameters are interpretable in terms of instantaneous polarization ellipse property. Each one of these two representations introduces parameters as non linear functions of the polarization parameters $[a(t), \theta(t), \chi(t), \varphi(t)]$. However, unlike the quaternionic approach, the vectorial approach does generalize to other multivariate signals [12]. Expressions of the Euler angle polar form parameters according to these two parametrizations can be found in [3].

[12]: Lilly et al. (2012), *Analysis of Modulated Multivariate Oscillations*

Those two representations also have problematic cases. When the instantaneous polarization state of the analysed signal $\boldsymbol{\mu}_z(t)$ is equal to one of the two orthogonal polarization states $\boldsymbol{\mu}_1$ or $\boldsymbol{\mu}_2$ used by the representation, the corresponding component (e.g. z_+ or z_- for the complex representation) vanishes and its phase is indeterminate[31]. We observe the same behaviour as for the instrumental gimbal lock: when $\boldsymbol{\mu}_z(t)$ is close to $\boldsymbol{\mu}_1$ (or $\boldsymbol{\mu}_2$), then discretization of the Hilbert transform induces errors on phase estimation.

31: The point is that one parameter is indeterminate even if the energy of z is non zero.

1.3.2 Symplectic forms

Previous examples have shown that all representations are not equal in terms of interpretation and usefulness. Equation (1.13) directly provides the Cayley Dickson form of the quaternionic embedding [13]

[13]: Ell et al. (2014), *Quaternion Fourier Transforms for Signal and Image Processing*

$$z_{\mathbb{H}}(t) = z_1(t) + z_2(t)\boldsymbol{j}$$

with $z_1(t) = z_{1\mathbf{1}}(t) + \boldsymbol{i}z_{1\boldsymbol{i}}(t)$ and $z_2(t) = z_{2\mathbf{1}}(t) + \boldsymbol{i}z_{2\boldsymbol{i}}(t)$. In this decomposition each $z_{1\mathbf{1}}(t)$, $z_{1\boldsymbol{i}}(t)$, $z_{2\mathbf{1}}(t)$ and $z_{2\boldsymbol{i}}(t)$ are the parameters. From (1.13) it is clear that $z_1(t) = z(t)$ and that $z_2(t)$ is the $\frac{\pi}{2}$ phase shifted version presented in (1.16). Then the Cayley Dickson form gives the parametrization $[x(t), x_+(t), y(t), y_+(t)]$. The decomposition is trivially useless in practice, as it introduces parameters that are the analyzed signals (the two components of z) themselves and their associated analytic signals.

The Cayley Dickson form is a particular case of the symplectic form

$$z_{\mathbb{H}}(t) = (a(t) + b(t)\boldsymbol{\mu}) + (c(t) + d(t)\boldsymbol{\mu})\boldsymbol{\nu}$$

with $\boldsymbol{\mu} \perp \boldsymbol{\nu} \in \mathbb{H}$ and $\boldsymbol{\mu}^2 = \boldsymbol{\nu}^2 = -1$ that encompass all non-polar representations of quaternions. In particular, any symplectic form with $\boldsymbol{\mu}, \boldsymbol{\nu} \in \{\boldsymbol{i}, \boldsymbol{j}, \boldsymbol{k}\}$, such as the Cayley-Dickson, would get the same four parameters $[x(t), x_+(t), y(t), y_+(t)]$. This comes from the linearity of the quaternionic Hilbert transform. Other symplectic forms would have at least $x(t)$ as parameter and three polynomial functions of $\{x_+(t), y(t), y_+(t)\}$. Overall, non-polar representations seem not adapted to describe instantaneous properties of polarized signals. Since they do not rely on any notion of frequency or even angle, the possibilities of geometric interpretation are compromised.

1.3.3 The classic polar form

The Euler angle polar form (1.20) depends on a particular choice of axes. These axes are chosen in order to match angles from (1.9) with those of (1.20). One may look for other quaternion polar decompositions expecting no particular indeterminate case. The general quaternion polar form [13]

$$z_{\mathbb{H}}(t) = a(t)e^{\Omega(t)} \tag{1.25}$$

is defined with a pure quaternion argument $\Omega(t) \in \mathbb{H}$ and a modulus $a(t) \in \mathbb{R}_+$. Again $a(t)$ is referred to as the instantaneous amplitude of the signal. The argument is decomposed in a phase term $\phi(t) \in \mathbb{R}$ and a pure unit quaternion $\boldsymbol{\mu}(t) \in \text{span}\{\boldsymbol{i}, \boldsymbol{j}, \boldsymbol{k}\}$ which are the angle and the axis of the rotation represented by $z_{\mathbb{H}}(t)/a(t)$ respectively: $\Omega(t) = \phi(t)\boldsymbol{\mu}(t)$.

[13]: Ell et al. (2014), *Quaternion Fourier Transforms for Signal and Image Processing*

Unlike complex signals, the axis of the exponential $\boldsymbol{\mu}(t)$ is varying. We get[32]

$$\begin{aligned}\phi(t) = \arccos\big[&\cos\theta(t)\cos\chi(t)\cos\varphi(t)\\ &-\sin\theta(t)\sin\chi(t)\sin\varphi(t)\big],\end{aligned} \tag{1.26}$$

$$\begin{aligned}\boldsymbol{\mu}(t) = \Big[&\boldsymbol{i}\sqrt{1-s_1(t)}\cos\left(\varphi(t)-\arctan\frac{\tan\chi(t)}{\tan\theta(t)}\right)\\ &+\boldsymbol{j}\sqrt{1+s_1(t)}\sin\left(\varphi(t)+\arctan\left(\tan\theta(t)\tan\chi(t)\right)\right)\\ &+\boldsymbol{k}\sqrt{1-s_1(t)}\sin\left(\varphi(t)-\arctan\frac{\tan\chi(t)}{\tan\theta(t)}\right)\Big]\\ &\Big/\frac{a(t)}{\sqrt{2}}\Big[1-s_1(t)\\ &\quad+\left(1+s_1(t)\right)\sin^2\left[\varphi(t)+\arctan\left(\tan\theta(t)\tan\chi(t)\right)\right]\Big].\end{aligned} \tag{1.27}$$

32: As defined in Appendix A.1, for any $q \in \mathbb{H}$ such that $q \neq 0$ the logarithm is defined such that

$$\ln(q) = \ln|q| + \frac{\operatorname{Im}\{q\}}{|\operatorname{Im}\{q\}|}\arccos\frac{\operatorname{Re}\{q\}}{|q|}.$$

Equations (1.26) and (1.27) are obtained from the vector representation presented in Section 1.3.1.

Since parameters $[a(t), \Omega(t)]$ and $\left[a(t), \phi(t), \boldsymbol{\mu}(t)\right]$ are not based on Euler angle decomposition of 3D rotations, they are not subject to the same drawbacks as the Euler angle polar form (1.20). That is, there is no indeterminate case but on the other hand we have lost interpretability. Both $\boldsymbol{\mu}(t)$ and $\phi(t)$ are functions of the instantaneous phase $\varphi(t)$ and other geometric parameters. The instantaneous axis $\boldsymbol{\mu}(t)$ is rotating. One may see this by computing one of its spherical coordinates: namely $\arctan\left(\boldsymbol{\mu}_k(t)/\boldsymbol{\mu}_i(t)\right) = \varphi(t) - \arctan\frac{\tan\chi(t)}{\tan\theta(t)}$.

1.3.4 The Cayley-Dickson polar form

Historically, the polar Cayley-Dickson form was introduced before the interpretation of the Euler polar form [13]. It was an attempt to build interpretable instantaneous parameters for AM-FM-PM signals. It introduces two complex parameters $\rho(t)$, $\psi(t) \in \mathbb{C}_{\boldsymbol{i}}$ such that

$$z_{\mathbb{H}}(t) = \rho(t)e^{\psi(t)\boldsymbol{j}}. \tag{1.28}$$

$\rho(t)$ is called the *complex modulus* and $\psi(t)$ the *complex phase*. It is easy to see that this form as a particular Euler angle representation

$$z_{\mathbb{H}}(t) = |\rho(t)|\, e^{\boldsymbol{i}\arctan\frac{\rho_{\boldsymbol{i}}(t)}{\rho_1(t)}} e^{\boldsymbol{j}\psi_1(t)} e^{\boldsymbol{k}\psi_{\boldsymbol{i}}(t)} \tag{1.29}$$

with different axes for the decomposition. One would prefer to use the Euler angle polar form (1.25) since the axes are adapted to the quantities directly involved in the AM-FM-PM model (1.9).

1.4 Instantaneous frequency and first instantaneous moments of the QFT

For real-valued AM-FM signals $x(t) = a(t)\cos\varphi(t)$ the instantaneous frequency $\omega(t)$ is identified with the derivative of the phase. It gives the local oscillation frequency of the signal. Two properties support this interpretation. First, $\dot{\varphi}(t)$ is identified with the first instantaneous moment of the spectral energy density $\frac{1}{\|x_+\|^2}|X_+(\omega)|^2$ [14, 15]. Second, it determines the ridge of its time-frequency and time-scale transforms (Gabor or Wavelet transforms for example) [16].

[14]: Ville (1948), *Théorie et Applications de la Notion de Signal Analytique*
[15]: Marple (1999), *Computing the discrete-time "analytic" signal via FFT*
[16]: Delprat et al. (1992), *Asymptotic wavelet and Gabor analysis: extraction of instantaneous frequencies*

It is less direct to define an instantaneous frequency associated to bivariate AM-FM-PM signals. We have seen in Section 1.2.4 that when polarized signals become circular the instantaneous phase of the polarized model (1.9) is not well defined as it is degenerate with the orientation angle $\theta(t)$. This prevents the straightforward extension from the real-valued case.

Lilly and Olhede [12] introduced the notion of *joint instantaneous frequency* in the broader case of oscillating multivariate signals. They considered the case of multivariate signals with multiple AM-FM components that have slightly different instantaneous frequencies. In this setting it is possible to generalize the notion of instantaneous frequency as a leading common frequency from which each component has a small instantaneous departure. It turns out that this joint instantaneous frequency is identified with the first instantaneous spectral moment of the multivariate signal and also the ridge of its time-frequency or time-scale transform. Figure 1.11 presents the ridge of the quaternion windowed Fourier transform of the AM-FM-PM signal defined as (1.11).

For a given bivariate signal z, $\frac{1}{\|z_{\mathbb{H}}\|^2}|z_{\mathbb{H}}(t)|^2$ and $\frac{1}{\|z_{\mathbb{H}}\|^2}|Z_{\mathbb{H}}(\omega)|^2$ are seen as probability densities describing an amount of information at time t and frequency ω carried by z. Bivariate signals are also characterized by[33] an additional geometric content which is encapsulated in the *spectral polarization density* $\frac{1}{\|z_{\mathbb{H}}\|^2}Z_{\mathbb{H}}(\omega)Z_{\mathbb{H}}(\omega)^{*j}$ that can be seen as a density

33: The quaternion-valued spectral density introduced by Flamant [3] is defined with respect to the two Parseval invariants of the quaternion Fourier transform, see Equations (A.8) and (A.9) of Appendix A.

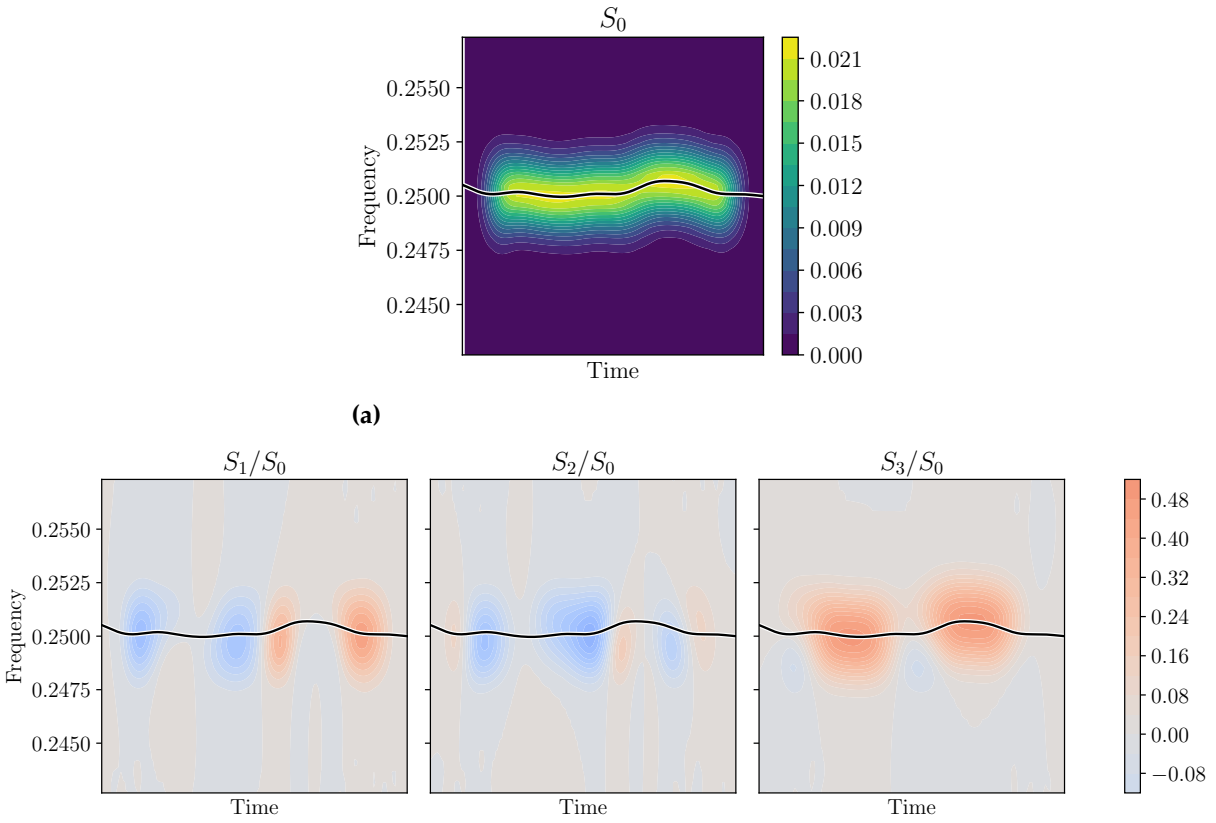

Figure 1.11: Energy spectrogram **(a)** and polarization spectrogram **(b)** of the signal presented in Figure 1.6. The frequency scale is normalized. In this example the signal is monochromatic: $\omega_0 = \omega_1 = 0.25$ and the amplitude is a Tukey window (for visualization puposes). The black line is the first instantaneous moment of the spectral energy density $\omega_z(t)$. The values of the instaneous Stokes parameters are on the ridge of the spectrogram.

34: Note that the spectral polarization density is a density on the Poincaré sphere. It is a quadratic quantity which is quaternion-valued and for which each component can take negative values.

of geometric information[34]. The general results presented in [12] apply for non stationary polarized signals but are extended here with the notion of *instantaneous polarization moment* defined as the instantaneous moment associated with the spectral polarization density. If the first order moments of these spectral densities exist, their instantaneous contributions $\omega_z(t) \in \mathbb{R}$ and $\nu_z(t) \in \text{span}\{\mathbf{1}, \boldsymbol{i}, \boldsymbol{k}\}$ are such that

$$\int \omega \left|Z_{\mathbb{H}}(\omega)\right|^2 \mathrm{d}\omega = \int \omega_z(t) \left|z_{\mathbb{H}}(t)\right|^2 \mathrm{d}t \tag{1.30}$$

and

$$\int \omega Z_{\mathbb{H}}(\omega) Z_{\mathbb{H}}(\omega)^{*j} \mathrm{d}\omega = \int \nu_z(t) \left|z_{\mathbb{H}}(t)\right|^2 \mathrm{d}t. \tag{1.31}$$

$\omega_z(t)$ is the *first instantaneous moment of the spectral energy density* and $\nu_z(t)$ the *first instantaneous moment of the polarization energy density*. As stated in Appendix A.2 $Z(\omega)Z(\omega)^{*j} = S_1(\omega) + \boldsymbol{i}S_2(\omega) - \boldsymbol{k}S_3(\omega)$ so the first instantaneous polar-

ization moment $\nu_z(t)$ embodies distributions of each normalized Stokes parameter. Thus $\nu_{z\mathbf{1}}$, $\nu_{z\boldsymbol{i}}$ and $-\nu_{z\boldsymbol{k}}$ are the instantaneous contributions to the mean normalized Stokes parameters s_1, s_2 and s_3 respectively.

From (1.30) and (1.31) one can find the following expressions of the instantaneous moments[35]:

$$\omega_z(t) = \mathrm{Proj}_{\mathbb{R}} \left\{ \frac{\dot{z}_{\mathbb{H}}(t)\boldsymbol{j}^{-1}\overline{z_{\mathbb{H}}(t)}}{|z_{\mathbb{H}}(t)|^2} \right\}, \tag{1.32}$$

$$\nu_z(t) = \mathrm{Proj}_{\mathrm{span}\{\mathbf{1},\boldsymbol{i},\boldsymbol{k}\}} \left\{ \frac{\dot{z}_{\mathbb{H}}(t)\overline{z_{\mathbb{H}}(t)}\boldsymbol{j}^{-1}}{|z_{\mathbb{H}}(t)|^2} \right\}. \tag{1.33}$$

35: See Equations (A.12) and (A.14) of Appendix A.4.

According to the AM-FM-PM model (1.9), we can derive the following expressions

$$\omega_z(t) = \dot{\varphi}(t) + \dot{\theta}(t)s_3(t) \tag{1.34}$$

and

$$\begin{aligned} \nu_{z\mathbf{1}}(t) &= \dot{\varphi}(t)s_1(t) + \dot{\chi}(t)\frac{s_2(t)}{s_3(t)}, \\ \nu_{z\boldsymbol{i}}(t) &= \dot{\varphi}(t)s_2(t) - \dot{\chi}(t)\frac{s_1(t)}{s_3(t)}, \\ -\nu_{z\boldsymbol{k}}(t) &= \dot{\varphi}(t)s_3(t) + \dot{\theta}(t) \end{aligned} \tag{1.35}$$

(and $\nu_{z\boldsymbol{j}}(t) = 0$) for each instantaneous moments (see Appendix A.4). Expressions (1.35) show that the contribution of the instantaneous polarization axis $\boldsymbol{\mu}_z(t) = (s_1(t),\, s_2(t),\, s_3(t))$ to the mean polarization depends on the instantaneous frequency $\dot{\varphi}(t)$ plus a corrective term:

$$\nu_z(t) = \dot{\varphi}(t)\boldsymbol{\mu}_z(t) + \left(\dot{\chi}(t)\frac{s_2(t)}{s_3(t)},\, -\dot{\chi}(t)\frac{s_1(t)}{s_3(t)},\, \dot{\theta}(t) \right). \tag{1.36}$$

It trivially means that the more the instantaneous ellipse is scanned, the more important its contribution to the polarization moment is. More interestingly (1.34) shows that the elliptic instantaneous frequency $\dot{\varphi}(t)$ does not characterize the local frequency content of the signal just like in the univariate case, because the first instantaneous moment $\omega_z(t)$ (almost surely[36]) involves contribution from the derivative of the instantaneous orientation $\theta(t)$.

36: The distinction should be made for constant $\theta(t)$ and linear polarization states.

Although in the first introduction of the quaternion formalism $\dot{\varphi}(t)$ was called the instantaneous frequency [7], we claim that it should not be named so[37]. It would seem that this

37: After the preliminar works [8, 10], Lilly and Olhede defined $\omega_z(t)$ as the joint instantaneous frequency [12]. A term that they proved to be better adapted.

misconception is due to the analogy with the univariate case where the first instantaneous moment of the spectral energy density corresponds to the instantaneous phase derivative $\dot{\varphi}(t)$ [14]. In order to avoid possible confusions, in the context of AM-FM-PM signal analysis we kept the term instantaneous scanning frequency of the ellipse attached to $\dot{\varphi}(t)$ and the term instantaneous frequency attached to $\omega_z(t)$.

One may remark that the dot product between the instantaneous polarization axis and the vector of first instantaneous polarization moment gives the instantaneous frequency i.e.

$$\nu_{z\mathbf{1}} s_1(t) + \nu_{z\boldsymbol{i}} s_2(t) - \nu_{z\boldsymbol{k}} s_3(t) = \omega_z(t). \tag{1.37}$$

Also, the instantaneous frequency, the third instantaneous Stokes parameter and the associated instantaneous moment characterize the instantaneous scanning frequency of the ellipse, at least in the non circular case, with

$$\dot{\varphi}(t) = \frac{\omega_z(t) + \nu_{z\boldsymbol{k}}(t) s_3(t)}{1 - s_3^2(t)}. \tag{1.38}$$

It follows that the signal is fully characterized by its instantaneous polarization and its first instantaneous spectral energy moment[38]: $[S_1(t),\ S_2(t),\ S_3(t),\ \omega_z(t)]$. The last term allows to retrieve the missing phase term as discussed in Section 1.2.3. Those parameters are non-degenerate observables which can always be estimated in a noisy setting [3, 12].

38: Note that $\varphi(t)$ can be retrieved from $\omega_z(t)$ and $[S_1(t),\ S_2(t),\ S_3(t)]$ using (1.34).

1.5 Conclusion

We defined the notion of bivariate signals modulated in both amplitude, frequency and polarization as a generalization real-valued AM-FM signals synthetised with four parameters: $[a(t),\ \theta(t),\ \chi(t),\ \varphi(t)]$. AM-FM-PM signals are a broad class of oscillating bivariate signal with time evolving elliptical trajectories. They are part of a broader range of multivariate signals for which several components share a leading common frequency [12].

It turns out that in some cases an AM-FM-PM signal loses one degree of freedom, i.e., when the polarization state becomes circular. This is a concern from an analysis point of view: for a given signal z, in a noiseless situation, one would not be able to recover the synthesis parameters. The decoupling between $\dot{\varphi}(t)$ and the ridge of time-frequency transforms

(which is the instantaneous moment $\omega_z(t)$) concludes the discussion of AM-FM-PM signal representations: $\dot{\varphi}(t)$ could not be considered as the instantaneous frequency of z and can't be retrieved from a time-frequency analysis. Even if the model (1.9) is well adapted in a synthesis point of view, it is not true in an analysis framework. A recovery is possible when imposing constraints on $\theta(t)$ and $\varphi(t)$ in order to complete "blind" spots (e.g. regularity constraints).

From the perspective of finding a parametrization not subject to the same limitations, we reviewed possible quaternion representations. There are several desirable representation properties: the representation should be interpretable and should not have indeterminate cases (at least when the signal energy is not vanishing). We showed that parametrization of AM-FM-PM signals different from the Euler angle polar representation are either not interpretable (classic polar form, Cayley-Dickson polar form, symplectic forms) or subject to particular limitations (vector and complex representations).

This work was motivated by the application presented in Chapter 3, we were seeking a representation of gravitational wave signals (which are AM-FM-PM signals) adapted to the generation algorithm we propose. Considering a large class of gravitational wave signals, we concatenate each waveform attribute in a matrix that we expect to be low rank. Unfortunately the instrumental gimbal lock is prohibiting for the Euler angle polar representation as a generic solution.

The vector and complex representations also suffer from limitations: (i) there are cases where one of the two phases is indeterminate (even if the signal energy is non-zero), (ii) it is not interpretable for a generic AM-FM-PM signal and (iii) the parameters are not regular and oscillate. The usage of such parametrizations associated to two orthogonal polarization states is limited to certain classes of signals and applications. In general, and specifically for the cases of interest in this thesis, it will not be possible to get low rank decomposition of signal parameters for signals passing through one of these two polarization states. The classic polar form, the Cayley-Dickson polar form and the symplectic forms have both highly oscillating parameters which makes them impractical for low rank decomposition.

Finally, we found observables characterizing AM-FM-PM signals which are defined without ambiguity: $\left[S_1(t), S_2(t), S_3(t), \omega_z(t)\right]$, or equivalently $\left[S_0(t), s_1(t), s_2(t), s_3(t), \omega_z(t)\right]$.

These parameters are interpretables and does not suffer from indeterminacies for non-vanishing signals. They are observables of a time-frequency representation of the signal. As such, they can even be estimated in a noisy setting. For a noiseless signal, the procedure is presented in Section 1.2.4. In a noisy setting, the estimation procedure is classic: one estimates the ridge of a signal's time-frequency transform and directly read the Stokes parameters on it while $\omega_z(t)$ corresponds to the ridge skeleton [3, 12].

Nevertheless, and contrarily to other reviewed representations, the latter include a quantity that rest on a discrete differentiation for practical implementations: the instantaneous frequency $\omega_z(t)$. One need to integrate $\omega_z(t)$ in order to retrieve the bivariate signal z from its attributes. This renders the estimations errors of $\omega_z(t)$ to scale cumulatively in the regression error of z and prevented us to consider $\left[S_1(t), S_2(t), S_3(t), \omega_z(t)\right]$ as a possible waveform representation for the application presented in Chapter 3. As will be detailed in Chapter 3, the polarization of the waveform modes depends on the choice of the source frame in which the gravitational waveform is expanded. A geometrical tricks is used in order to circumvent Euler angle indeterminacy, which consist in (i) choosing the source frame to favour elliptic polarization and (ii) restraining the polarization modulations by considering a reduced region of the source parameters (and thus avoid circular polarization states).

2 Introduction to gravitational-wave astronomy

In the theory of general relativity, the space-time concept mathematically represents space and time as two inseparable and mutually influencing quantities. According to this theory, gravitational interactions result from deformations in the geometry of space-time, generated by masses.

Mathematically, space-time is defined as a 4-dimensional semi-Riemannian manifold[1], which is a locally Euclidean topological space whose geometry is defined by a metric tensor. The Einstein field equations define the way the metric relates and evolves with energy or matter contents. Gravitational waves are wave-like solutions of the Einstein field equations, i.e. variations of the curvature of space-time propagating in space. Gravitational waves are generated by accelerated masses. The generation of substantial amount of gravitational radiation requires very large masses at relativistic velocities, properties that are only encountered in extreme astrophysical systems of compact objects such as neutron stars or black holes.

1: Semi-Riemannian manifolds are a generalisation of Riemannian manifolds with a smoothly varying symmetric metric tensor which is non-degenerate [17]. More precisely, it is a manifold with a pseudo-Riemannian metric i.e. a topological space which is localy similar to a Euclidean space for which the requirement of positive-definiteness is relaxed and on which we can derive differential calculus.

[17]: Petersen (2016), *Riemannian Geometry*

Both neutron stars and (stellar-mass) black holes are formed from the gravitational collapse of the core of a massive star. Neutron stars have a $\sim$ 10-km core made of very dense matter essentially composed of neutrons. Black holes are even more compact celestial objects, so compact that they bend space-time to the point of preventing any matter or radiation from escaping from the inner region bounded by their horizon.

In our Galaxy it is common to observe pairs of stars, generally referred to as binary star systems. Those can evolve into pairs of black holes or/and neutron stars following the collapse of each object, thus forming compact binaries.

When the two objects are sufficiently close to each other, they radiate a significant fraction of their binding energy in the form of gravitational waves and gradually move even closer, eventually leading the final merger. During the inspiral, the two components orbit around each other reaching relative velocities close to the speed of light. Finally, the two objects merge into a black hole whose mass is roughly the sum of the two initial bodies' masses. The orbital motion during the inspiral and merger induces a quasi-periodic gravitational wave with a characteristic phase and amplitude time evolution.

The 14th of September 2015 marked the birth of gravitational-wave astronomy [18]. The first ever recorded gravitational wave was detected by both LIGO[2] instruments. It is the product of the coalescence of two black holes of around 36 and 29 solar masses. The two objects orbiting at relativistic speed merged and produced a single 62 solar masses black hole. The event, located at more than one billion light-years from Earth, released 3 solar masses as gravitational radiation.

[18]: Abbott et al. (2016), *Observation of Gravitational Waves from a Binary Black Hole Merger*

2: LIGO stands for Laser Interferometer Gravitational-Wave Observatory.

Since then, about 90 signals have been detected by the LIGO-Virgo collaboration [19] that are associated with the coalescence of compact binaries composed of either black holes and/or neutron stars. The majority of the sources detected so far are binary black holes [20], a type of source on which we focus in this manuscript.

[19]: Abbott et al. (2021), *GWTC-3: Compact Binary Coalescences Observed by LIGO and Virgo During the Second Part of the Third Observing Run*

[20]: Abbott et al. (2020), *GWTC-2: Compact binary coalescences observed by LIGO and Virgo during the first half of the 3rd observing run*

Some of the details of the source dynamics get imprinted into the emitted gravitational wave. As a result, properties of the source can be learned from the analysis of the gravitational-wave signal. Accurate gravitational waveform models are deduced from the resolution of the source dynamics which is a difficult relativistic problem [21]. The evaluation of the astrophysical waveform models can be computationally demanding and thus resulting in an inflation of the computational budget.

[21]: Buonanno et al. (1999), *Effective one-body approach to general relativistic two-body dynamics*

Based on the generic model introduced in the previous chapter, this chapter is dedicated to the development of models that approximate theoretical gravitational waveforms but are much faster to compute.

2.1 Gravitational-wave theory

Published in 1905, the theory of general relativity succesfully resolves the contradictions between Newtonian mechanics and Maxwell theory of electromagnetism [22]. It reformulates laws of classical mechanics and makes them compatible with the invariance of the speed of light c in a vacuum showed by Michelson and Morley [23].

[22]: Einstein (1923), *Die Grundlage der allgemeinen Relativitätstheorie*

[23]: Michelson et al. (1887), *LVIII. On the relative motion of the earth and the luminiferous Æther*

In GR (general relativity) spacetime is a 4-dimensional semi-Riemannian manifold. Its geometry is described by the Einstein tensor $G_{\mu\nu}$ defined as

$$G_{\mu\nu} = R_{\mu\nu} - \frac{1}{2} g_{\mu\nu} R,$$

with $R_{\mu\nu}$ the Ricci curvature tensor, R the scalar curvature and $g_{\mu\nu}$ the metric tensor which allows to compute distances between spacetime points. μ and ν denote the time and spatial coordinates.

The Einstein field equations associate the geometry of spacetime with the mass-energy evolving in it as

$$G_{\mu\nu} = \frac{8\pi G}{c^4} T_{\mu\nu},$$

where G the Newtonian's gravitational constant and $T_{\mu\nu}$ the stress-energy tensor linked to the mass-energy distribution.

The metric tensor $g_{\mu\nu}$ includes information about spacetime curvature as it characterizes the spacetime interval[3]:

$$\mathrm{d}s^2 = g_{\mu\nu}\mathrm{d}x^\mu \mathrm{d}x^\nu.$$

3: In this section we use the Einstein summation convention that consists in summing over indexes that are repeated in upper and lower position.

In the flat Minkowski spacetime with coordinates (ct, x, y, z), the Minkowski metric reads

$$\eta_{\mu\nu} = \begin{pmatrix} -1 & 0 & 0 & 0 \\ 0 & 1 & 0 & 0 \\ 0 & 0 & 1 & 0 \\ 0 & 0 & 0 & 1 \end{pmatrix}$$

and the invariant spacetime interval is[4] $\mathrm{d}s^2 = -c^2\mathrm{d}t^2 + \mathrm{d}x^2 + \mathrm{d}y^2 + \mathrm{d}z^2$.

4: For two events E_1 and E_2 with respective coordinates $s_1 = (ct_1, x_1, y_1, z_1)$ and $s_2 = (ct_2, x_2, y_2, z_2)$, their distance is computed as a spacetime interval:

$$\Delta s^2 = -c^2(t_2 - t_1)^2 + (x_2 - x_1)^2 + (y_2 - y_1)^2 + (z_2 - z_1)^2.$$

Einstein's equations are non-linear, but considering a weak pertubation $h_{\mu\nu}$ of the metric $\eta_{\mu\nu}$

$$g_{\mu\nu} = \eta_{\mu\nu} + h_{\mu\nu} \quad \text{with} \quad \left|h_{\mu\nu}\right| \ll 1,$$

they can be linearized as

$$\Box\overline{h}_{\mu\nu} - \eta_{\mu\nu}\partial^\rho\partial^\sigma\overline{h}_{\rho\sigma} - \partial^\rho\partial_\nu\overline{h}_{\mu\rho} - \partial^\rho\partial_\mu\overline{h}_{\nu\rho} = -\frac{16\pi G}{c^4}T_{\mu\nu},$$

where $\overline{h}_{\mu\nu} = h_{\mu\nu} - (1/2)\eta_{\mu\nu}\eta^{\mu\nu}\overline{h}_{\mu\nu}$ is the traceless tensor and $\Box = g^{\mu\nu}\partial_\mu\partial_\nu$ is the d'Alembert operator. In an appropriate coordinate system, namely the transverse-traceless-temporal gauge, the above equation simplifies in a wave equation[5]

$$\left(\nabla^2 - \frac{1}{c^2}\frac{\partial^2}{\partial t^2}\right) h_{\mu\nu} = 0,$$

5: Here we denoted $\nabla^2 = \sum_{i=1}^{3} \frac{\partial^2}{\partial {x_i}^2}$.

whose solutions are called "gravitational waves".

Gravitational waves are transverse waves propagating at

speed of light. Because the metric is the Minkowski metric plus a small spatial perturbation, we can explicitely write this metric for the three-dimensional Euclidean space. Considering a coordinate system such that its z axis is aligned with the propagation direction, we define a vector[6] $\vec{k}$ which points from the source to the observer, such that

$$k = \begin{pmatrix} 0 \\ 0 \\ 1 \end{pmatrix}.$$

6: In the following, we denote vector objects with an arrow $\rightarrow$ and tensors with a double arrow $\leftrightarrow$. The arrows are removed when expressing the objects in a given coordinate frame.

The matrix associated to the metric tensor perturbation writes

$$h = \begin{pmatrix} h_+ & h_\times & 0 \\ h_\times & -h_+ & 0 \\ 0 & 0 & 0 \end{pmatrix}$$

with h_+ and $h_\times$ two independent degrees of freedom, functions of $t - \vec{k}.\vec{r}/c$, and corresponding to two polarizations: *plus* and *cross* polarizations respectively.

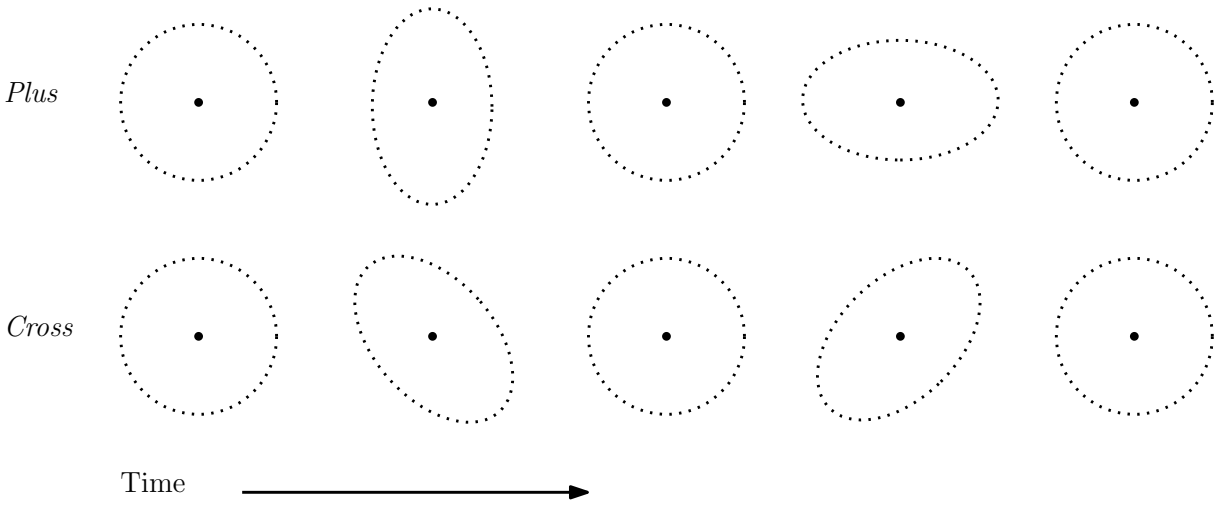

Figure 2.1: Effect of the plus and cross polarizations on a ring of test particles in the transverse (x, y) plane with respect to the propagation direction z. There is no displacement along the direction of propagation. The cross polarization is a $\pi/4$-rotated version of the plus polarization.

It can also be presented as

$$h = h_+ e_+ + h_\times e_\times$$

where

$$e_+ = \begin{pmatrix} 1 & 0 & 0 \\ 0 & -1 & 0 \\ 0 & 0 & 0 \end{pmatrix} \quad \text{and} \quad e_\times = \begin{pmatrix} 0 & 1 & 0 \\ 1 & 0 & 0 \\ 0 & 0 & 0 \end{pmatrix}$$

are polarization matrices associated to the polarization basis tensors $\overleftrightarrow{e_+}$ and $\overleftrightarrow{e_\times}$. They are defined such as $\overleftrightarrow{e_+} = \vec{p}\otimes\vec{p} - \vec{q}\otimes\vec{q}$

and $\overleftrightarrow{e_+} = \vec{p} \otimes \vec{q} - \vec{q} \otimes \vec{p}$ for $\vec{p}$ and $\vec{q}$ the unit vectors defining the wave frame. For an inertial frame $(\vec{e}_1^I, \vec{e}_2^I, \vec{e}_3^I)$ attached to the source, the wave frame $(\vec{p}, \vec{q}, \vec{k})$ is such that

$$\vec{q} = \frac{\vec{e}_3^I \times \vec{k}}{|\vec{e}_3^I \times \vec{k}|} \quad \text{and} \quad \vec{p} = \vec{k} \times \vec{q}.$$

In this setting, the two polarizations lead to the physical effect depicted in Figure 2.1. This figure shows the effect of a gravitational wave on a ring of test particles in "free fall" (subject to gravity only). Plus polarization alternates between vertical stretching/horizontal squeezing and conversely. Cross polarization is identical to plus polarization with a rotation by $\pi/4$. Gravitational waves are thus intrinsically bivariate signals, with two signals h_+ and $h_\times$ associated to each polarization.

2.2 Gravitational-wave observatories

2.2.1 The Virgo detector

Virgo[7] is a major European experiment designed to detect gravitational waves [24]. It is located in Cascina, near Pisa in Italy, and was put into operation in the early 2000s, see Figure 2.3.

7: Virgo is named after the Virgo Cluster of about 1 500 galaxies in the Virgo constellation.

[24]: Accadia et al. (2012), *Virgo: a laser interferometer to detect gravitational waves*

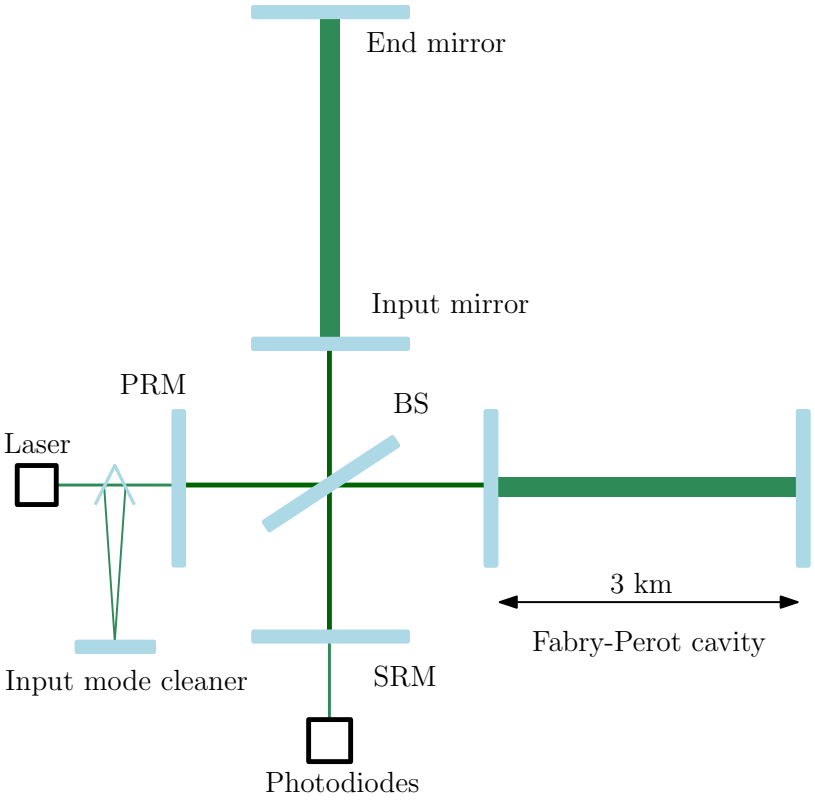

Figure 2.2: Simplified Advanced Virgo optical layout. A light beam is emitted and splitted into the two arms of the detector by the beam splitted (BS). The interference pattern of the recombinated light beam at the photodetector depends on the relative length of one arm compared to the other. When a gravitational wave passes through the detector, this relative length is modified and the interference pattern is impacted. The mode cleaner removes spurious modes while the signal and power recycling cavities, with the power and signal recycling mirrors (PRM and SRM), enhance the sensitivity of the detector.

Figure 2.3: Aerial view of Virgo the European gravitational wave detector. Virgo detector has two arms of 3 kilometers.

The detector has two perpendicular 3 km arms in which a laser beam is splitted. It measures a signal corresponding to the relative difference ΔL of its arm length L thanks to the interference scheme of the recombined light, see Figure 2.2. The two recombining beams interfere destructively and photodiodes count the number of impinging photons.

As the spacetime interval is equal to zero for light ($ds^2 = 0$), we can demonstrate that the effect of a gravitational wave reaching the detector consists to stretch the detector arms so the distance travelled by the photons will be different in each arm [25]. The measured strain writes:

$$\frac{\Delta L}{L}(t) = h_+(t)F_+(\delta, \phi, \psi) + h_\times(t)F_\times(\delta, \phi, \psi) \tag{2.1}$$

where F_+ and $F_\times$ are the antenna beam pattern, (δ, ϕ) the position of the source in the sky[8] in spherical coordinates and ψ the polarization angle that characterizes the orientation between the polarization basis and the observer frame, see Figure 2.4. As the ratio of two distances, the strain $(\Delta L/L)(t)$ has no physical unit.

[25]: Maggiore (2007), *Gravitational Waves: Volume 1: Theory and Experiments*

8: As the Earth is rotating, the localization of the source should varies during the observation time. The observation time is suffiently short to suppose δ, ϕ and ψ to be constant for a given event and we neglect the time dependence. In practice the observation time is shorter than 1.5 seconds which suffices for this assumption to remain valid.

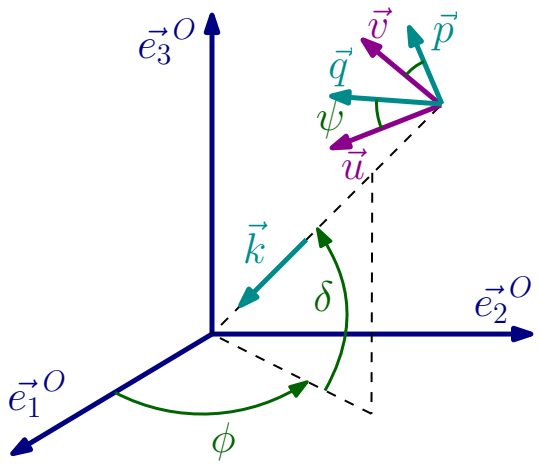

Figure 2.4: The wave frame $(\vec{p}, \vec{q}, \vec{k})$ is defined by the 3 angles (δ, ϕ, ψ) in the observer frame $(\vec{e}_1^{\,O}, \vec{e}_2^{\,O}, \vec{e}_3^{\,O})$. The position of the source in the sky is defined by (δ, ϕ) and the orientation of the polarization basis is characterized by ψ thanks to the introduction of a second wave frame $(\vec{u}, \vec{v}, \vec{k})$.

The observer frame $(\vec{e}_1^{\,O}, \vec{e}_2^{\,O}, \vec{e}_3^{\,O})$ is commonly identified to the equatorial coordinate system. The polarization basis tensor is defined in Section 2.1 with respect to $\vec{p}$ and $\vec{q}$, i.e. the x and y axes of the wave frame respectively. Their orientations are not known a priori by the observer ($\vec{p}$ and $\vec{q}$ are not observables). Thus we define a second wave frame $(\vec{u}, \vec{v}, \vec{k})$ associated to the propagation direction $\vec{k}$. Similarly, its x and y axes are such that

$$\vec{u} = \frac{\vec{e}_3^{\,O} \times \vec{k}}{|\vec{e}_3^{\,O} \times \vec{k}|} \quad \text{and} \quad \vec{v} = \vec{k} \times \vec{u}.$$

As illustrated in Figure 2.5, the polarization angle ψ is then the angle between the x (or y) axes of the two wave frames.

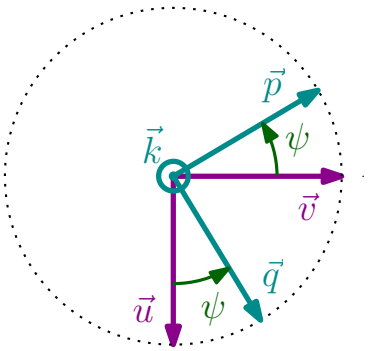

Figure 2.5: The polarization angle ψ connects the two wave frames: the wave frame defined in the source frame and the one defined in the observer frame. Here the plane containing $\vec{u}$ and $\vec{v}$ is viewed from above ($\vec{k}$ points towards the reader).

The antenna beam pattern ponderates the response of the detector depending on the incidence of the wave onto the instrument. Its derivation is straightforward: for $\vec{l}$ and $\vec{m}$ the perpendicular unit vectors aligned with the detector arms, the double dot product of the detector tensor $\overleftrightarrow{d} = (\vec{l} \otimes \vec{l} - \vec{m} \otimes \vec{m})/2$ with the polarization basis tensors gives $F_+ = \overleftrightarrow{d} : \overleftrightarrow{e_+} = d^{ab} e_{+\,ab}$ and respectively for $F_\times$. In the frame of the detector, i.e. for $\vec{e}_2^{\,O} = \vec{l}$ and for $\vec{e}_1^{\,O} = \vec{m}$, we get:

$$F_+(\delta, \phi, \psi) = \frac{1}{2}(1 + \cos^2\delta)\cos 2\phi \cos 2\psi - \cos\delta \sin 2\phi \sin 2\psi,$$
$$F_+(\delta, \phi, \psi) = \frac{1}{2}(1 + \cos^2\delta)\cos 2\phi \sin 2\psi - \cos\delta \sin 2\phi \cos 2\psi.$$

Figures 2.4 and 2.5 present the different angles involved in the antenna beam pattern formula.

The detection of gravitational waves constitutes a technical feat due to the size of the expected signal. Based on the arm

length (3 km), a detectable signal is of the size[9] $(\Delta L/L) \sim 10^{-21}$. Advanced technologies and a specific optical design are necessary to achieve this minimal target sensitivity.

Different upgrades have been implemented until the detector became operational for gravitational wave observations in 2017 under the project Advanced Virgo [26, 27]. This second generation detector is a dual-recycled Michelson interferometer with Fabry-Perot cavities in the arms, see Figure 2.2. The power of the bright fringe is recycled once by a semi-reflective mirror, i.e. the Power Recycling Mirror, between the input mode-cleaner and the Beam Splitter. The mirrors are suspended to a chain of pendulums and the laser beam operates under vacuum. Compared to the previous first generation detectors, the signal is recycled by adding a Signal Recycling Mirror between the Beam Splitter and the detection system. This broadens the bandwidth of the interferometer in the high frequency range of the detector.

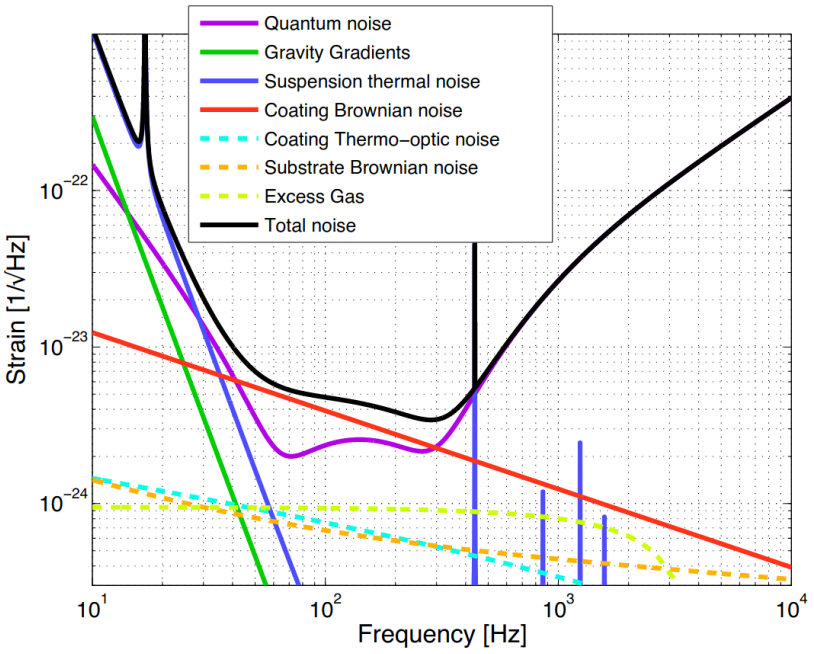

Figure 2.6: Advanced Virgo sensitivity and expected noise contributions in 2015 [28]. The Advanced Virgo sensitivity curve (solid black) is the summation of the different noise contributions.

Virgo is sensitive to gravitational waves for frequencies ranging from ~ 20 Hz to ~ 2000 Hz. At design sensitivity the noise floor of $3 \times 10^{-24}/\sqrt{\text{Hz}}$ is reached at 300 Hz. See Figure 2.6 for a review of the most limiting noise sources.

The low frequency sensitivity is limited by seismic noise and suspension thermal noise. Seismic noise is due to the motion of the Earth surface as well as to human activity while thermal noise is due to vibrations of the atoms that compose the mirrors and suspensions. The mid frequency sensitivity is mainly limited by thermal noise and quantum noise. Quantum noise originates from the quantum nature

9: As an analogy, it is equivalent to a variation as small as the thickness of a human hair between earth and Alpha Centauri, the closest star to our sun.

[26]: Acernese et al. (2015), *Advanced Virgo: a second-generation interferometric gravitational wave detector*
[27]: Acernese et al. (2020), *Advanced Virgo Status*

[28]: Accadia et al. (2012), *Advanced Virgo Technical Design Report*

of light and relates to the statistical counting uncertainty when measuring the power at the output part of the interferometer [25]. Above 300 Hz, the shot noise becomes the main limitation. The refraction induced by residual gazes in the tubes is limited by a ultra-high vacuum. Stabilized lasers are used to limit the fluctuations in the laser power and frequency. Light scattering is limited by an extreme polishing of the mirrors at a micro-roughness coating of exquisite optical quality. Electronic noise coupled with other noise sources can induce spurious non-stationary signals, named glitches, that are detected and classified.

2.2.2 A worldwide network of detectors

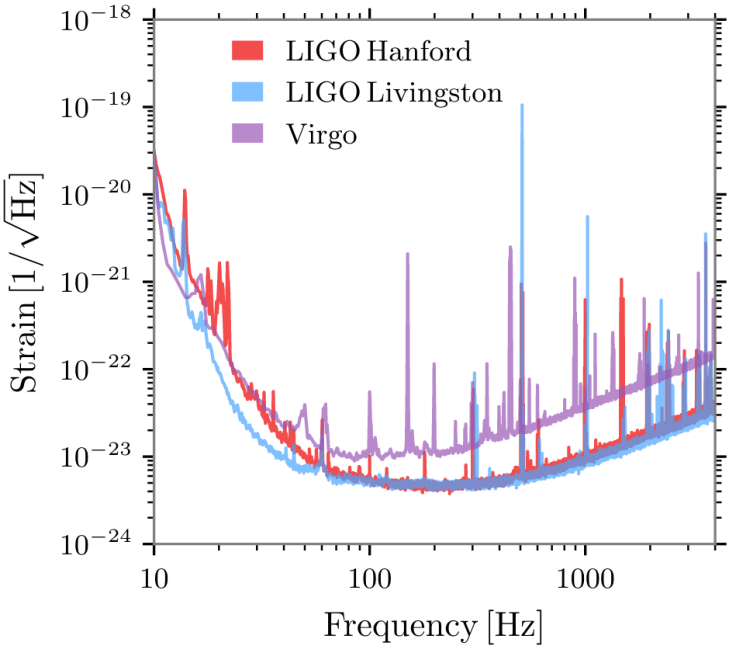

Figure 2.7: Representative sensitivity curves of LIGO and Virgo detectors during the third observing run [19]. Contrarily to the anticipated curve, these ones include calibration lines and the correponding harmonics.

Advanced Virgo is part of a network that also includes the two LIGO detectors based in the US: Advanced LIGO Hanford and Advanced LIGO Livingston. KAGRA[10], the Japanese second generation detector joined the collaboration for the third run and LIGO-India will be added to the list for the fifth. An overview of past and future plans for LIGO, Virgo and KAGRA detectors is presented in Figure 2.8.

10: KAGRA is short for Kamioka Gravitational Wave Detector, but is also a homophonic pun of the Japanese word KAGURA.

Upgrades of the instrument are done in between observing runs i.e. data collection campaigns for gravitational-wave astronomy purposes. The first detection of gravitational waves was announced in 2016 [18] after the first observing run O1. Virgo joined the LIGO detectors during the second observing run. The sensitivities obtained by LIGO and Virgo during the third observing runs are shown in Figure 2.7.

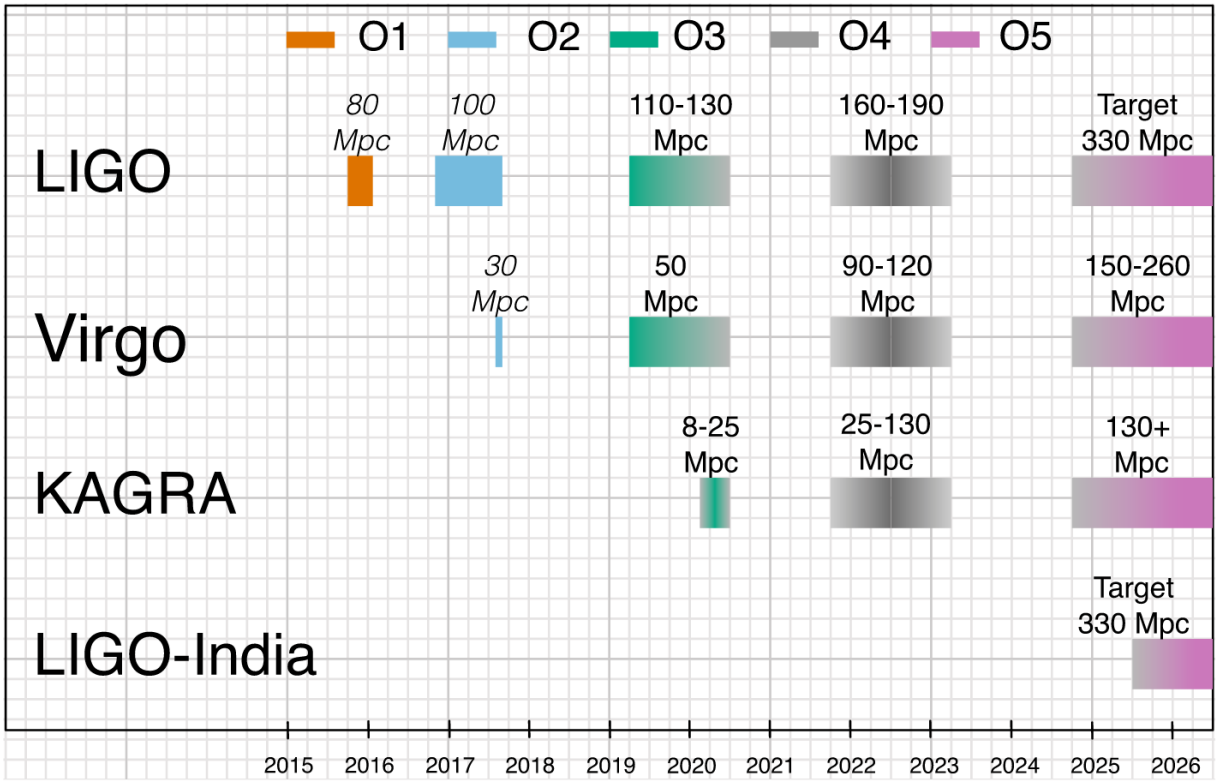

Figure 2.8: Review of the sensitivity of advanced LIGO, advanced Virgo and KAGRA for the past and future observing runs [29]. Detector sensitivities are given in terms of sensitive luminosity distance for a $1.4\,M_\odot + 1.4\,M_\odot$ binary neutron star system. The O4 and O5 runs have been rescheduled recently and postponed by six months with respect to what is shown here. The sensitivity of KAGRA has also been significantly revised.

There are obvious similarities between the instruments. For example, LIGO-India is a copy of LIGO observatories which will be located in India. However, there are important peculiarities. LIGO detectors are larger than Virgo and KAGRA. The formers have 4-km arms while the latters have 3-km arms. KAGRA is the first underground detector with cryogenic technology used to cool down the Fabry-Perot mirrors and reduce the thermal noise. The mirrors are made of saphir which has excellent properties at low-temperatures. Its undergrounding reduces drastically seismic noise.

2.2.3 Benefits of a detector network

The data collected by the instruments are shared and analysed in a joint effort within the LIGO-Virgo-KAGRA collaboration. The false alarm rate is reduced thanks to a coherent analysis and the duty cycle is increased. The network of detector is particularly important for the localization of the source. Knowing that gravitational waves travel at the speed of light, the time delays between the arrival at each detector are used in order to locate the source in the sky with triangulation

techniques. Using timing triangulation, a two detectors network can only conclude on an concentric ring between the two sites. A three detector network reduces the estimated location to two points and a four detector network is able to retrieve the exact sky location. In practice the time of arrivals are combined with other informations, such as the beam pattern of the detectors[11], which allows to draw credible regions on the sky with less than four instruments [29, 30].

Fast inference of sky location is particularly important in the case of mergers involving neutron stars. For the mergers of binary neutron stars or a neutron star with a black hole a short gamma-ray burst is theoretically emitted. We can use optical telescopes so as to follow a possible electromagnetic counterpart associated to a gravitational wave emission. The coordinated observation of gravitational and electromagnetic radiations is at the core of multi-messenger astronomy. It is a unique opportunity to study cosmology and the physics of astrophysical compact objects.

11: As the detectors are located in different geographical areas, they have different responses for a given source, see (2.1) and Figure 2.9. The presence or the lack of signal in one detector gives a hint on the possible location of the source. For instance GW170817 reached Virgo close to 45 degrees, so Virgo was not observing the signal but this information was critical for localization.

[29]: Abbott et al. (2020), *Prospects for observing and localizing gravitational-wave transients with Advanced LIGO, Advanced Virgo and KAGRA*

[30]: Fairhurst (2018), *Localization of transient gravitational wave sources: beyond triangulation*

2.2.4 Future observatories

There are plans to improve the sensitivity of the detectors even further. Detectors will have higher sensitivity (about one order of magnitude) and allow to expand the observation to more massive sources. Einstein Telescope is a third generation European gravitational wave detector project with an underground infrastructure (beyond a total mass of ~ 200 in solar mass $M_\odot$, as allowed by current detectors). The detector will have 10-km arms with cryogenic cooling system, quantum technologies to reduce the fluctations of light and active noise mitigation systems. Cosmic Explorer is a similar US project with two sites, one with 40-km arms and one with 20-km arms. The idea is to increase the amplitude of the observed signal with no increase in the noise by expanding the arm lengths. Einstein Telescope and Cosmic explorer strive to observe compact-object binaries from $10^3\,M_\odot$ to $10^4\,M_\odot$. Finally LISA is a large-scale space mission of the European Space Agency designed for mergers of massive black holes at the center of galaxies, extreme mass ratio inspirals and speculative astrophysical objects such as cosmic strings. The instrument will be a constellation of three satellites in heliocentric orbits forming three space interferometers with arms of 2.5 million km. It will chase sources between $10^7\,M_\odot$ and $10^{10}\,M_\odot$. Due to the extreme sensitivity, the data collected

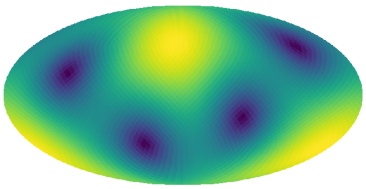

Figure 2.9: Antenna pattern of Virgo (Mollweide projection) in the equatorial coordinate system. The colors of each sky pixel is determined by

$$\sqrt{F_+^2(\delta,\phi,\psi)+F_\times^2(\delta,\phi,\psi)}.$$

The power antenna pattern is independent with respect to ψ. High values ~ 1 are in yellow and small ones ~ 0 are in blue. The maximum values are for signals coming from overhead or underfoot.

will consist of superpositions of gravitational signals from possible millions of sources.

2.3 Gravitational wave detections

Advanced LIGO and Advanced Virgo detectors have performed three rounds of data acquisition campaigns: O1, O2 and O3. The signals detected by the LIGO-Virgo-KAGRA collaboration are listed in the Gravitational Wave Transient Catalog GWTC-3 [19]. A total of 90 gravitational waves have been detected so far. This includes sources at distances ranging from 40 Mpc to 6 Gpc. All the sources are compact-object binaries composed of stellar-mass black holes and neutron stars with masses from 1.2 $M_\odot$ to 106 $M_\odot$. This section reviews the three data taking campaigns through some examples of noteworthy detections. The gravitational-wave signature from the merger of two compact stars will be detailed later in Section 2.4.2.

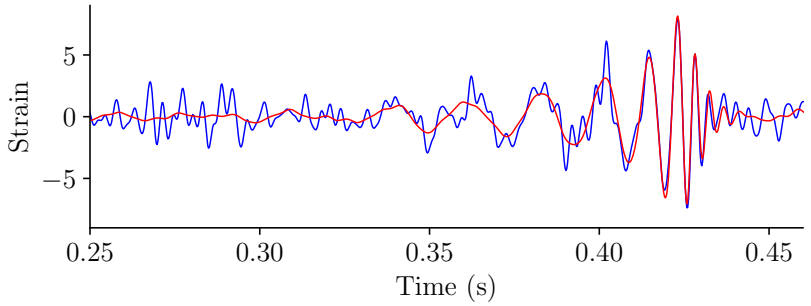

Figure 2.10: Whitened observations (blue) and matched filter template (red) of GW150914 for LIGO Hanford detector.

GW150914 Three events have been detected during O1. Among them, GW150914 [18] is the first gravitational-wave signal ever detected. It is also the first observation of the coalescence of two black holes. The strain was produced by the merger of two black holes 440 Mpc away from Earth. The two objects were around 36 $M_\odot$ and 31 $M_\odot$, reaching $\sim$ 60% of the speed of light before the final merger. The remnant is a black hole of 63 $M_\odot$. 3 $M_\odot$ were converted into gravitational radiation observed by the LIGO detectors for a duration of 0.2 s. GW150914 proved the existence of BBHs (binaries of black holes). The announcement of its confident detection in 2016 [18] marked the birth of gravitational-waves astronomy. Figure 2.10 presents a whitened data sample of LIGO Hanford corresponding to GW150914 data segment.

GW170817 Among the 8 confident detections made during O2 by LIGO and Virgo, GW170817 [31] is the first ever detected gravitational-wave from a binary neutron star. Because of the relatively small mass of the binary, the observed signal (visible for 100 s) is primarily related to the inspiral phase of the coalescence ; the merger and postmerger are not in the sensitive band of the instruments. GW170817 is also the first multi-messenger observation [32] as a range of electromagnetic counterparts have been observed together with gravitational waves. For example, 1.7 s after the merger time, the Fermi Gamma-ray Space Telescope and the International Gamma-Ray Astrophysics Laboratory (INTEGRAL) spacecraft detected a gamma-ray burst that also originated from the BNS (binary neutron star) merger. Multimessenger observations can bring tremendous contributions through several aspects, e.g. it is an alternative way to measure the Hubble constant [33] and test general relativity [34]. The electromagnetic observation provides important information on a long standing question concerning the production of such heavy elements such as gold and platinium, found to be produced in the aftermaths of BNS mergers. Another BNS merger was observed during O3, however no electromagnetic counterpart was detected.

[31]: Abbott et al. (2017), *GW170817: Observation of Gravitational Waves from a Binary Neutron Star Inspiral*

[32]: Abbott et al. (2017), *Multi-messenger Observations of a Binary Neutron Star Merger*

[33]: Abbott et al. (2017), *A gravitational-wave standard siren measurement of the Hubble constant*

[34]: Abbott et al. (2019), *Tests of General Relativity with GW170817*

GW200105 During the third observing run, two mixed binary mergers were observed for the first time, i.e. NS-BH (black hole - neutron star binary) coalescences, and GW200105 is the first [35]. The nature of the objects is deduced by the inferred component masses, about 8.9 $M_\odot$ and 1.9 $M_\odot$. The merger have taken place at 280 Mpc. It is an opportunity to study matter under extreme conditions and the formation channels of such binaries.

[35]: Abbott et al. (2021), *Observation of Gravitational Waves from Two Neutron Star–Black Hole Coalescences*

GW190412 A total of 79 signals were detected during O3. GW190412 is different from the other observations due to the asymmetric mass distribution among the two black holes: $\sim 30\,M_\odot$ and $\sim 8\,M_\odot$. The mass ratio of 0.26 allowed to observe subdominant modes [36]. It is the first signal with marginal hints of orbital precession. The source parameters are in a previously unobserved region of the parameter space, for which we lack an accurate waveform model. With the scheduled increase in sensitivity of second generation instruments, we expect to see more of those events with detectable higher order modes as well as precession induced modulation in future detections.

[36]: Abbott et al. (2020), *GW190412: Observation of a binary-black-hole coalescence with asymmetric masses*

2.4 Basics of compact binary coalescences

2.4.1 Phenomenology

We did not characterize how gravitational waves are emitted, nor what are their sources. The emission of gravitational waves from a physical system can be estimated to first order by the "quadrupole formula" [25]. This formula establishes that gravitational wave radiation requires the temporal variation of the mass quadrupole. This implies that gravitational wave sources necessarily have a non-spherically symmetric mass distribution. Stellar binaries is possibly the simplest astrophysical system with this property. In the context of ground-based detectors such as Virgo and LIGO that observe in the frequency band around 100 Hz, we concentrate on binaries of stellar-mass compact objects (neutron stars and black holes) – referred to as compact binaries – that can possibly generate gravitational waves in this frequency region. Compact binaries are the only gravitational wave source detected so far, as discussed in Section 2.3.

Compact binaries gradually lose gravitational potential energy through gravitational radiation. This causes their orbital separation to decay until the two objects merge into a remnant, generally a black hole. The binary passes through three different dynamical regimes during this coalescence process. Initially, the two objects are far apart, and following slowly shrinking quasi-circular orbits: this is the inspiral phase. When the system reach the innermost last stable orbit [25] the two objects "plunge" onto each other and merge: this is the merger phase. The merger remnant settles down to equilibrium: this is the ringdown phase.

2.4.2 Gravitational-wave signature

The gravitational wave signal is directly related to the source dynamics. The three dynamical regimes described above are visible in the waveform, see Figure 2.11.

Gravitational wave signature appears to be a amplitude and frequency modulated signal. The frequency and amplitude follow a specific time evolution. To leading order, the instantaneous frequency of the waveform can be approximated as a power law[12]

12: This is usually referred to as the Newtonian approximation.

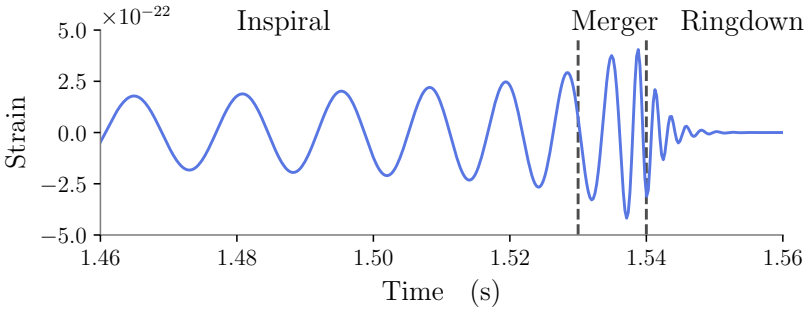

Figure 2.11: The three dynamical regimes of a binary of compact objects seen in a simulated strain.

$$f_{\mathrm{GW}}(t) = \frac{1}{\pi}\left(\frac{5}{256}\frac{1}{(t_{\mathrm{coal}}-t)}\right)^{3/8}\left(\frac{G\mathcal{M}}{c^3}\right)^{-5/8},$$

for $t < t_{\mathrm{coal}}$, where t_{coal} is the merger time.

At this crude approximation order, the frequency evolution solely depends on the chirp mass $\mathcal{M} = (m_1 m_2)^{3/5}/(m_1 + m_2)^{1/5}$ [25] with the binary components masses m_1 and m_2. The plunge and merger occur when the binary reaches the Innermost Stable Circular Orbit (ISCO) [25], associated with the frequency

$$f_{\mathrm{ISCO}} \sim 2.2\,\mathrm{kHz}\left(\frac{M}{M_\odot}\right)^{-1}, \tag{2.2}$$

where $M = m_1 + m_2$ is the total mass.

The merger phase results in a deformed black hole remnant which "rings" analogously to an elastic body and radiates gravitational waves at characteristic frequencies corresponding to its quasi normal modes, typically

$$f_{\mathrm{QNR}} \sim 885\,\mathrm{Hz}\left(\frac{M}{M_\odot}\right)^{-1}$$

for a rotating black hole with a dimensionless spin of[13] 0.7. This is the maximum frequency reached by the gravitational-wave signal. This frequency is in the observable band when $M > 450\,M_\odot$.

The signal duration in the detection frequency band (from 20 Hz to few kHz) depends on the component masses. The mass of a neutron star is typically between $\sim 1.1\,M_\odot$ and $\sim 2.1\,M_\odot$[14], while stellar-mass black holes have a much wider mass span ranging from $5\,M_\odot$ to $100\,M_\odot$. The in-band duration is a fraction of a second for black-hole binaries, while the signal can last few tenths of seconds for neutron-star binaries.

13: This is the typical spin range for black holes formed by mergers.

14: $M_\odot$ denotes the mass of the Sun.

Using the quadrupole formula, the amplitude of the gravitational wave strain can be estimated as

$$\Delta L/L \sim 4.1 \times 10^{-22} \left(\frac{\mathcal{M}}{M_\odot}\right)^{5/6} \left(\frac{100\,\mathrm{Mpc}}{D}\right) \left(\frac{100\,\mathrm{Hz}}{f_{\max}}\right)^{-1/6},$$

where D is the luminosity distance in Mpc between the source and the observer.

Section 3.2.1 goes beyond the crudle and high level description given here, and reviews the various waveform approximants that have the required accuracy to analyse the data today.

2.5 Summary

Gravitational-wave astronomy is a new way to observe the universe via the warping of space-time induced by the motion of massive objects. It already gave precious informations about the existence of black holes and the coalescence of compact bodies as well as opportunities to test fundamental physics.

At this date, 90 signals have been detected with sources from $1.2\,M_\odot$ to $106\,M_\odot$ at distances up to 6 Gpc. The vast majority of detected events were emitted by BBHs. 2 BNS and 2 BH-NS coalescences have been detected. Electromagnetic counterparts have also been observed in association with the BNS merger GW170817, it is the first multi-messenger astronomy event involving gravitational waves.

Gravitational waves are bivariate signals, being particularly adapted to the formalism introduced in Chapter 1. As shown in Chapters 3 and 4, we can take advantage of the new formalism introduced separately by Flamant and Lilly [7, 12] to develop new data analysis techniques in the context of gravitational-wave astronomy.

3 Fast generation of gravitational waveforms

Gravitational-wave astronomy has given access to a range of astrophysical objects in an unprecedent way by analysing the ripples of spacetime with implications in astrophysics, cosmology and possibilities to test theories as general relativity [37–39].

[37]: Kimball et al. (2021), *Evidence for Hierarchical Black Hole Mergers in the Second LIGO–Virgo Gravitational Wave Catalog*
[38]: The LIGO Scientific Collaboration et al. (2022), *Tests of general relativity with GWTC-3*
[39]: The LIGO Scientific Collaboration et al. (2021), *The population of merging compact binaries inferred using gravitational waves through GWTC-3*

The number of detected signals is expected to increase with the technical upgrades of the current instruments as well as the addition of new observatories in the global network. The LIGO-Virgo detector network performed three observing runs over the last seven years. Among the 90 detections, 86 originate from binary black hole mergers. These are all opportunities to study compact objects through the prism of gravitational-wave astronomy.

Gravitational-wave modelling is a building block in order to draw conclusions based on the observations of the detectors. Theoretical waveforms are compared with observations by Bayesian data analysis pipelines, drawing posterior probabilities for parameter estimation and applying hypothesis testing.

This chapter is dedicated to the generation of gravitational waveforms with machine learning models. We address the case of waveform modelling for spin-aligned and precessing BBH sources. The core of the methods is based on a judicious choice of signal representation, which leads to the introduction of waveform attributes with smooth variations with respect to the source parameters. The appropriateness of the representation makes possible the use of standard machine learning methods to get an operable waveform generator.

We first start by briefly reviewing the current state of gravitational wave data analysis to establish the context and motivations.

3.1 Gravitational-wave data analysis in a nutshell

3.1.1 Search for gravitational-wave transients

Several approaches are used to detect gravitational-wave signals. For example, GW150914 was initially detected with coherent WaveBurst pipeline [40, 41] which is an unmodeled search algorithm identifying clusters of excess power in wavelet transforms with different resolutions. While the unmodeled approach provides a way to detect unanticipated signals such as GW150914, standard matched filtering techniques are widely used in the gravitational-wave data analysis [42, 43]. Matched filtering pipelines are less flexible but more sensitive to weaker signals. For a detector d, the matched filtering detection statistic is given by

$$\rho_d(t) = \max_{\vartheta\in\Theta} 2\,\mathrm{Re}\int_{\Omega_d} \frac{X_d(f)H^*_\vartheta(f)}{S_d(f)} e^{2i\pi ft}\mathrm{d}f \qquad (3.1)$$

called signal-to-noise ratio (SNR), where S_d is the estimated power spectral density of the noise, X_d and H_ϑ are the Fourier transfoms of the recorded signal x_d and a waveform template h_ϑ associated to a set of physical parameters ϑ. The frequency domain Ω_d over which the integral is computed is determined by the bandwith of the detector's data. Θ is a fixed collection of parameter sets, it is constructed in order to pave the region of expected signals[1]. The network SNR is defined as

$$\rho_{\mathrm{net}}(t) = \sqrt{\sum_d \rho_d{}^2(t)}.$$

It combines the SNR of individual detectors and is used to assess the False Alarm Rate. These two statistics strongly depend on the validity of the template bank and thus on the waveform approximants.

The network SNR is a detection statistics which can be involved in the computation of the p-value used to define confident detections. The p-value ranks the significance of a candidate event being a gravitational wave comparatively to the rate at which the detectors produce noise with the same detection statistics. Its computation needs to estimate the noise background, which is a difficult task knowing that the noise is not really stationary nor Gaussian and that it is impossible to configure the detectors to have signal-free

[40]: Klimenko et al. (2004), *A wavelet method for detection of gravitational wave bursts*
[41]: Klimenko et al. (2016), *Method for detection and reconstruction of gravitational wave transients with networks of advanced detectors*
[42]: Usman et al. (2016), *The PyCBC search for gravitational waves from compact binary coalescence*
[43]: Cannon et al. (2012), *Toward early detection of gravitational waves from compact binary coalescence*

1: Note that the template bank used for detection is fixed and is not necessarily sampled regularly over the binary parameters.

measurements. It is considered that the p-value is under the detection threshold for roughly $\rho_{\rm net}(t) > 8$.

3.1.2 Inference of source parameters

Once the signal has been detected, the nature and the properties of the sources are inferred from the observations made by gravitational wave detectors. The waveform properties are closely connected to the source parameters. For instance, the masses of the objects can be inferred from the frequency evolution of the signal. The luminosity distance (the distance from the source to the observer) can be inferred from the amplitude. The sky location of the source can be retrieved from the differences between the time of arrival at each detector. From the amplitude and phase modulations (i.e. polarization modulations, see Chapter 4) we can infer spins and orbital eccentricity.

The Bayesian formalism is particularly adapted for parameter inference and hypothesis testing. It derives from the Bayes' theorem and standard rules of probability theory. For two statistical events A and B the Bayes' theorem reads

$$\mathbb{P}(B|A) = \frac{\mathbb{P}(A|B)\mathbb{P}(B)}{\mathbb{P}(A)}.$$

For some observed data A and hypothesis B, $\mathbb{P}(A|B)$ is the likelihood of A given B, $\mathbb{P}(B|A)$ is the posterior distribution i.e. the updated version of the prior distribution $\mathbb{P}(B)$ accounting the new information broughtby the data A and $\mathbb{P}(A)$ is the marginal likelihood or model evidence.

In the context of gravitational wave data analysis, we want to infer source parameters ϑ (e.g. masses, spins etc.) given a set of observed data x, a model $\mathscr{H}$ and a prior information I. Bayes' theorem gives the posterior density function

$$\mathbb{P}(\vartheta|x,\mathscr{H},I) = \frac{\mathbb{P}(x|\vartheta,\mathscr{H},I)\mathbb{P}(\vartheta|\mathscr{H},I)}{\mathbb{P}(x|\mathscr{H},I)}. \tag{3.2}$$

The denominator is often neglected as it applies to all parameter sets in the parameter space[2].

For a given event, the detector observation is a gravitational wave signal s corrupted by an additive noise[3]: $x(t) = s(t) + n(t)$. The noise is supposed to be a Gaussian and stationary process with zero mean on a short time segment around the event. The likelihood is generally computed on

2: The important relation is $\mathbb{P}(\vartheta|x,\mathscr{H},I) \propto \mathbb{P}(x|\vartheta,\mathscr{H},I)\mathbb{P}(\vartheta|\mathscr{H},I)$. Computation of the normalization factor for the posterior estimate is straightforward. As a matter of fact, Bayesian methods can be applied without insuring that each considered "density" sums to one.

3: As mentioned in Chapter 2 $s(t) = F_+(\Theta)h_+(t) + F_\times(\Theta)h_\times(t)$ where $h_{+,\times}$ are the waveforms associated to each polarization mode and $F_{+,\times}(\Theta)$ the antenna beam pattern of the detector.

the frequency domain. In this case, the noise variance is given by the noise power spectral density $S_n(\omega)$, where ω is the frequency variable. The likelihood is then given by a multivariate Gaussian distribution

$$-\log \mathbb{P}(x|\vartheta, \mathscr{H}, I) \propto \sum_{\omega} |x(\omega) - s(\omega)|^2 / S_n(\omega). \tag{3.3}$$

3.1.3 Bayesian samplers in the context of gravitational-wave astronomy

While the algorithms based on standard matched filtering uses a fixed lattice of waveforms paving the space of possible signals [42], Bayesian inference techniques sample adaptatively ϑ using standard Bayesian sampler such as Metropolis Hastings or nested sampling in order to build a posterior density estimate [44, 45]. About 10^5 to 10^6 theoretical waveforms are required to cover a sufficient portion of the parameter space.

[44]: Cornish et al. (2015), *Bayeswave: Bayesian inference for gravitational wave bursts and instrument glitches*

[45]: Thrane et al. (2019), *An introduction to Bayesian inference in gravitational-wave astronomy: Parameter estimation, model selection, and hierarchical models*

[46]: Veitch et al. (2015), *Parameter estimation for compact binaries with ground-based gravitational-wave observations using the LALInference software library*

Two main software packages are available for parameter inference: LALInference [46] and Bilby [45].

Parameter estimation is computationally highly demanding. The analysis of a single event requires from tenths of hours at best to days for a single run. Computations related to waveform generation dominate this cost.

In the next decade, LIGO and Virgo detectors are expected to conduct at least two major observing runs with improved sensitivity, leading to a large increase in the number of detected signals. The analysis of those future observations calls for numerically efficient, yet accurate waveform generators. In this context, this chapter is dedicated to the acceleration of source's parameters estimation through the development of fast generation method of theoretical waveforms.

3.2 Binary black hole coalescences

Stellar collapse through supernova explosion can leave as remnant a compact object. Depending on the mass of the progenitor, it can be either a white dwarf, a neutron star or a stellar-mass black hole. It is considered that remnants with mass higher than $\sim 3\,M_\odot$ are more likely to be black holes.

Black holes may form in binary systems, thus leading to a black hole binary. It consists in two objects of masses[4] m_1 and m_2, with spin angular momentums $\vec{S}_1(t)$ and $\vec{S}_2(t)$, which are orbiting each other with an angular momentum $\vec{L}(t) = \mu\,\vec{r}(t) \times \vec{p}(t)$, where $\vec{r}(t)$ and $\vec{p}(t)$ are the orbital separation and its canonically conjugate momentum [47] respectively. The system loses energy through emission of gravitational radiations which causes the orbital separation to decrease and the orbital frequency $\Omega_{\rm orb}(t) = |\vec{r} \times \dot{\vec{r}}|/|\vec{r}|^2$ to increase until they merge.

4: The first and second objects are chosen such that the mass ratio $q = m_1/m_2 \geqslant 1$.

[47]: Pan et al. (2014), *Inspiral-merger-ringdown waveforms of spinning, precessing black-hole binaries in the effective-one-body formalism*

Different scenarios are anticipated for the formation of black hole binaries (see [48] for a recent review). This results in different binary properties, regarding the orientation of the object spins or the separation of the two bodies. We mainly differentiate between two configurations:

[48]: Mapelli (2020), *Binary Black Hole Mergers: Formation and Populations*

Spin-aligned BBHs Certain BBH formation scenarios favor spin-aligned (or anti-aligned) configurations, e.g. isolated BBHs from binary star systems. In this case, the black holes created are likely to have spins close to being aligned. Moreover, the spins of black holes orbiting each other tend to align themselves in the long time as the system loses energy by emitting gravitational radiation [49, 50]. In this case, $\vec{L}(t)$ and $\vec{J}(t) = \vec{L}(t) + \vec{S}_1(t) + \vec{S}_2(t)$ are both normal to the orbital plane which thus remains fixed with respect to an inertial observer.

[49]: Rodriguez et al. (2016), *Illuminating black hole binary formation channels with spins in advanced LIGO*
[50]: Gerosa et al. (2018), *Spin orientations of merging black holes formed from the evolution of stellar binaries*

Precessing BBHs Other binary formation scenarios lead to the misalignment of at least one of the component spins with respect to the normal of the orbital plane. Let us define the Newtonian orbital angular momentum $\vec{L}_N(t) = \mu\,\vec{r}(t) \times \dot{\vec{r}}(t)$, which is normal to the orbital plane by construction[5]. During the orbital motion, $\vec{L}(t)$, $\vec{L}_N(t)$ and the spin $\vec{S}_1(t)$ and $\vec{S}_2(t)$ undergo a precession movement around the total angular momentum $\vec{J}(t)$, see Figure 3.1. In this more generic configuration, the orientation of the line of sight compared to the orbital plane is varying with time. The main difference bewteen $\vec{L}(t)$ and $\vec{L}_N(t)$ is that, while the head of the former draw a circle around the total angular momentum, the latter exibit an additional nutation as the two bodies are orbiting.

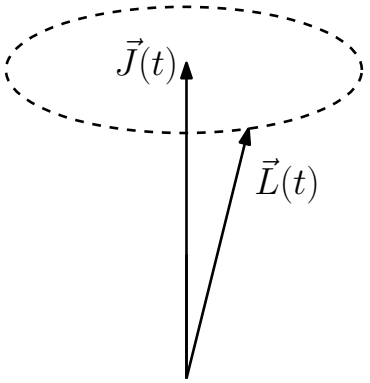

Figure 3.1: Precession of the orbital plane induced by the misalignment of the spin of at least one of the two bodies. The angular momentum $\vec{L}(t)$ precess around the total angular momentum $\vec{J}(t)$.

The large majority of the observed sources presented in Section 2.3 are compatible with the first case (aligned spin)

5: In general, the orbital angular momentum $\vec{L}(t)$ of a spinning binary is not orthogonal to the orbital plane while it is always the case for $\vec{L}_N(t)$.

but there are few cases where the component spins appear to be misaligned.

3.2.1 Gravitational waveforms

It is customary to present gravitational waves as complex valued signals:

$$h(t) = h_+(t) - \boldsymbol{i} h_\times(t),$$

in particular for analytic developments. When modelling the signal for a given source it is convenient to decompose h using a spin weighted spherical harmonics expansion:

$$h(t) = \frac{M}{D} \sum_{l=2}^{\infty} \sum_{m=-l}^{l} h^I_{l,m}(t)\, {}_{-2}Y_{l,m}(\iota, \varphi_0) \tag{3.4}$$

where the ${}_{-2}Y_{l,m}(\iota, \varphi_0) \in \mathbb{C}$ are the -2 spin weighted spherical harmonics[6] and the $h^I_{l,m}(t) \in \mathbb{C}$ are the associated modes. The spin weighted spherical harmonics are functions of ι and φ_0, respectively the inclination and initial phase[7] of the source in an inertial source frame denoted I, see Figure 3.2. M and D are respectively the total mass and the luminosity distance in geometrical units ($G = c = 1$).

It is worth noticing that Equation (3.4) outlines that the line of sight (in the inertial frame) influences the value of each spin weighted spherical harmonics ${}_{-2}Y_{l,m}(\iota, \phi)$ whereas the different modes $h^I_{l,m}(t)$ result from the source dynamics.

A number of theoretical models allow to compute the waveform modes of (3.4) related to initial source conditions by approximating solutions of the source dynamics [53]. There are no exact close-form solution for this relativistic problem, however accurate approximations are available.

3.2.2 Review of available waveform approximants

Gravitational-wave signals are approximated by a range of analytic and numerical techniques which define waveform families. Depending on the approach, the strain is approximated with different accuracies and their computation lead to different runtimes. Two main waveform families (Effective-One-Body and Phenomenological approximants detailed below) allow to compute the waveform associated with the

[51]: Ossokine et al. (2020), *Multipolar effective-one-body waveforms for precessing binary black holes: Construction and validation*

[52]: LIGO Scientific Collaboration (2018), *LIGO Algorithm Library - LALSuite*

6: See Appendix B for a short introduction to spin weighted functions and spin weighted spherical harmonics.

7: Our convention originates from [51]. Here $\varphi_0 = \pi/2 - \Phi_{\text{ref}}$ where Φ_{ref} is the reference phase in the `LALSimulation` conventions [52].

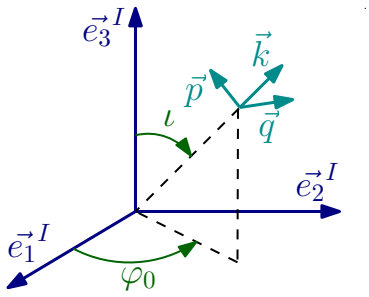

Figure 3.2: Line of sight in the inertial source frame $(\vec{e}^I_1, \vec{e}^I_2, \vec{e}^I_3)$. The inclination ι and the initial phase φ_0 are the spherical coordinates of the propagation direction $\vec{k}$ in the inertial source frame. The wave frame is constructed such that its z-axis is aligned with $\vec{k}$.

[53]: Schmidt (2020), *Gravitational Waves From Binary Black Hole Mergers: Modeling and Observations*

entire coalescence process, including the three dynamical phases : inspiral, merger and ringdown.

Post-Newtonian Theory and Numerical Relativity The post-Newtonian (PN) [54] and numerical relativity (NR) [55] formalisms are the major building blocks on which the waveform families rely. For the inspiral phase, PN expansions of the equations of motion at low velocities provides accurate predictions till the orbital velocity becomes comparable to the speed of light. NR are fully relativistic numerical resolution of the Einstein field equations. They are acccurate including in the highly non-linear regime of the merger phase, but requires very expensive computing ressources. NR waveforms are used to calibrate other models and create NR surrogates.

[54]: Blanchet (2014), *Gravitational Radiation from Post-Newtonian Sources and Inspiralling Compact Binaries*

[55]: Boyle et al. (2019), *The SXS collaboration catalog of binary black hole simulations*

Effective-One-Body approximants [21] The Effective-One-Body (EOB) formalism maps the two-body problem onto an effective one-body problem [21]. This mapping reduces the problem to a single test particle in a deformed Schwarzschild metric with deformation parameter equal to the symmetric mass ratio $\nu = \mu/M$. This "mapping trick" allows to accurately resolve the source dynamics from the inspiral through the merger phase. A complete waveform is obtained by stitching the adequate quasi-normal mode expected during the ringdown phase. This approach works inherently in the time domain, and requires the resolution of dynamical equations that are computationally slow to evaluate. Waveform approximants based on EOB are available for non-spinning and spin-aligned binaries, but also for binaries with precessing and eccentric orbits [56].

[56]: Hinderer et al. (2017), *Foundations of an effective-one-body model for coalescing binaries on eccentric orbits*

Phenomenological approximants [57] The phenomenological framework is initially based on the waveform obtained for the inspiral phase by the post-Newtonian expansion of general relativity in the weak field regime, i.e. for small velocities [54]. This initial waveform is expanded in the merger and ringdown phases by a generic (polynomial and Lorentzian) model which is fitted against the finite set of numerical relativity simulations available today. This operation is done in the frequency domain, so that the phenomenological waveforms provide closed-form expressions of the signal in frequency that are fast to compute and convenient for the data analysis.

[57]: Ajith et al. (2007), *A phenomenological template family for black-hole coalescence waveforms*

3.2.3 Waveform parametrization

The source parameters that impact the dynamics are the masses m_1, m_2 and spins $\vec{S}_1(t_0)$, $\vec{S}_2(t_0)$ of each object, where t_0 refers to a given initial time. By convention we use the dimensionless spins $\vec{\chi}_i(t_0) = \vec{S}_i(t_0)/{m_i}^2$ for $i = 1, 2$ in the computation of waveform models. Thus the system is parametrized by

$$\vartheta = \left\{m_1, m_2, \chi_{1x}, \chi_{1y}, \chi_{1z}, \chi_{2x}, \chi_{2y}, \chi_{2z}\right\},$$

where $\chi_{ix}, \chi_{iy}, \chi_{iz}$ are the coordinates in the source frame I of the dimensionless spin $\vec{\chi}_i(t_0)$. ϑ is the set of parameters "intrinsic" to the physical system while ι, φ_0 and D are "extrinsic" parameters (that depend on the observer).

General relativity's scale invariance implies[8] $h(t; m_1, m_2) = h(\lambda t; \lambda m_1, \lambda m_2)$ [58]. So in practice the intrinsic parameter set can be reduced to[9] $\vartheta = \left\{q, \chi_{1x}, \chi_{1y}, \chi_{1z}, \chi_{2x}, \chi_{2y}, \chi_{2z}\right\}$ where q is the mass ratio (defined as $q = m_1/m_2$ and with $q \geqslant 1$). Waveform models compute separately each waveform mode $h^I_{l,m}$ (in time or frequency domain) for a given ϑ, and compute the waveform with (3.4) and the proper time rescaling.

Sections 3.3 and 3.4 use this remark to construct fast and accurate generative models of time-domain gravitational waveforms using machine learning: the extrinsec parameters used in the training stage (i.e. the total mass, the luminosity distance and the line of sight) are fixed such that $M^* = 20\,M_\odot$, $r^* = 1\,\mathrm{Mpc}$, $(\iota^*, {\varphi_0}^*) = (0, 0)$.

8: By convention, the time grid is such that $t = 0$ at the merger of the two objects.

[58]: Bohé et al. (2017), *Improved effective-one-body model of spinning, nonprecessing binary black holes for the era of gravitational-wave astrophysics with advanced detectors*

9: Or, as we will see, for spin-aligned BBHs $\vartheta = \{q, \chi_{1z}, \chi_{2z}.\}$.

3.2.4 Waveform approximation accuracy measure

Errors in the waveform approximation lead to systematic errors in the astrophysical parameters estimates obtained from the observations. Systematic errors from mis-modeling should be smaller than the statistical errors due to the presence of noise in the observations.

The waveform approximation accuracy is measured by the mismatch measure ε, which writes

$$\varepsilon\,(h, g) = \min_{\tau \in \mathbb{R}} \left[1 - \frac{|\langle h_\tau, g\rangle|}{\|h_\tau\|\,\|g\|}\right] \tag{3.5}$$

for h, g two given complex-valued waveforms and $h_\tau(t) = h(t-\tau)$. ϵ is a common measure to test waveform accuracy in gravitational wave data analysis [58]. It is time-shift and phase-shift invariant. The scalar product is computed in the frequency domain as

$$\langle h, g\rangle = \int \frac{H(\omega)\overline{G(\omega)}}{S(\omega)} \mathrm{d}\omega,$$

where ω is the frequency variable and H and G are respectively the Fourier transforms of h and g. $S(\omega)$ is a frequency dependent weighting that is usually fixed to the gravitational-wave detector noise power spectrum density. As we do not want to favour certain frequencies for the evaluation of the model performances, we made the conservative assumption of a flat noise curve[10] $S(\omega) = 1$.

Error in the waveform modelling can be seen as a systematic error. A rule of thumb (see e.g., Appendix G of [59]) tells at which mismatch the systematic error dominates over the statistical error due to the random noise. This rule states that the mismatch should be strictly smaller than statistical error $N/(2 \times \mathrm{SNR}^2)$ where N is the effective number of intrinsic parameters and SNR is the signal-to-noise ratio. In the next observing runs of LIGO-Virgo-KAGRA collaboration detectors, it is expected to see events with SNR going up to 50 typically. For spin aligned BBHs with $N = 3$ effective parameters and precessing BBHs with $N = 7$, this defines a targeted accuracy of $\varepsilon \leqslant 10^{-5}$ and $\varepsilon \leqslant 10^{-4}$ respectively.

[58]: Bohé et al. (2017), *Improved effective-one-body model of spinning, nonprecessing binary black holes for the era of gravitational-wave astrophysics with advanced detectors*

10: It would be straightforward to compute ε in (3.5) with a given noise curve.

[59]: Chatziioannou et al. (2017), *Constructing Gravitational Waves from Generic Spin-Precessing Compact Binary Inspirals*

3.3 Spin-aligned binary black holes

Non-precessing BBH mergers are the most common type of sources detected by the LIGO-Virgo Collaboration [60]. They are BBHs for which each object has a spin[11], respectively $\vec{S}_1(t)$ and $\vec{S}_2(t)$, aligned (or anti-aligned) with the orbital angular momentum $\vec{L}(t)$ as represented in Figure 3.3. In this case, the orbital plane remains fixed during the coalescence. $\vec{L}(t)$ is normal to the orbital plane and is used to define an inertial frame I attached to the source. For a given time t_0 we define a basis $(\vec{e}_1^I, \vec{e}_2^I, \vec{e}_3^I)$ such that the z axis of the frame is aligned with the angular momentum, i.e. $\vec{e}_3^I \equiv \vec{L}(t_0)$, and the x axis points from the second body to the first, i.e. $\vec{e}_1^I \equiv \vec{r}(t_0)$. By definition S_1 and S_2 have no x and y components in the inertial frame. The set of intrinsic parameters is reduced to[12]

[60]: The LIGO Scientific Collaboration et al. (2021), *GWTC-3: Compact Binary Coalescences Observed by LIGO and Virgo During the Second Part of the Third Observing Run*

11: We consider zero spin binaries as spin-aligned binaries.

12: As mentioned in Section 3.2.3, the dimensionless spins $\vec{\chi}_1$ and $\vec{\chi}_2$ used in waveform models are defined such that $\vec{\chi}_1 = \vec{S}_1/{m_1}^2$ and respectively for $\vec{\chi}_2$.

$\vartheta = \{m_1, m_2, \chi_{1z}, \chi_{2z}\}$. The extrinsic parameters (relative to position and orientation of the binary) are defined with respect to this frame as illustrated in Figure 3.3.

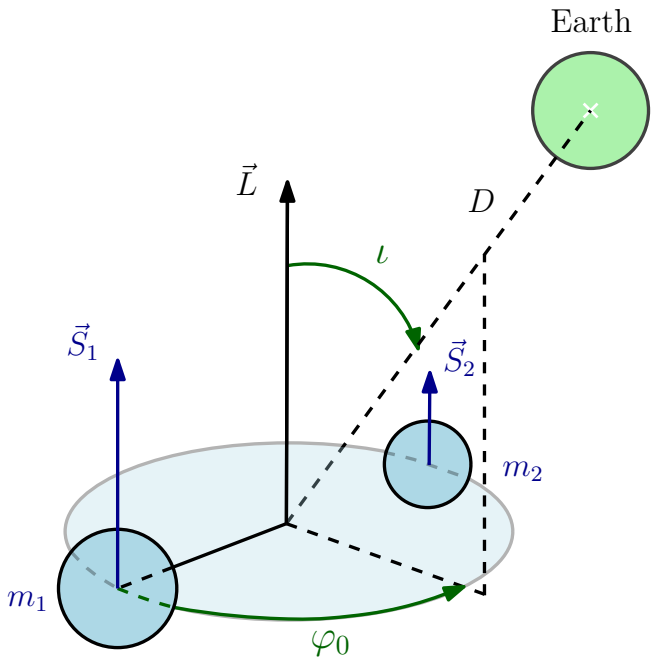

Figure 3.3: Physical parameters of a spin aligned BBH. The spin of each black hole is aligned with the orbital angular momentum $\vec{L}(t)$ which coincides with the normal to the orbital plane. The orbital plane is fixed during the coalescence. The inertial source frame is such that its z axis is aligned with $\vec{L}(t)$ and its x axis is aligned with the (partially dashed) black line going from one object to the other. The source motion is guided by the spins and masses of the objects. The waveform also depends on extrinsic parameters such as the luminosity distance D and the line of sight (ι, φ_0).

In the case of spin-aligned BBHs, the modes of the spin weighted spherical harmonics expansion of $h(t)$ verify the conjugate symmetry

$$h^I_{l,-m}(t) = (-1)^l \overline{h^I_{l,m}(t)}. \tag{3.6}$$

Then it is sufficient to compute modes with positive values of m. Moreover, for low mass ratios the dominant $(2, \pm 2)$ modes give a good approximation of the complete waveform [53]. The proposed model only needs to generate the $(2, 2)$ mode which is a complex-valued amplitude and frequency modulated signal such that $h^I_{l,m}(t) = a(t)e^{\varphi(t)}$ [58].

3.3.1 Generative model

The generation of noise-free waveform surrogates in the case of spin-aligned BBHs has been successfully realized using reduced-order modelling (based on tensor spline fitting) [61, 62] and more standard machine learning approaches such as mixture-of-experts regression [63] and artificial neural networks [64, 65]. We built on [63] and propose a model with reduced complexity based on principal component regression. It improves the overall regression accuracy by about an order of magnitude. These performances are notably achieved thanks to a different choice of features. The

[61]: Pürrer (2016), *Frequency domain reduced order model of aligned-spin effective-one-body waveforms with generic mass-ratios and spins*
[62]: Lackey et al. (2019), *Surrogate model for an aligned-spin effective one body waveform model of binary neutron star inspirals using Gaussian process regression*
[63]: Schmidt et al. (2021), *Machine learning gravitational waves from binary black hole mergers*
[64]: Khan et al. (2021), *Gravitational-wave surrogate models powered by artificial neural networks*
[65]: Chua et al. (2019), *Reduced-Order Modeling with Artificial Neurons for Gravitational-Wave Inference*

full pipeline is implemented using the Scikit-learn software library [66] resulting in a compact code, easy to maintain.

[66]: Pedregosa et al. (2011), *Scikit-learn: Machine Learning in Python*

Outline of the model

The machine learning model we present takes as input a set of astrophysical parameters ϑ and returns a corresponding waveform. The model is based on a judicious representation of the waveform modes.

For non-precessing BBH it suffices to generate the dominant $(2, \pm 2)$ modes in order to have a good approximation of h. Thanks to the conjugate symmetry property (3.6) the computation of the $(2, -2)$ mode is left to post-processing and we consentrate to the generation of the $(2, 2)$ mode can be done from $(2, 2)$ at post processing stage.

The $(2, 2)$ mode is a complex-valued signal $h^I_{2,2}(t) = a(t)e^{i\varphi(t)}$ with a modulated amplitude $a(t)$ and a modulated phase $\varphi(t)$, often referred to as "chirp" for short. Compared to the mode waveform, the two attributes $a(t)$ and $\varphi(t)$ exhibit non-oscillatory and smooth variations with respect to the features, that can thus be accurately fitted.

As presented in Section 2.4.2, the amplitude and phase evolve over different timescales during the dynamical regimes of the chirp signal. To capture their variations with a uniform accuracy over the entire waveform duration, amplitude and phase are discretized in time with a varying sampling resolution. The waveform attributes are resampled on a time grid $\tilde{t}$ going from $t_{\text{start}} = -20\,\text{s}$ to $t_{\text{end}} = 0.006\,\text{s}$ and such that $\tilde{t} = \text{sign}(t)\,|t|^{\frac{1}{\alpha}}$ where $\alpha = 0.35$ [63].

We propose a principal component regressor [67] that consists in a polynomial regression of the (truncated) PCA coefficients of the attributes. The generative model is first learned from a training set of waveforms.

[67]: Hastie et al. (2017), *The elements of statistical learning*

More precisely, the waveform amplitudes (and similarly for phases) are concatenated in a matrix $A \in \mathcal{M}_{N,M}(\mathbb{R})$, where N is the size of the training set and M is the size of the time grid. K principal components of A are computed and stacked in $W_K \in \mathcal{M}_{K,M}(\mathbb{R})$, from which we get the reduced matrix $A_K = AW_K^T \in \mathcal{M}_{N,K}(\mathbb{R})$. A polynomial regressor p_k is used in order to predict the k-th reduced amplitude coefficients. The regressor takes as input a set of features $\tilde{\vartheta}$ that are obtained from the set of binary parameters ϑ by a non-linear mapping. This mapping is optimized in order to improve the

performances. At the generation step, the model regresses the k-th reduced amplitude coefficient as $p_k(\tilde{\vartheta}) = \hat{a}_K[k]$. The truncated PCA is finally inverted such that $\hat{a} = \hat{a}_K W_K \in \mathbb{R}^M$. The same procedure is applied for $\hat{\varphi}$.

The usage of the truncated PCA is motivated by the strong correlation of the waveform attributes for different values of binary parameters. It simplifies the regression task by reducing the dimension of the target space.

The waveform synthesis is performed according to the following steps:

1. The features $\tilde{\vartheta}$ are computed from the requested waveform parameters ϑ.
2. Given $\tilde{\vartheta}$, $a(t)$ and $\varphi(t)$ PCA coefficients are regressed from a polynomial combining of the features.
3. The PCA is inverted to compute the attributes $a(t)$ and $\varphi(t)$, which are mapped to $(2, 2)$ mode waveform.
4. Post processing: based on (3.4), the estimated waveform is computed as follows

$$\hat{h}(t) = \hat{h}^I_{2,2}(t)\,{}_{-2}Y_{2,2}(\iota, \varphi_0) + \hat{h}^I_{2,-2}(t)\,{}_{-2}Y_{2,-2}(\iota, \varphi_0).$$

The various parameters of the generative model (number of PCA, order of the polynomial regression, type of regressor) are optimized in order to minimize the regression accuracy (score) quantified by the mismatch $\varepsilon(\hat{h}, h)$ between the true and estimated waveform defined in Section 3.2.4.

3.3.2 Results

Several models can be used to generate approximate yet accurate waveforms for data analysis purposes [53]. In this work, we use SEOBNRv4 [58], so the generative model predict waveform approximations obtained with this model. It can be adapted to other waveform models by replacing the training set with corresponding waveforms. Our choice is motivated by the comparison it allows with the results of Schmidt [63] and by the model used later in Section 3.4, which is also a model generalizing SEOBNRv4 in the case of precessing binaries.

The code needed to reproduce the presented results is public: https://git.ligo.org/cyril.cano/gw-generation. It takes the form of a python package from which one can compute and evaluate a waveform generative model. A precomputed

model is given, it allows an external user to generate gravitational waveforms without having to compute the training set.

Training and testing datasets

A dataset of 4000 randomly distributed BBH waveforms was computed with `LALSimulation` software library [52]. The construction of the dataset was performed using the GRICAD infrastructure[13], which is supported by Grenoble research communities, while the learning part is done on a personal laptop. The mass ratio q is uniformly sampled over $[1, 20]$ and the dimensionless spins χ_{1z}, χ_{2z} are uniformly drawn in $[-0.8, 0.95]$.

13: GRICAD is a Scientific Computing and Data Infrastructure supported by CNRS, Grenoble Alpes University, Grenoble Institute of Engineering and INRIA. See https://gricad.univ-grenoble-alpes.fr.

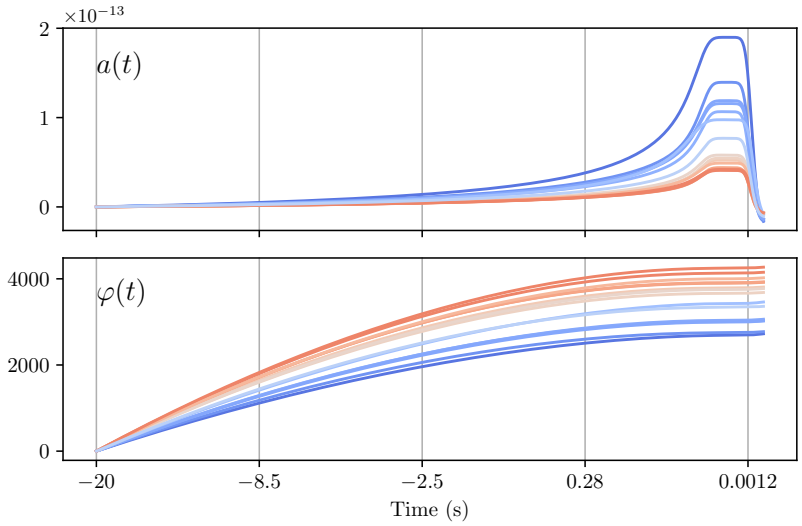

Figure 3.4: Sample of size 20 of the attributes in the dataset. The time grid is sampled in a non-uniform way, with more sample near the merger than during the inspiral. The color is indexed on the mass ratio value. Red corresponds to $q \sim 20$ and blue to $q \sim 1$.

The attributes are stacked in two matrices, used for the computation of the principal components. Each waveform attribute is aligned to zero at $t = t_{\text{start}}$ for PCA efficiency purposes[14].

14: The amplitude and phase offsets subtracted by the alignment procedure can be fitted and added back at the generation stage to produce the full waveform. Though we don't detail this part here but this can be done with good accuracy with the same regressor.

The dataset is made to be comparable with the one used by Schmidt et al. [63]. It is splitted into a training and a testing set that corresponds to 80% and 20% respectively. All reported results are obtained with the testing set.

Figure 3.4 shows a selection of examples from the training set. The attributes appear to have a regular dependency with respect to the feature q.

Number of principal components

There are two origins for the modelling errors for each attribute: the PCA truncation error and the regression error.

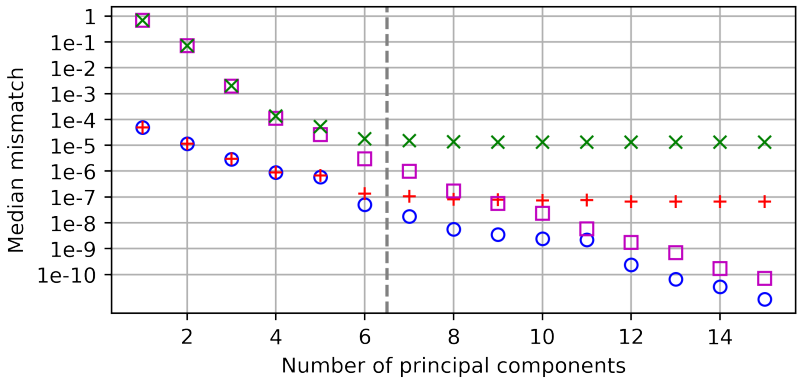

Figure 3.5: Median mismatch *vs* number of principal components retained after PCA truncation. The mismatch is computed after fitting the amplitude only (phase is exact) for blue circles and red plus signs, and the phase only for violet boxes and green crosses. Circles and boxes represent mismatches solely due to the PCA truncation and plus signs and crosses represent mismatches due to the overall model (including the regression step). The dashed line indicates the selected PC truncation level at 6 PC.

Figure 3.5 presents the modelling error imputed to PCA truncation (circles and boxes) as well as the total error including regression (plus signs and crosses) when fitting the amplitude (phase is exact) in blue and red, or the phase (amplitude is exact) in violet and green.

The phase approximation errors lead the overall score. For example, the truncation to only one PC (principal component) leads to a mismatch of 5×10^{-5} for the amplitude and 0.7 for the phase. The accuracy of phase regression is thus critical for the final overall accuracy.

The overall error after regression stabilizes at 6 PCs for the phase (green crosses) with a mismatch median score of about 10^{-5}. This is the retained number of PCs after truncation as this indicates the regressor fails to estimate higher order PC coefficients. For simplicity, the PCA expansion is truncated to the same number of PCs for both the amplitude and phase.

Feature selection

The choice of the feature set has a significant impact on the final score and regression accuracy. Schmidt et al. [63] use a mixture of experts regressor to infer the PCA coefficients from the set of intrinsic parameters $\vartheta = \{m_1, m_2, \chi_{1z}, \chi_{2z}\}$. This ensemble learning method is based on a weighted sum of linear regressors called "experts" [67]. A range of experiments was made, we tested several regressor (e.g. multilayer perceptron, random forest regressor) and preferred to work with a simpler regressor applied to a different feature set $\tilde{\vartheta}$.

To leading order, the amplitude and phase evolution are known [53] to depend on the chirp mass $\mathcal{M}$, the mass ratio q

and the effective spin $\chi_{\text{eff}} = (q\chi_{1z} + \chi_{2z})/(1+q)$. Naturally those physically motivated parameters are good candidates to fit the data.

Systematic tests of different feature combinations were performed. Promising feature sets were pre-selected based on their r^2 score [66] obtained for the prediction of the first PCs of the phase as it essentially determine the overall performance. The tested feature sets have up to 6 parameters. They include parameters such as the masses m_1, m_2, their inverses $1/m_1$, $1/m_2$, the effective spin χ_{eff}, the mass ratio q and the chirp mass $\mathcal{M}$.

Twenty feature sets were found to give the best median mismatch of order 10^{-5}. Among them, $\{\chi_{1z}, \chi_{2z}, q, m_2\}$ and $\{\chi_{2z}, \chi_{\text{eff}}, \mathcal{M}\}$ are of particular interest. The latter have the nice property to have only three features, as the number of intrinsic parameters, however the former results in a much smaller variance for the mismatch (which implies that the 95% percentile of the observed distribution is much more lower) and is thus preferred.

Interestingly physically motivated feature sets such as $\{q, \chi_{1z}, \chi_{2z}\}$ or $\{q, \chi_{\text{eff}}, \mathcal{M}\}$ do not perform as well, with a median mismatch of 0.03 and 0.1 respectively.

Order of polynomial features

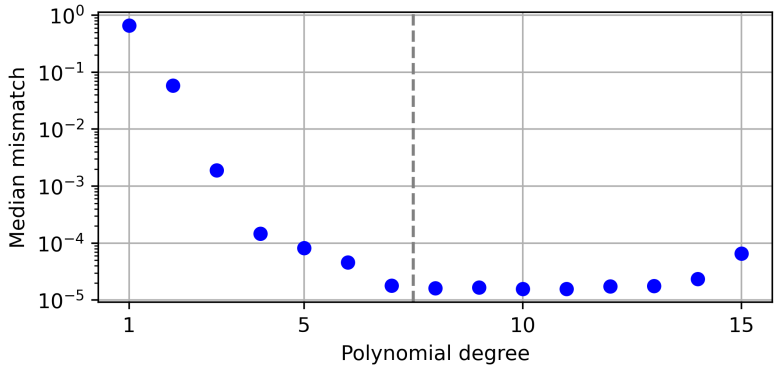

Figure 3.6: Median mismatch *vs* order of the polynomial expansion of features $\{\chi_{1z}, \chi_{2z}, q, m_2\}$. The dashed line shows the selected degree of 7.

To capture the non-linear part of the signal, the regression model is applied to the polynomial expansion of the features $\tilde{\vartheta} = \{\chi_{1z}, \chi_{2z}, q, m_2\}$ up to a pre-determined order. This maximum order is chosen to optimize the score. Figure 3.6 shows the results for polynomial orders from 1 to 15. As the polynomial order increases, the performance improves. After the 13^{th} order, it faces an overfitting problem. The 7^{th} order is

selected[15]: it is found to be the smallest order that minimizes the median mismatch.

15: Classically polynomial regression methods use lower order so the results are interpretable. Here we prefered to focus on the performances of the model rather than insuring its interpretability.

Accuracy and runtime benchmarking

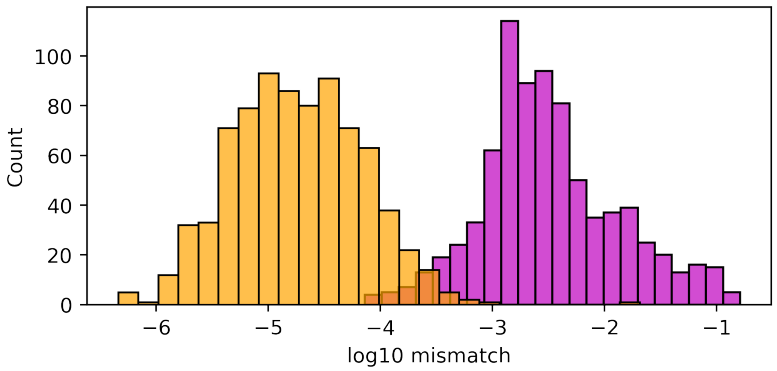

Figure 3.7: Histogram of mismatches on the test set for the proposed model (orange) and Schmidt's model (violet). Even if the dataset we used is supposed to be comparable to the dataset used in [63], we were not able to exactly reproduce the presented results.

The objective was to build a generative model with mismatch scores $\varepsilon \leqslant 10^{-5}$. It is achieved by the proposed model on almost all the parameter space. Figure 3.7 shows the mismatch distribution over the testing set using the feature $\tilde{\vartheta} = \{\chi_{1z}, \chi_{2z}, q, m_2\}$. The median mismatch is 1.8×10^{-5} (average is 6.8×10^{-5}) and the 5% and 95% percentiles are $2.2{\times}10^{-6}$ and $1.6{\times}10^{-4}$ respectively. The worst case mismatch is $\sim 10^{-2}$.

Figure 3.8 presents the example of two predicted waveforms. The first example is representative of the median prediction accuracy for which the prediction error can not be seen by eyes. The second example is the worst prediction made in the testing set. For this one, phase prediction error is clearly visible.

We implemented the model presented in [63] in order to compare it. As shown on Figure 3.7 we were not able to reproduce the presented results. No matter which reference is considered ([63] or our reproduction), we show an improvement of at least one order of magnitude compare to Schmidt et al. model.

The distribution of errors is not uniform in the parameter space. Figure 3.9 shows that the best fits are for high mass ratios. The model struggles to obtain the same accuracy level at low mass ratios and for high effective spins, where there is a more important diversity in the waveform attributes.

Schmidt et al. [63] achieve a median mismatch value of 5×10^{-4} for the spin aligned case, with tails going to 10^{-1} in

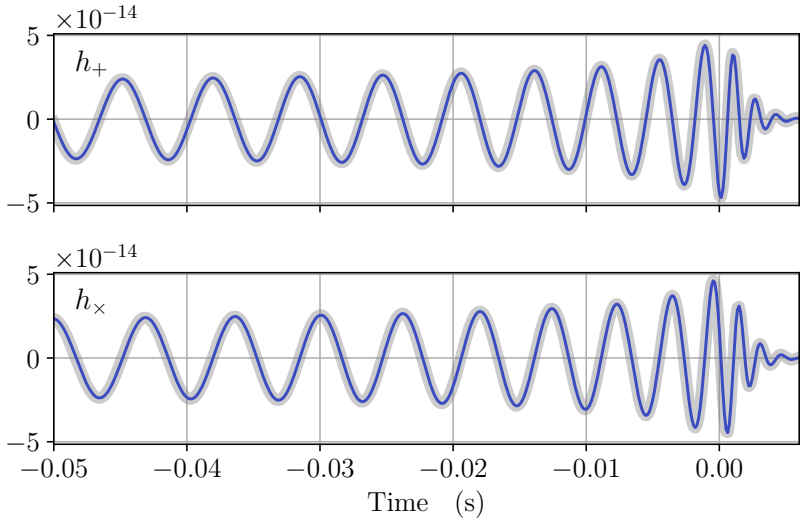

(a)

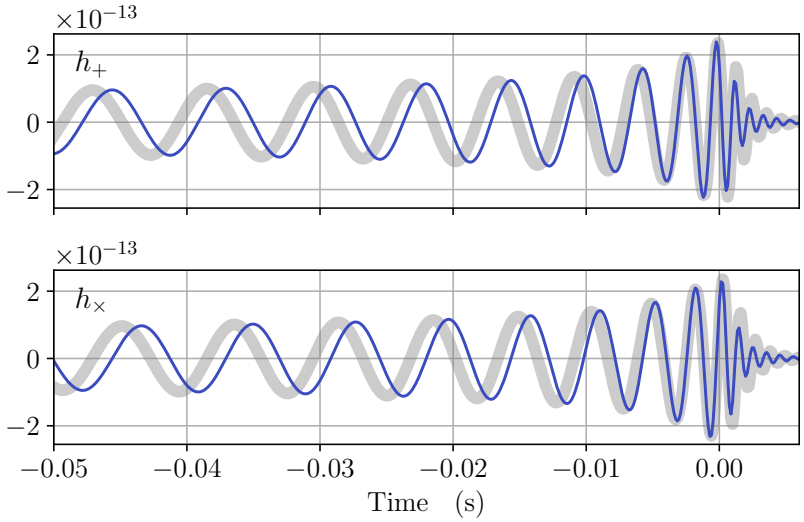

(b)

Figure 3.8: Zoom on target waveforms (grey) generated by SEOBNRv4 and predictions (blue) from the proposed model. **(a)**: waveform for which the mismatch is 10^{-5} (median mismatch on the testing set). **(b)**: waveform for which the mismatch is 10^{-2} (worst mismatch on the testing set).

the worst case. This corresponds to an applicability range that goes up to SNR = 54 (3 in the worst case). Our model has generation errors uniformly much smaller than the intrinsic numerical and modeling errors of SEOBNRv4 (which is less than 1% [58]). Thus it produces approximations of SEOBNRv4 waveforms without adding substantial errors.

We compared the generation time of SEOBNRv4 model with the proposed machine learning model. Figure 3.10 presents a distribution of the speed-up factor defined as the ratio between the generation time of SEOBNRv4 (using `LALSimulation` [52]) and the proposed principal component regression model. A set of 500 BBH waveforms was generated for a uniform distribution of total mass between 40 $M_\odot$ and 100 $M_\odot$. The other parameters are distributed as for the mismatch evaluation. The observed median speed-up is $\sim 10^2$ (comparable to [63]). It illustrates the benefits of using

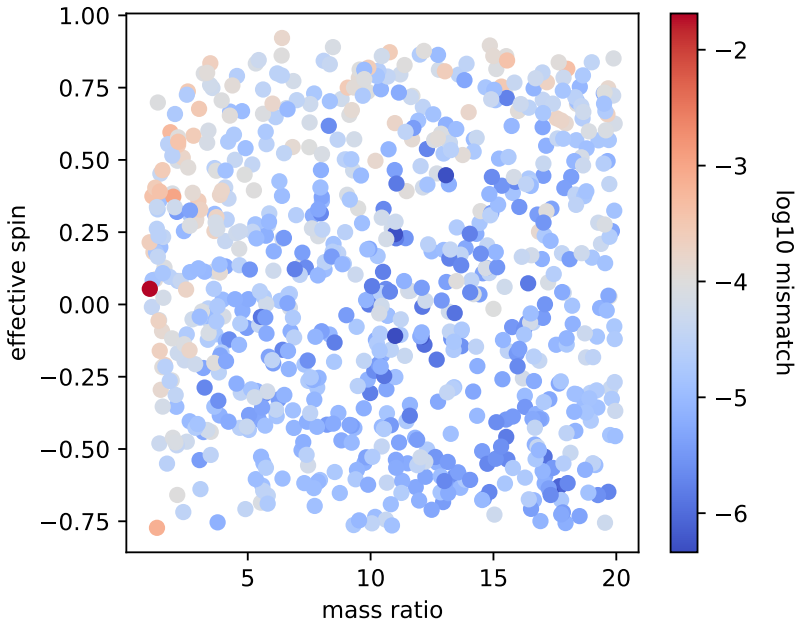

Figure 3.9: Scatter plot of the mismatches with respect to the mass ratio and the effective spin. Each point corresponds to a compact binary in the test set.

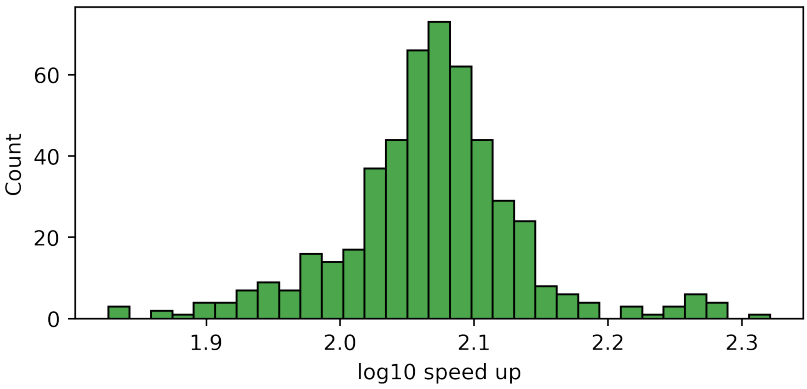

Figure 3.10: Speed up factor of the proposed model compared to SEOBNRv4 for a population of spin-aligned BBHs with total masses going from 40 $M_\odot$ to 100 $M_\odot$.

the proposed model to accelerate parameter estimation with Bayesian samplers [45].

Usage with Bilby

Bilby [45] is a user-friendly parameter estimation code made for gravitational-wave astronomy. Bilby allows a user-defined prior and likelihood function to be passed to a sampler, and collects the posterior samples and the evidence calculated by the sampler. It provides an easy access to the gravitational-wave data [68] as well as to a range of priors and likelihood functions that are often encountered in the context of gravitational-wave astronomy.

In collaboration with Tom Colin, we used the principal component regression model with Bilby [69]. The model was used for the estimation of posterior distribution for the event GW150914. As illustrated in Figure 3.11, the results show consistent posterior estimation with respect to physical

[68]: Abbott et al. (2021), *Open data from the first and second observing runs of Advanced LIGO and Advanced Virgo*

[69]: Ashton et al. (2019), *Bilby: A User-friendly Bayesian Inference Library for Gravitational-wave Astronomy*

waveform models as SEOBNRv4. On a modern laptop, the computation took 3 h 13 min and 21 min for the proposed generative model and SEOBNRV4 respectively, that is an acceleration factor of about 10.

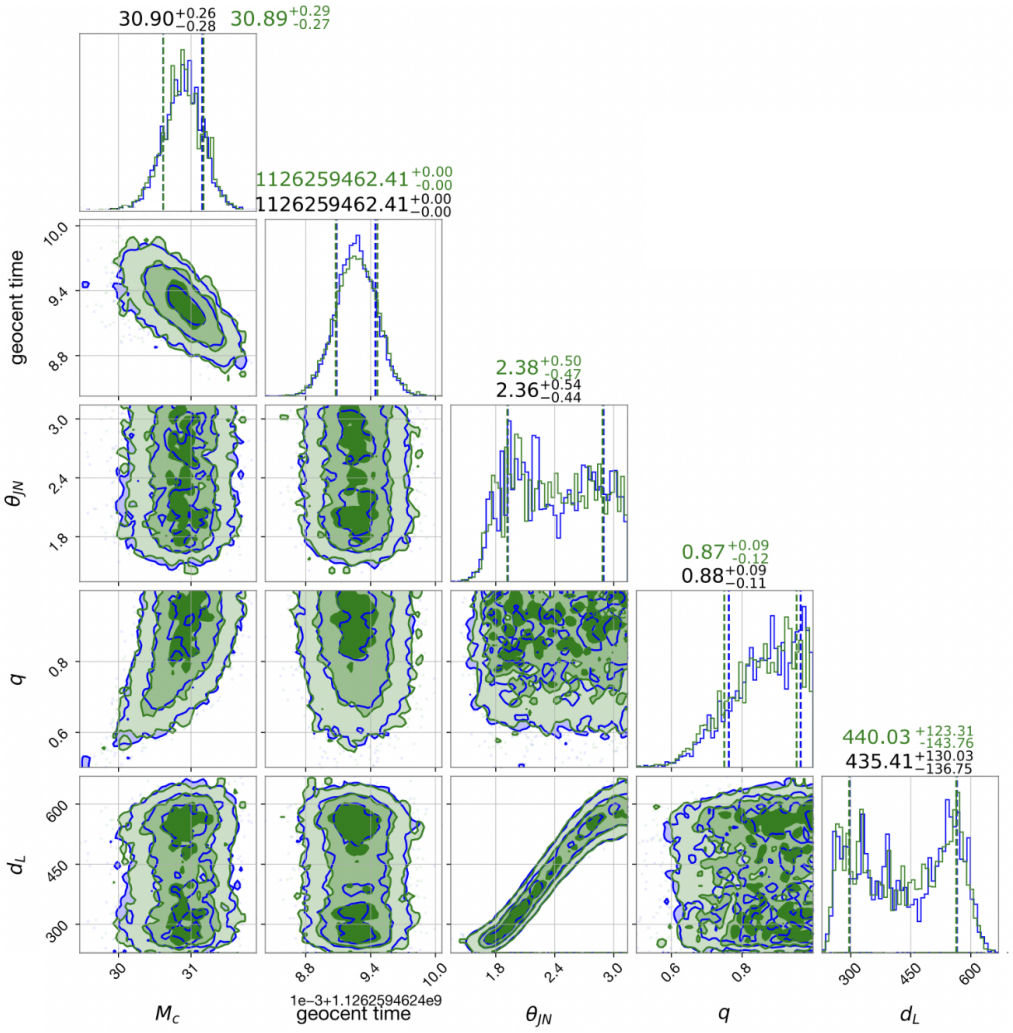

Figure 3.11: Corner plot showing the comparison of the posterior distribution obtained for the event GW150914 with Bilby using the SEOBNRv4 (frequency domain approximant) in blue and the fast approximant model proposed here in green. The posterior densities are shown for the following parameters: the detected chirp mass M_c , the mass ratio q, the merger time t_c in the geocentric frame, the inclination angle θ_{JN} and the luminosity distance d_L.

3.4 Precessing binary black holes

In a generic configuration, BBHs have spin angular momentums $\vec{S}_1(t)$ and $\vec{S}_2(t)$ not aligned (nor anti-aligned) with the Newtonian angular momentum $\vec{L}_N(t)$ i.e. the normal to the orbital plane. In this case, as illustrated in Figure 3.12, the spins and the Newtonian angular momentum precesses around the total angular momentum $\vec{J}(t)$.

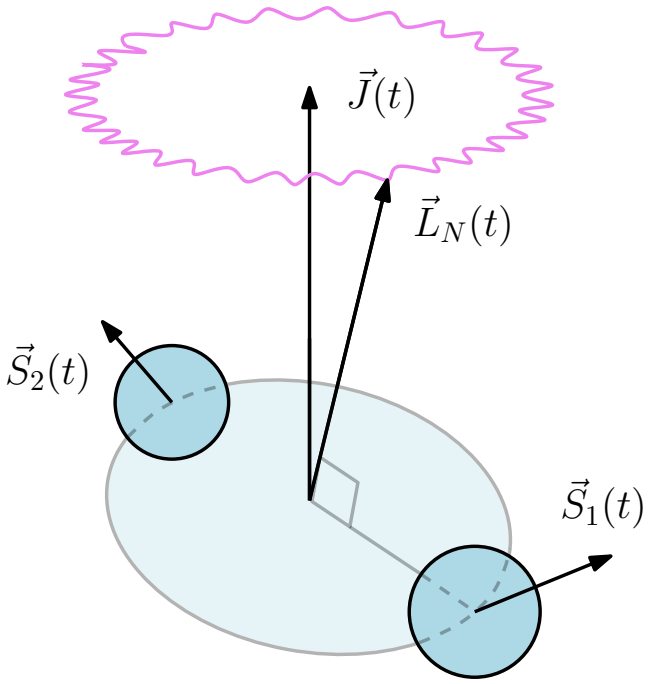

Figure 3.12: Precession of the orbital plane induced by the misalignment of the spin of at least one of the two bodies with the Newtonian angular momentum $\vec{L}_N(t)$. In constrat to the EOB orbital angular momentum $\vec{L}(t)$, $\vec{L}_N(t)$ has a slight nutation. Variations of the orientation of the orbital plane affect the polarization of the waveform modes.

An inertial frame I can be defined at a given time t_0 such that $\vec{e}_3^I \equiv \vec{L}_N(t_0)$ and $\vec{e}_1^I \equiv \vec{r}(t_0)$ (where $\vec{r}(t)$ points from the second body to the first). The inclination ι and the initial phase φ_0 are defined with respect to the basis $(\vec{e}_1^I, \vec{e}_2^I, \vec{e}_3^I)$, where $\vec{e}_2^I = \vec{e}_3^I \times \vec{e}_1^I$. The spin components are defined in this basis, leading to the set of intrinsic parameters $\vartheta = \{m_1, m_2, \chi_{1x}, \chi_{1y}, \chi_{1z}, \chi_{2x}, \chi_{2y}, \chi_{2z}\}$.

The waveform modes of the spin weighted spherical expansion (3.4) are defined with respect to the inertial frame I. As opposed to spin-aligned binaries, the effect of the subdominant modes is enhanced by precession and the restriction to the dominant $(2, \pm 2)$ modes leads to a significant error. Also the conjugate symmetry property (3.6) no longer holds. Each inertial mode should be computed separately by its own generative model.

Referring to Chapter 4, the polarization state of the waveform modes is determined by the orientation of the orbital plane with respect to the observer and the precession motion

modulates their polarization state over time. In Chapter 1, we studied a number of representation for AM-FM-PM signals. We tested and applied these representations to the modes that dominantes the expansion of a gravitational waveform of a precessing BBH. Based on this, in this section, we investigate various options to construct a machine learning generative model for time-domain gravitational waveforms from precessing BBH thanks to the Euler angle parametrization presented in Chapter 1.

3.4.1 Rotation of the inertial frame

As what will be shown in Chapter 4, orbital precession modulates the polarization of waveform inertial modes. Figure 3.13 displays the $(2,1)$ modes of two simulated gravitational waveforms, both from a non-precessing and a precessing BBH.

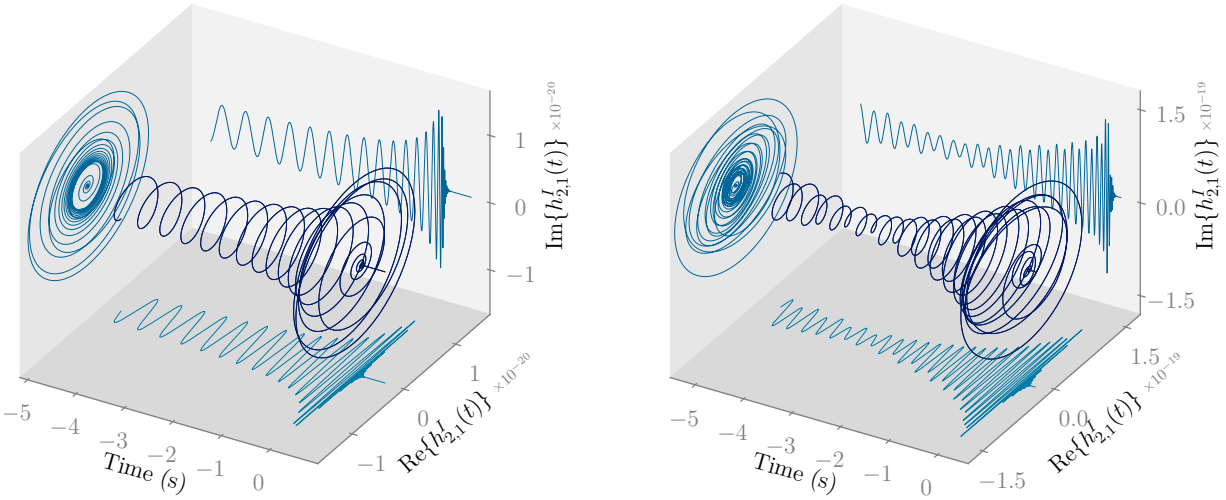

Figure 3.13: Inertial modes $h^I_{2,1}(t)$ simulated with SEOBNRv4P for a spin-aligned **(a)** and a precessing **(b)** BBH. The inertial mode associated with the spin-aligned binary is an amplitude and frequency modulated signal (it is circularly polarized) while the same mode for a highly precessing binary is modulated in polarization (it evolves in a time varying ellipse). The non-precessing binaries is such that $m_1 = 15$, $m_2 = 5$ with spins $\chi_{1z} = 0.9$, $\chi_{2z} = 0.9$. The precessing one has spins $\chi_{1x} = 0.1$, $\chi_{1y} = 0.6$, $\chi_{1z} = 0.2$, $\chi_{2x} = 0.4$, $\chi_{2y} = 0$, $\chi_{2z} = 0.5$, which correponds to $\chi_p = 0.6$ (highly precessing binary).

The Euler angle parametrization presented in Chapter 1 decomposes such signal in a quadruplet $[a(t),\ \theta(t),\ \chi(t),\ \varphi(t)]$ as a generalization of AM-FM signal decomposition used in Section 3.3. It was shown that this parametrization is subject to an indeterminacy problem for circular and nearly circular instantaneous polarization states.

Inertial modes are circularly polarized when $\vec{L}_N(t)$ is aligned with $\vec{e}_3^I$ (which is by convention parallel to $\vec{L}_N(t_0)$). The general dynamics of the system is such that periodically $\vec{L}_N(t)$ reaches same positions (see Figure 3.12), where the waveform modes are circular. This causes the Euler angle indeterminacy to occur periodically.

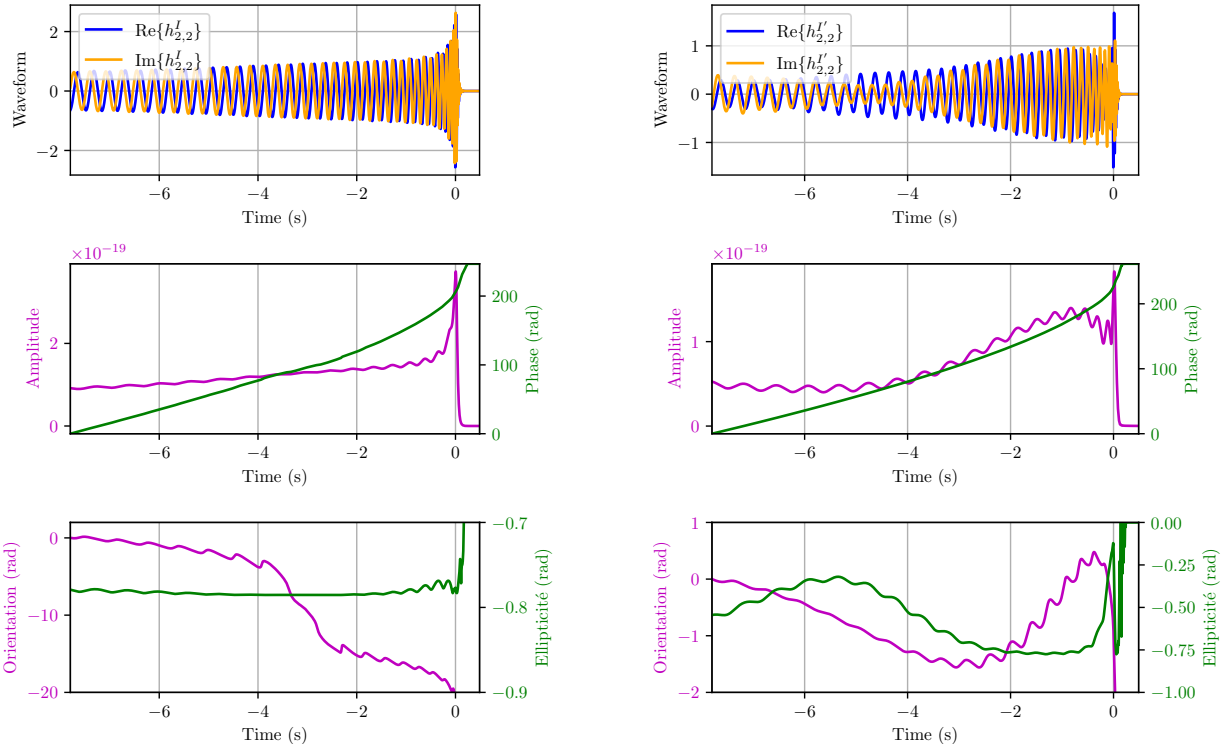

Figure 3.14: $(2,2)$ inertial mode in the I frame **(a)** and the I' frame **(b)** for a precessing BBH. In the I frame, the gimbal lock induces spurious variations of the instantaneous ellipticity and phase when the signal is quasi-circular (see the phase and orientation curves in **(a)** aroud $t = -3$ s). The estimated instantaneous orientation in **(a)** shows variations about 20 rad during the last 8 sec of the coalescence, while in **(b)** it remains between $\pm\pi/2$ rad. The problem is solved in the rotated frame I' in which the mode is kept elliptic all the time. The binary is such that $m_1 = 15\,M_\odot$, $m_2 = 5\,M_\odot$ with spins $\chi_{1x} = 0.1$, $\chi_{1y} = 0.6$, $\chi_{1z} = 0.2$, $\chi_{2x} = 0.4$, $\chi_{2y} = 0$, $\chi_{2z} = 0.5$, which correponds to $\chi_p = 0.6$ (highly precessing binary).

In order to avoid such indeterminate configurations, we switch to a different inertial frame I' for the spin weighted spherical harmonic expansion of the gravitational waveform. By convention this frame is fixed such that its z axis is inclined by $\pi/3$ rad compared to e_3^I. The rationale is that the waveform expressed in this new inclined frame is less likely to be purely circular and therefore become locally degenerate for the Euler angle representation. The rotation of the modes from I to the new inertial frame I' is achieved with the Wigner D-matrices, such as

$$h^{I'}_{l,m}(t) = \sum_{m'=-l}^{l} h^{I}_{l,m'}(t) D^{l}_{m',m}(0, \pi/3, 0), \qquad (3.7)$$

where $D^{l}_{m',m}$ are the Wigner D-matrices described in Appendix B. The waveform is thus decomposed in the new inertial frame I' as[16]

$$h(t) = \frac{M}{D} \sum_{l=2}^{\infty} \sum_{m=-l}^{l} h^{I'}_{l,m}(t) {}_{-2}Y_{l,m}(\iota', \varphi_0'). \tag{3.8}$$

16: Note that the choice of the inertial frame in which the waveform is expanded is a free parameter. The choice of a given source frame is important in the definition of the spin weighted spherical harmonics ${}_{-2}Y_{l,m}$, with respect to which the waveform modes are computed.

This solution is not valid for highly precessing BBHs for which the orbital plane can even flip, resulting in a temporary quasi-alignment (or anti-alignment) of $\vec{e}_3^{\,I'}$ and $\vec{L}_N(t)$. Figure 3.14 demonstrates the effect of the rotation of the inertial frame on the $(2,2)$ mode of a precessing BBH. In particular we show that the instantaneous parameters of the I' modes are not subject to the same indetermination.

3.4.2 Generative model

The generation of gravitational waveforms from precessing BBHs is a difficult problem due to the diversity of the waveforms. Also the generative model has to fit the polarization modulation induced by the orbital precession. The purely circularly polarized model used in the previous section does not work.

It has been recently achieved with an artificial neural network [70] (achieving a median mismatch of $\sim 10^{-4}$). Thomas' model [70] computes the waveform in a co-precessing frame and rotates it to correspond to an inertial frame. In the co-precessing frame the modes are not modulated in polarization, such that the generation procedure consists (roughly) to generate spin-aligned modes and rotation parameters. We propose a different approach based on a specific representation of waveform inertial modes as amplitude, frequency and polarization modulated signals. While facing technical limitations, we show promising results.

[70]: Thomas et al. (2022), *Accelerating multimodal gravitational waveforms from precessing compact binaries with artificial neural networks*

Outline of the model

The proposed model has the same global structure as for spin-aligned BBHs. It generates the inertial waveform modes $\{(2,\pm2), (2,\pm1), (2,0)\}$ in the rotated frame I' thanks to a decomposition in adapted waveform attributes. The $(2,\pm2)$ and $(1,\pm1)$ modes are decomposed in four attributes: the instantaneous amplitude $a(t)$, instantaneous orientation $\theta(t)$, instantaneous ellipticity $\chi(t)$ and instantaneous phase $\varphi(t)$.

The real and imaginary parts of the $(2,0)$ mode are treated separately and decomposed in instantaneous amplitude and instantaneous phase[17].

17: The real part and the imaginary part of the $(2,0)$ mode computed with SEOBNRv4P have quite different instantaneous frequencies, such that $h^{l'}_{2,0}(t)$ cannot be considered as an AM-FM-PM signal as defined in Chapter 1.

The mode attributes are computed with the procedure presented in Appendix A.3. The waveform is zero padded and windowed before applying the discrete quaternion Hilbert transform in order to avoid instrumental gimbal lock as well as aliasing. The instantaneous parameters of the $(2,\pm2)$ and $(2,\pm1)$ modes are deduced from their quaternion embeddings. The amplitude and phase of the real and imaginary parts of the $(2,0)$ mode are deduced from the associated analytic signal constructed with the complex Hilbert transform.

For each mode attribute the model performs a principal component regression [67]. The PCA coefficients of the attribute are predicted thanks to a polynomial regression from a set of features ϑ.

The model has to account for new effects with respect to spin-aligned BBH. The nutation of the orbital plane has an effect on mode attributes, adding an oscillatory behaviour as shown in Figure 3.14. This prevents from using the non-uniform time grid resolution as in the spin-aligned case, which in turn will limit the model's ability to generate long duration waveforms.

The model synthesis phase can be decomposed in the following steps:

1. A set of features $\tilde{\vartheta}$ is computed based on the user input binary parameters

$$\vartheta = \left\{m_1,\, m_2,\, \chi_{1x},\, \chi_{1y},\, \chi_{1z},\, \chi_{2x},\, \chi_{2y},\, \chi_{2z}\right\}.$$

2. The reduced coefficients of each mode attribute are regressed by a polynomial regressor.
3. The PCAs are inverted to compute mode attributes.
4. Finally, the gravitational waveform is constructed from (3.8).

3.4.3 Results

In principle, the proposed machine learning model can be adapted to every time-domain waveform models. In this work we used SEOBNRv4P [51] which is an EOB model for precessing BBHs[18]. EOB models outperform Phenomenological models in terms of waveform accuracy but their

18: The formalism of SEOBNRv4P, discussed in Section 3.2, is based on a definition of a coprecessing frame P (see Chapter 4). In this frame we considered both the $(2,\pm2)$ and $(2,\pm1)$ modes.

computation time is more important. Building a fast and accurate generative machine learning model is a way to get fast approximation of SEOBNRv4P waveforms without losing performances in the inference process.

Training and testing datasets

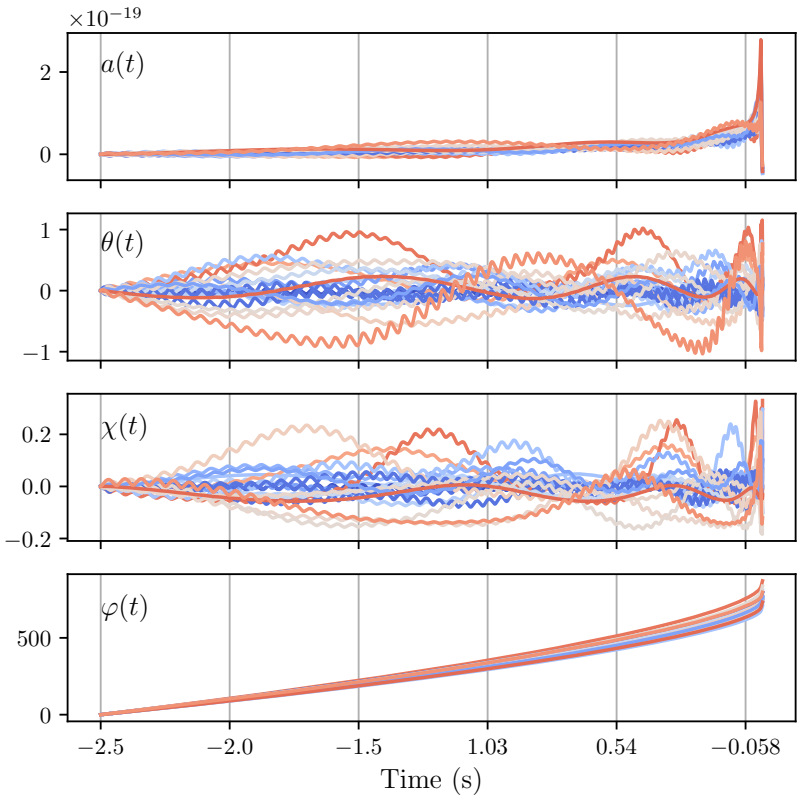

Figure 3.15: Sample size 20 of the dataset corresponding to $(2, 2)$ mode. The color scale is indexed on the value of χ_p which correspond to the level of precession. Low values ~ 0 are represented in blue and high values ~ 0.5 are represented in red.

We computed a dataset consisting in 1000 different configurations[19], composed of $(2, \pm 2)$, $(2, \pm 1)$ and $(2, 0)$ inertial modes in the rotated inertial frame I'. The computation was performed on GRICAD clusters[20]. The mass ratio is uniformly sampled in $[1, 4]$ and the norm of the spins is uniformly sampled in $[0, 0.95]$. The orientation of the spin is sampled from an isotropic distribution on the north hemisphere of the I frame. We further applied a selection threshold on the value of the dimensionless effective precession spin $\chi_p = S_p/(A_1 {m_1}^2)$ which governs the precession dynamics at the first order [71], where $S_p = \max\left(A_1 {m_1}^2 \|\chi_{1\perp}\|, A_2 {m_2}^2 \|\chi_{2\perp}\|\right)$ is the effective precession spin[21] and $A_1 = 2+3q/2$, $A_2 = 2+3/(2q)$. Values of χ_p higher than 0.5 are discarded in order to limit the precession and avoid indeterminate cases while computing the attributes of the modes (i.e. cases where $\chi(t) \sim \pi/4$), which correspond to configurations when the z axis of the rotated frame I' is

19: This is four times less than the previous study.

20: GRICAD is a Scientific Computing and Data Infrastructure supported by CNRS, Grenoble Alpes University, Grenoble Institute of Engineering and INRIA. See https://gricad.univ-grenoble-alpes.fr.

[71]: Schmidt et al. (2015), *Towards models of gravitational waveforms from generic binaries: II. Modelling precession effects with a single effective precession parameter*

21: We denote $\|\chi_{1\perp}\| = \sqrt{{\chi_{1x}}^2 + {\chi_{1y}}^2}$ and respectively for $|\chi_{2\perp}|$.

nearly aligned with the Newtonian orbital angular momentum $\vec{L}_N(t)$, and is likely to happen for strongly precessing binaries.

To keep the data volume manageable despite the high sampling frequency needed to capture the nutation oscillations[22], we limit the time grid between $t_{\text{start}} = -2.5\,\text{s}$ and $t_{\text{end}} = 0.006\,\text{s}$. The time origin of the waveform attributes is set to $t = t_{\text{start}}$.

A sample of the dataset is shown in Figure 3.15. Compared to the previous case with spin alignment, there is a larger diversity of waveforms which makes the generation a much more complicated problem.

The training and testing sets correspond to 80% and 20% of the dataset respectively. All reported results are obtained with the testing set.

22: We used SEOBNRv4P waveforms sampled at 8kHz, that allows a sufficient level of oversampling and smoothness of the waveform attributes.

Number of principal components

PCA truncation is the first source of error. The number of selected principal components is determined by the objective on the waveform accuracy and the regressor performances on each reduced coefficients.

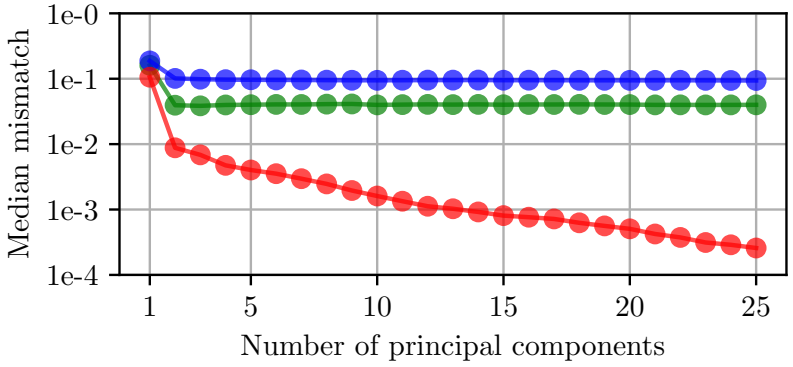

Figure 3.16: Median mismatch *vs* number of principal components. The green points are obtained by including only the $(2, \pm 2)$ modes for the waveform approximation. The $(2, \pm 1)$ modes are added to the $(2, \pm 2)$ modes for the blue points and the red points are obtained with all the inertial modes.

The mismatch is given for a zero inclination in the rotated inertial frame I', which is equivalent to say that $\iota = \pi/3$ in the inertial frame I. It allows to sanction subdominant mode prediction errors[23].

Figure 3.16 presents the median mismatch depending on the number of principal components that is kept. The PCA truncation error goes below 10^{-3} for a minimum of 14 principal components. Figure 3.16 also illustrates the importance of including subdominant modes in the waveform predictions.

23: The expression of the different modes is ponderated by the spin weighted spherical harmonics, which depends on the inclination of the source ι.

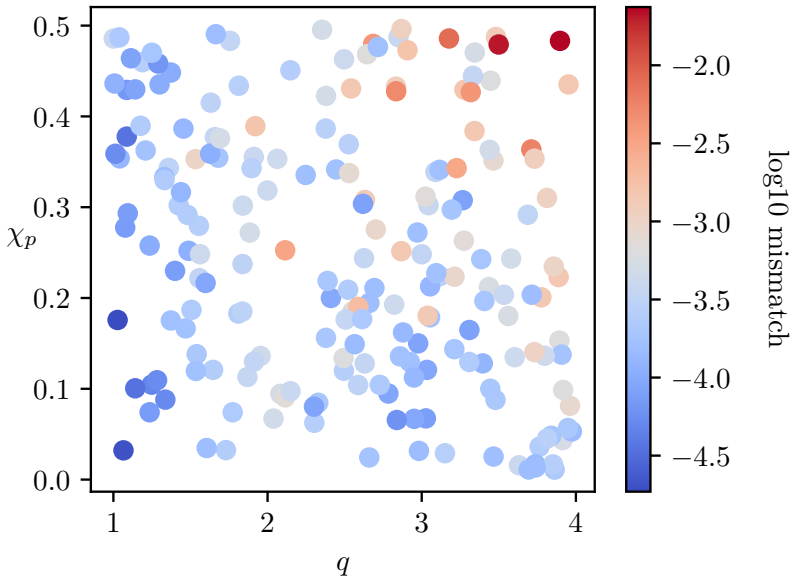

Figure 3.17: Scatterplot of mismatches attributable to PCA truncation at 25 principal components according to the mass ratio and the dimensionless effective precession spin.

The mismatch is much smaller when including all the inertial modes.

The PCA approximation error of the modes' attributes is not constant over the parameter space. As illustrated in Figure 3.17, the waveform mismatch induced by PCA truncation is higher for high mass ratio and high dimensionless effective precession spin, that is for highly precessing binaries.

Regression of reduced PC coefficients

As a generalization of the spin-aligned generative model, the regression is performed by a polynomial regressor over a set of features ϑ. The set of features and the order of the polynomial regression should be optimized through cross validation.

We could not find a feature set nor a polynomial order able to reach a mismatch of 10^{-4} uniformly over the full parameter space. Note that the learning process is limited by the small size of the training set[24] ~ 800.

24: The training set is smaller than the one used for spin-aligned binaries even though the regression problem is more complex.

As in the spin-aligned case (see Figure 3.5), the phase reduced coefficients regression accuracy is found to lead the overall prediction error. These leading coefficients have rather poor regression accuracy with a polynomial regressor. For instance, given the set of features

$$\vartheta = \{q, \chi_p, m_1, m_2, \chi_{1x}, \chi_{1y}, \chi_{1z}, \chi_{2x}, \chi_{2y}, \chi_{2z}\}$$

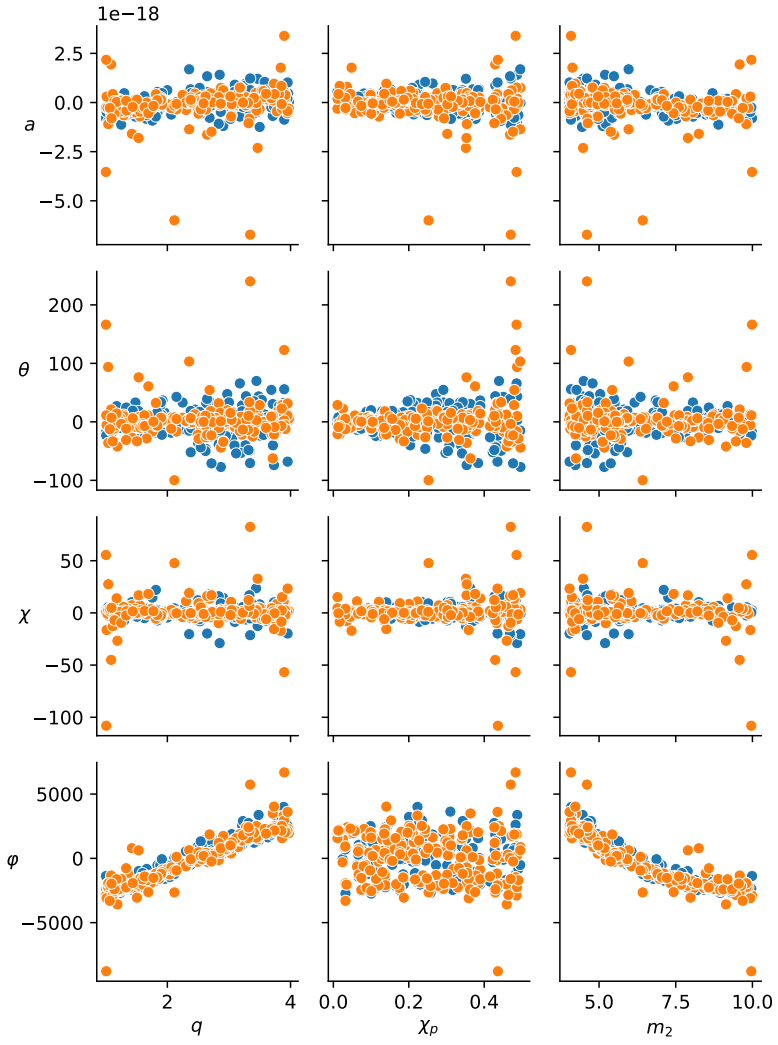

Figure 3.18: Scatterplot of the features *vs* first reduced coefficients of the attributes of the (2, 2) mode. True reduced coefficients are in blue and predicted ones are in orange.

and a polynomial order of 7, the r^2 score regarding the first reduced coefficients of the phase for the different modes is of the order of 10^{-2} while it was $\sim 10^{-9}$ in the spin aligned case. It is of the order of 10^{-1} for the second reduced coefficients of the phase of the different modes, while it was $\sim 10^{-7}$ in the spin aligned case. Figure 3.18 shows the first reduced attribute coefficients of the dominant (2, 2) mode. The regressor clearly succeeds to fit the general trend but fails to fit the details at the required 10^{-4} precision level.

Figure 3.19 compares a waveform predicted by the proposed model with the corresponding SEOBNRv4PHM waveform. It is clear that the results are not as good as in the spin-aligned case. An additional difficulty we found here was highlighted by the gap between the red curve of Figure 3.16 and the others. This time, the evaluated waveform is a sum of oscillatory signals and thus a slight mislanignment between the phase of the predicted modes can drastically change the result.

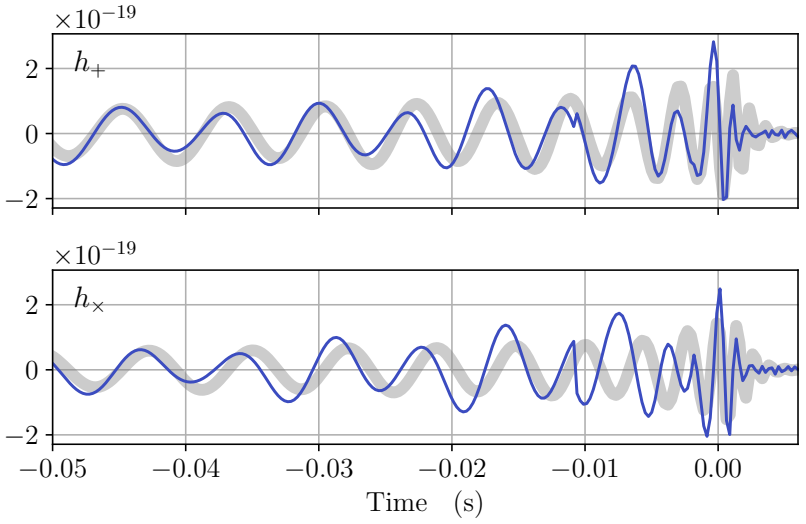

Figure 3.19: Zoom on a target $(2, 2)$ waveform mode (grey) generated by SEOBNRv4PHM (in the rotated inertial frame I') and a prediction (blue) from the proposed model. The mismatches of the total waveform and of the rotated $(2, 2)$ mode are ~ 0.6.

Discussion and perspectives

The presented approach shows promising results for waveform generation in the case of precessing BBHs. As illustrated in Figure 3.18 (e.g. see the last line), the distribution of the reduced coefficients of the different attributes have a clear dependence on some features. These results call for an extention of the size of the dataset in order to test the limits of the model[25]. The regression task should be tackled by a more complex regressor able to fit the non linearity of the data, e.g. a neural network.

25: Hardware limitation is the main constraint on the size of the dataset. One should completely run the proposed model on a computing cluster.

Interestingly, the reduced coefficients of the mode attribute are very similar i.e. the first reduced coefficients of the phase for the $(2, \pm 2)$, $(2, \pm 1)$ and $(2, 0)$ modes are very close to each other. This suggests that, just like what we propose, the same regressor can be used for all the modes' attributes.

Additional subdominant modes, modelled by SEOBNRv4PHM, could be added to the principal component regression model. This would lead to consider $(5, \pm m)$ inertial modes for $m \leq 5$ and respectively $(4, \pm m)$ and $(3, \pm m)$ inertial modes. It is especially important for parameter inference purpose, allowing unbiased estimates.

SEOBNRv4P computes modes' amplitude and phase in a (non-inertial) co-precessing P attached to the Newtonian orbital angular momentum $\vec{L}_N(t)$. In `LALSimulation` library, the modes are rotated and mapped to the inertial frame I with the Wigner D-matrices as in (3.7). Expressions of the quadruplet $[a(t), \theta(t), \chi(t), \varphi(t)]$ according to the rotation parameters between the two frames P and I, and the amplitudes and phases in the precessing frame, are given in

Chapter 4. Given the modes' amplitude and phase in the precessing frame, as well as the rotation parameters, the Euler angle parametrization of the inertial modes could be computed without the discrete quaternion Hilbert transform. Thus, the dataset construction might not be limited by Euler angle indeterminacy considerations. Unfortunately, because of technical reasons we were limited in the usage of `LALSimulation` code and could not benefit from such simulation sub-products.

The conclusion of Chapter 1 mentioned that the represention with instantaneous Stokes parameters and instantaneous frequency is more adapted for the analysis of non-stationary polarized signals, mainly because it is not submitted to undetermination problems (that we avoided by rotating the inertial frame and limiting the effective precession spin). However, in this situation this representation is not appropriate since the instantaneous frequency needs to be summed to construct the full waveform. The phase regression error cumulates in the integral causing the final performance to drop.

3.5 Summary

Thanks to the recent introduction of new detectors and the sensitivity improvement of the LIGO and Virgo detectors[26], it is expected to see more events (of order 200 expected during O4 and 500 during O5) during the next observing runs. It will be more and more important to have fast generative model of gravitational waveforms in order to use efficiently the computational ressources. Consistently with the past observing runs, it is likely that non-precessing BBHs will be prevalent, but we expect to see wider variety of sources such as precessing binaries as already indicated in the most recent observations.

26: The commissioning of the detectors is currently progressing.

We presented a principal component regression model able to generate gravitational waveforms accurately. The proposed model is fast to evaluate and can greatly reduce the parameter inference computational budget. It has been interfaced with the Bayesian inference library Bilby for gravitational wave astronomy, and shows consistent posterior estimation compared to other waveform models.

The generative model is extended to precessing BBHs' waveforms. Although the model is not able to reach the required

performance level, we presented promising results. As discussed in the previous section, the model can be extended to other regions of the parameter space, i.e. higher dimensionless effective precession spin, as well as to include subdominant modes. Further investigation would require more computational power during the training phase.

4 Gravitational-wave polarimetric analysis

Unmodeled pipelines perform gravitational-wave detection and reconstruction without a precise physical model and with a very few a priori on the targetted waveform. They allow to discover unanticipated sources, as for GW150914 [18], and to identify new components from the gravitational-wave signature that was not anticipated by the theory of general relativity.

Gravitational waves being intrinsically bivariate, their polarimetric analysis may be particularly useful in the "agnostic" context where one does not formulate an a priori on the nature of the source. This has not received much attention in the litterature so far.

The difficulty comes from the measurement method, which provides as observable a linear combination of the two polarization modes waveforms h_+ and $h_\times$. The reconstruction of these variables or of the signal polarization parameters is thus necessary. As a consequence, this requires to first localize the source in the sky.

This chapter introduces an original method to regularize this ill-posed inverse problem by imposing an a priori on the polarization of the targeted signal. The application of this method is presented in a realistic setting.

For compact star mergers, gravitational waveforms are modelled as a sum of non stationary polarized signals whose instantaneous polarization parameters depend on the orientation of the line of sight with respect to the orbital plane. Through the use of a source frame on which the conjugate symmetry holds between opposite waveform m-modes, the instantaneous polarization state and instantaneous frequency of the polarized components are derived.

The polarimetric analysis of gravitational waves is of particular interest for the observation of precession of the orbital plane. Its observation amounts to detect a variation in the polarization state of the received signal [72]. In this context, a general SNR-like quantity is introduced in order to quantify the detectability of the polarization state of a signal in an additive Gaussian noise.

[72]: Flamant et al. (2018), *Non-parametric characterization of gravitational-wave polarizations*

4.1 Observations with a detector network

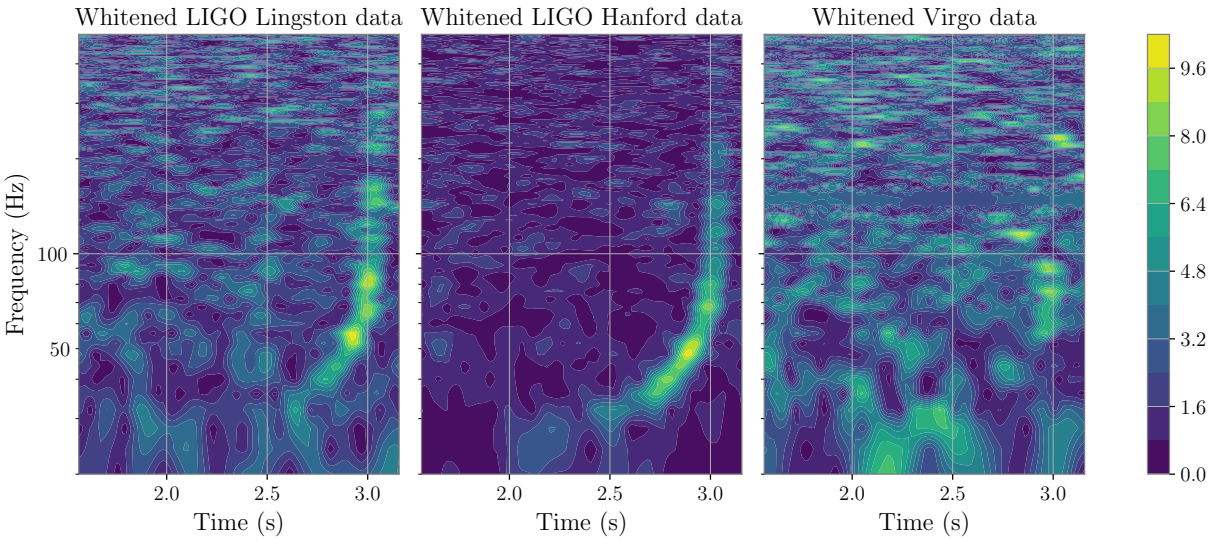

Figure 4.1: Simulated gravitational wave signal (energy spectrogram) as observed by the three LIGO and Virgo detectors. The properties of the source are described in Section 4.2.4.

As introduced in Equation (2.1), the strain measured by a detector depends on the antenna pattern of the detector $\left[F_+\left(\delta,\phi,\psi\right), F_\times\left(\delta,\phi,\psi\right)\right] \in \mathbb{R}^2$ such as

$$x_d(t) = h_+(t)F_+^d\left(\delta,\phi,\psi\right) + h_\times(t)F_\times^d\left(\delta,\phi,\psi\right) + n_d(t),$$

where $\left(\delta,\phi\right) \in \mathbb{R}^2$ denotes the position of the source in the sky in spherical coordinates (i.e. longitude and latitude respectively), ψ is the so called polarization angle[1] and $n_d(t)$ is an additive noise. If the observation time is sufficiently short[2] then the Earth rotation can be neglected.

Gravitational-waves travel at the speed of light and reach the detectors at different times. The current three detectors network observation can be written as the following linear vectorial equation:

$$\begin{bmatrix} x_L(t-\tau_{L,\delta,\phi}) \\ x_H(t-\tau_{H,\delta,\phi}) \\ x_V(t-\tau_{V,\delta,\phi}) \end{bmatrix} = \begin{bmatrix} F_+^L\left(\delta,\phi,\psi\right) & F_\times^L\left(\delta,\phi,\psi\right) \\ F_+^H\left(\delta,\phi,\psi\right) & F_\times^H\left(\delta,\phi,\psi\right) \\ F_+^V\left(\delta,\phi,\psi\right) & F_\times^V\left(\delta,\phi,\psi\right) \end{bmatrix} \begin{bmatrix} h_+(t) \\ h_\times(t) \end{bmatrix} + \begin{bmatrix} n_L(t-\tau_{L,\delta,\phi}) \\ n_H(t-\tau_{H,\delta,\phi}) \\ n_V(t-\tau_{V,\delta,\phi}) \end{bmatrix} \tag{4.1}$$

where the subscripts L, H, V stand for the LIGO Livingston, LIGO Hanford and Virgo detectors. As an illustration, Figure 4.1 shows a simulated gravitational-wave signal corresponding to a BBH of total mass 40 $M_\odot$ added to LIGO and Virgo noise. In a more compact form

$$\mathbf{x}(t;\delta,\phi) = F\left(\delta,\phi,\psi\right)\mathbf{h}(t) + \mathbf{n}(t;\delta,\phi) \tag{4.2}$$

1: The polarization angle corresponds to a rotation of the polarization basis, see Figures 2.4 and 2.5.

2: In practice the observation time is shorter than few tenths of seconds which suffices for this assumption to remain valid.

where $\mathbf{x}(t;\delta,\phi)$ denotes the recorded signal of the network, $F\left(\delta,\phi,\psi\right)$ is the beam pattern matrix composed of the detectors' antenna patterns, $\mathbf{h}(t)$ is the bivariate gravitational wave signal and $\mathbf{n}(t;\delta,\phi)$ is the network additive noise. According to the sky position, the time shifts $\tau_{.,\delta,\phi}$ map the three observation times in a common frame related to the Earth center. The noises $n_L(t)$, $n_H(t)$, $n_V(t)$ are supposed to be independent and stationary[3].

As shown in Equation (4.2), the signal lies in a two dimensional plane given by span $\left\{F_+\left(\delta,\phi,\psi\right), F_\times\left(\delta,\phi,\psi\right)\right\}$ where $F_+\left(\delta,\phi,\psi\right)$ and $F_\times\left(\delta,\phi,\psi\right)$ are the two columns of the network antenna pattern in (4.1).

3: The noise is supposed to be stationary during the observation time. In practice, drifts are observed on longer time periods in addition to transient noises that can overlap intermittently with gravitational-wave signals.

4.1.1 The polarization angle

As discussed in Section 2.2.1, the polarization angle characterizes the orientation of the polarization basis with respect to the observer frame. It is not an observable as it corresponds to a rotation of the antenna pattern[4], i.e. for ψ_0 and ψ_1 two given polarization angles, the corresponding antenna pattern vectors are related by

$$F_+(\delta,\phi,\psi_1) = \cos 2\Delta_\psi F_+(\delta,\phi,\psi_0) + \sin 2\Delta_\psi F_\times(\delta,\phi,\psi_0),$$
$$F_\times(\delta,\phi,\psi_1) = -\sin 2\Delta_\psi F_+(\delta,\phi,\psi_0) + \cos 2\Delta_\psi F_\times(\delta,\phi,\psi_0),$$

where $\Delta_\psi = \psi_1 - \psi_0$. This means that $F(\delta,\phi,\psi_1)h(t) = F(\delta,\phi,\psi_0)R(-2\Delta\psi)h(t)$ where $R(-2\Delta\psi)$ is the 2×2 rotation matrix of angle $-2\Delta\psi$.

4: Another way to see it is to write the network observation in the complex formalism as

$$x(t) = \mathrm{Re}\left\{F(\delta,\phi)e^{-2i\psi}h(t)\right\} + n(t),$$

where $x(t)$, $n(t) \in \mathbb{R}^3$, $h(t) = h_+(t) - ih_\times(t) \in \mathbb{C}$ and $F(\delta,\phi) = F_+(\delta,\phi,0) + iF_\times(\delta,\phi,0) \in \mathbb{C}^3$.

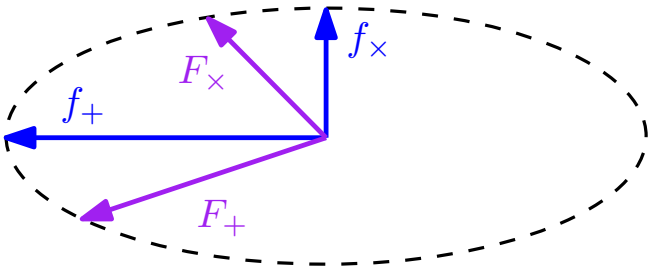

Figure 4.2: Dominant polarization frame vectors $(f_+, f_\times)$ compared to antenna pattern vectors $(F_+, F_\times)$ associated to a given polarization frame, i.e. a given $\psi \neq \psi^{\mathrm{DPF}}$.

A preferred frame for the definition of the polarization angle is given by the dominant polarization frame (DPF) [73]. For any sky coordinates (δ,ϕ), the dominant polarization frame is defined by ψ^{DPF} such that the network antenna pattern vectors $f_+(\delta,\phi) = F_+(\delta,\phi,\psi^{\mathrm{DPF}})$ and $f_\times(\delta,\phi) = F_\times(\delta,\phi,\psi^{\mathrm{DPF}})$ are orthogonal and $\left\|f_+(\delta,\phi)\right\| \geqslant \left\|f_\times(\delta,\phi)\right\|$, see Figure[5] 4.2. A direct computation leads to

[73]: Klimenko et al. (2005), *Constraint likelihood analysis for a network of gravitational wave detectors*

5: Note that all the developments presented are for a network of three detectors because this allows a clear geometrical interpretation, but the results remain valid for a larger network.

$$\psi^{\mathrm{DPF}} = \frac{1}{4}\arctan 2\,\frac{2\left\langle F_+(\delta,\phi,0), F_\times(\delta,\phi,0)\right\rangle}{\left\|F_\times(\delta,\phi,0)\right\|^2 - \left\|F_+(\delta,\phi,0)\right\|^2}, \tag{4.3}$$

where arctan2 stands for the four-quadrant inverse tangent. $f_+(\delta,\phi)$ and $f_\times(\delta,\phi)$ are named the DPF vectors.

For now on, in order to simplify the expressions, we suppose that the line of sight is known so the dependence of the antenna pattern on the line of sight (δ,ϕ) is dropped and the detectors observations are time shifted so the waveforms $h_+(t)$ and $h_\times(t)$ are aligned in each detector and (4.1) holds.

Polarization has received little interest in the gravitational wave data analysis community so far because there are limitations for their reconstruction and analysis. First, the reduced number of detectors make difficult the location of the source which is necessary in order to write (4.2). For the majority of the detected signals only two detectors are involved, the SNR being not equilibrated between the detectors, when at least three are needed for an accurate localization. Second, due to the low noise level, accurate reconstruction methods are restrained to the single axis $f_+(\delta,\phi)$ of the two-dimensional plane spanned by $\left\{f_+(\delta,\phi),\ f_\times(\delta,\phi)\right\}$. Based on the work presented in Chapter 1, we aim to bring new methods exploiting the fact that $h(t)$ is an amplitude, frequency and polarization modulated signal or the sum of several such signals.

4.1.2 Polarimetric characterization of the noise

A common assumption on the detector noises is that they are Gaussian, stationary and independent from a detector to the other. The detector noise is characterized in the frequency domain by its power spectral density $S_d(\omega)$, where ω is the frequency variable. The amplitude spectral densities $\sqrt{S_d(\omega)}$ can be estimated on a segment of LIGO-Virgo data[6] as shown in Figure 4.3.

6: See Section 4.2.4 for details about the corresponding data segment and the chosen sky position (δ,ϕ).

The covariance matrix of the detector network is constructed from these estimated noise spectral densities. For each frequency, we get the noise covariance matrix

$$\Delta(\omega) = \begin{bmatrix} S_L(\omega) & 0 & 0 \\ 0 & S_H(\omega) & 0 \\ 0 & 0 & S_V(\omega) \end{bmatrix}. \tag{4.4}$$

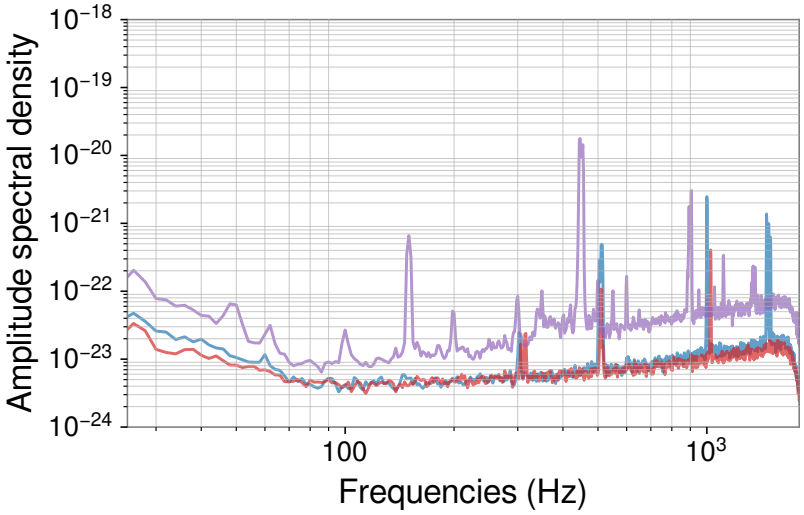

Figure 4.3: Estimated amplitude spectral densities (Welch's method) of the data segment for Virgo (purple), LIGO Livingston (blue) and LIGO Hanford (red) used to reconstruct the signal.

Then, equation (4.2) can be rewritten in the frequency domain with the whitened detectors' observations, such as

$$\tilde{X}(\omega) = \tilde{F}(\omega;\psi)\, H(\omega) + \tilde{N}(\omega), \tag{4.5}$$

where $\tilde{X}(\omega) = \Delta^{-1/2} X(\omega)$ is the whitened vector of observations, $\tilde{F}(\omega;\psi) = \Delta(\omega)^{-1/2} F(\psi)$ is the noise-scaled beam pattern and similarly for $\tilde{N}(\omega)$ which is now a standard white Gaussian noise.

The projection operator on the noise-scaled signal plane span $\left\{\tilde{F}_+(\omega;\psi), \tilde{F}_\times(\omega;\psi)\right\}$ is given by the Moore-Penrose inverse of the noise-scaled beam pattern matrix

$$\tilde{F}^\dagger(\omega;\psi) = \left(\tilde{F}^T(\omega;\psi)\,\tilde{F}(\omega;\psi)\right)^{-1} \tilde{F}(\omega;\psi). \tag{4.6}$$

The covariance matrix of the noise projection in the noise-scaled wave plane $\tilde{F}^\dagger(\omega;\psi)\,\tilde{N}(\omega)$ is given by

$$V(\omega) = \tilde{F}^\dagger(\omega;\psi)\,(\tilde{F}^\dagger(\omega;\psi))^T. \tag{4.7}$$

By definition of the Moore-Penrose inverse, we get $V(\omega) = (\tilde{F}^T(\omega;\psi)\,\tilde{F}(\omega;\psi))^{-1}$. It is straightforward to get

$$V(\omega) = \frac{\left\|\tilde{F}_+(\omega;\psi)\right\|^{-1}\left\|\tilde{F}_\times(\omega;\psi)\right\|^{-1}}{1-c^2(\omega;\psi)} \begin{bmatrix} \kappa(\omega;\psi) & -c(\omega;\psi) \\ -c(\omega;\psi) & \kappa^{-1}(\omega;\psi) \end{bmatrix}. \tag{4.8}$$

where

$$c(\omega;\psi) = \frac{\left\langle \tilde{F}_+(\omega;\psi), \tilde{F}_\times(\omega;\psi)\right\rangle}{\left\|\tilde{F}_+(\omega;\psi)\right\|\left\|\tilde{F}_\times(\omega;\psi)\right\|} \quad \text{and} \quad \kappa(\omega;\psi) = \frac{\left\|\tilde{F}_\times(\omega;\psi)\right\|}{\left\|\tilde{F}_+(\omega;\psi)\right\|} \tag{4.9}$$

Choosing $\psi = \psi^{\mathrm{DPF}}$ where ψ^{DPF} is the polarization angle of the dominant polarization frame defined with the noise-scaled antenna pattern, i.e. ψ^{DPF} is such that $\tilde{f}_+(\omega) = \tilde{F}_+\left(\omega; \psi^{\mathrm{DPF}}\right)$ and $\tilde{f}_\times(\omega) = \tilde{F}_\times\left(\omega; \psi^{\mathrm{DPF}}\right)$ are orthogonal and $\kappa\left(\omega; \psi^{\mathrm{DPF}}\right) \leqslant 1$, then

$$V(\omega) = \begin{bmatrix} \left\|\tilde{f}_+(\omega)\right\|^{-2} & 0 \\ 0 & \left\|\tilde{f}_\times(\omega)\right\|^{-2} \end{bmatrix}. \tag{4.10}$$

Equation (4.10) shows that in the DPF, the *plus* and *cross* components[7] of the noise are independent. Since $\kappa\left(\omega; \psi^{\mathrm{DPF}}\right) \leqslant 1$, the noise power is higher in the *cross* component than in the *plus* component.

7: By the *plus* and *cross* components, we call the parts of the noise aligned with $\tilde{f}_+(\omega)$ and $\tilde{f}_\times(\omega)$ respectively.

The polarization of the noise is embedded in the covariance matrix[8] $V(\omega)$. In the DPF, the Stokes parameters of the noise are given by

$$\begin{aligned} S_0(\omega) &= \left\|\tilde{f}_+(\omega)\right\|^{-2} + \left\|\tilde{f}_\times(\omega)\right\|^{-2}, \\ S_1(\omega) &= \left\|\tilde{f}_+(\omega)\right\|^{-2} - \left\|\tilde{f}_\times(\omega)\right\|^{-2}, \\ S_2(\omega) &= S_3(\omega) = 0. \end{aligned} \tag{4.11}$$

8: One has that [1]

$$\begin{aligned} S_0(\omega) &= \mathbb{E}\left|n_+(\omega)\right|^2 + \mathbb{E}\left|n_\times(\omega)\right|^2, \\ S_1(\omega) &= \mathbb{E}\left|n_+(\omega)\right|^2 - \mathbb{E}\left|n_\times(\omega)\right|^2, \\ S_2(\omega) &= 2\,\mathrm{Re}\mathbb{E}\left\{n_+(\omega)\overline{n_\times}(\omega)\right\}, \\ S_3(\omega) &= 2\,\mathrm{Im}\mathbb{E}\left\{n_+(\omega)\overline{n_\times}(\omega)\right\}. \end{aligned}$$

for a given bivariate stochastic process $n(t) = [n_+(t), n_\times(t)]^T$.

Figure 4.4 shows the normalized Stokes parameters estimated on a segment of the LIGO-Virgo detectors data[9].

9: The data segment and the sky location used for the estimation are described in Section 4.2.4.

The estimated spectral polarization degree defined as

$$\Phi_n(\omega) = \frac{\sqrt{\mathbb{E}\left\{S_1(\omega)\right\}^2 + \mathbb{E}\left\{S_2(\omega)\right\}^2 + \mathbb{E}\left\{S_3(\omega)\right\}^2}}{\mathbb{E}\left\{S_0(\omega)\right\}} \tag{4.12}$$

is also given. This quantity is the fraction of polarized noise power ($0 \leqslant \Phi_n(\omega) \leqslant 1$)at frequency ω [1]: $\Phi_n(\omega) = 1$ for a fully polarized stochastic signal, and $\Phi_n(\omega) = 0$ for an unpolarized signal. As for the amplitude spectral density, the polarization degree is invariant with respect to the polarization angle (this is not the case for the normalized Stokes parameters).

In the wave plane span $\left\{\tilde{f}_+(\delta, \phi),\ \tilde{f}_\times(\delta, \phi)\right\}$, the noise is thus strongly polarized, which means that its observed polarization state is stable over time. By construction of the DPF, it is linearly polarized along the *cross* direction. This indicates that $h_\times$ measurements are much more noisy than that of h_+.

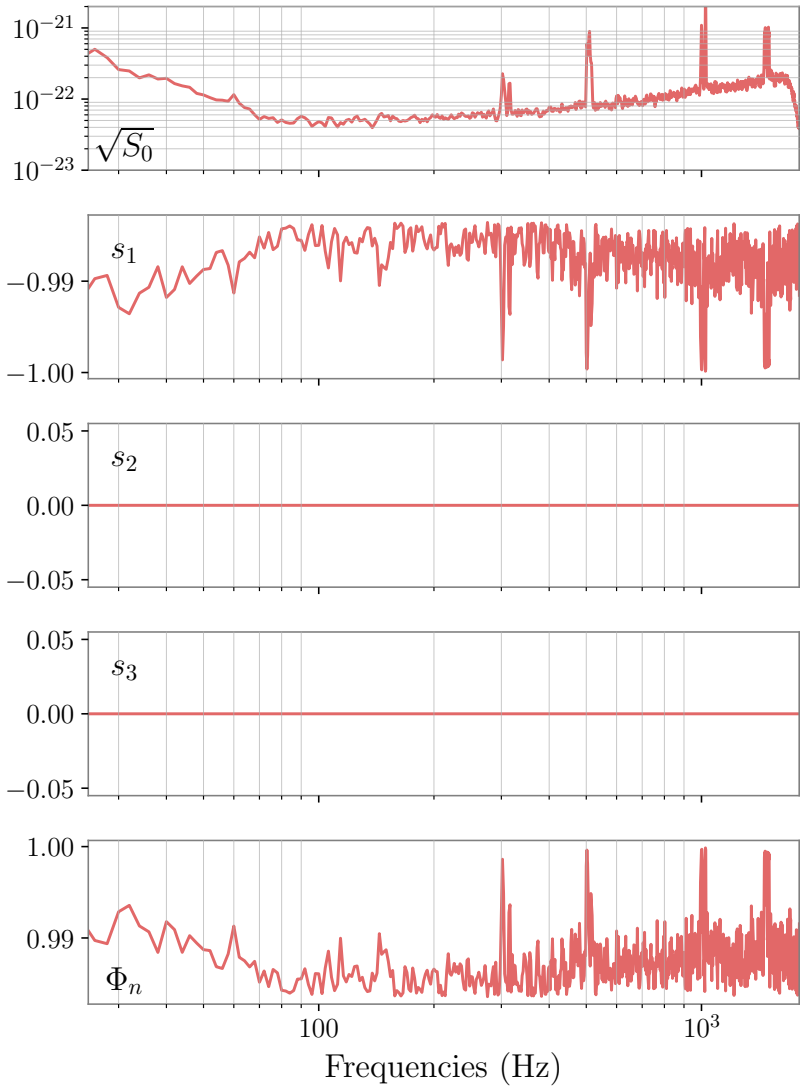

Figure 4.4: Estimated normalized noise Stokes parameters $(s_1(\omega), s_2(\omega), s_3(\omega))$ and polarization degree $\Phi_n(\omega)$. The amplitude of the noise is given by $\sqrt{S_0(\omega)}$. The Stokes parameters are computed with (4.11) from the estimated power spectral densities of the detectors shown in Figure 4.3.

Note that the estimated polarization parameters presented in Figure 4.3 are dependent on the chosen line of sight. One would have different values for a different choice of (δ, ϕ).

4.2 Reconstruction of gravitational-wave signals

It follows from Equation (4.11) that the noise of the detector network is linearly polarized: the noise is mostly located in the *cross* component. As expected this complicates the reconstruction of $h_\times$ from noisy observations. Contrarily to the noise, in general the gravitational-wave strain is not necessarily linearly polarized (it is not for compact-star binary mergers that are not edge-on, i.e. $\iota \neq \pi/2$). Based on these differences in the polarization patterns this section presents a

new regularization term which promotes certain polarizaton states.

4.2.1 Standard approach

As it clearly appears from (4.5), the reconstruction of the gravitational-wave strain h from noisy data is an inverse problem. This problem is generally ill posed as for a great part of the sky, the mixing matrix $\tilde{F}_\times(\omega;\psi)$ is ill conditionned, i.e. $\kappa\left(\omega;\psi^{\mathrm{DPF}}\right) \ll 1$ in (4.9). Geometrically, this means that for an arbitrary polar angle ψ, $\tilde{F}_+(\omega;\psi)$ and $\tilde{F}_\times(\omega;\psi)$ are nearly aligned or one of them is close to zero. For instance, the cross component $h_\times$ cannot be retrieved when $\kappa\left(\omega;\psi^{\mathrm{DPF}}\right) = 0$.

We propose an approach where the reconstruction problem is modeled as an optimization problem with a data fidelity term $\Psi(h,x)$ and a regularization term $\Omega(h)$, the reconstructed strain $\hat{h}$ is obtained as

$$\hat{h} = \underset{h\in\mathscr{H}}{\arg\min}\, \Psi(h,x) + \lambda\Omega(h), \tag{4.13}$$

where $\lambda > 0$ is a regularization parameter and $\mathscr{H}$ is a finite dimensional Hilbert space. Motivated by a statistical interpretation of the reconstruction scheme, the data fidelity term is often chosen as to be the log likelihood of the observations, which from equation (4.5) can be written in the time-frequency domain as the noise weighted least square function[10]

$$\Psi(h,x) = \sum_{(\omega,\tau)\in\Gamma} \frac{1}{2}\left\|\tilde{X}(\omega,\tau) - \tilde{F}(\omega)H(\omega,\tau)\right\|_2^2, \tag{4.14}$$

where Γ corresponds to time-frequency bins in which the signal is present.

Coherent Waveburst [40, 41], one of the LIGO-Virgo pipelines, follows this approach[11]. It identifies time-frequency regions with excess of power [41]. Time-frequency bins that show a statistically significant excess of power with respect to the reference noise estimation are selected. Γ is identified among the pre-selected bins with a ad-hoc clustering algorithm. Solutions of (4.13) assuming $\lambda = 0$ are given by

$$\hat{H}(\omega,\tau) = \tilde{F}^\dagger(\omega)\tilde{X}(\omega,\tau) \tag{4.15}$$

where $\tilde{F}^\dagger(\omega)$ is the Moore Penrose inverse defined in (4.6).

10: This is true under the condition that the noise is uncorrelated over the time-frequency bins.

11: Coherent Waveburst uses the likelihood ratio $\mathbb{P}(x|H_1)/\mathbb{P}(x|H_0)$ between the null hypothesis H_0 (no signal is present in the data) and the alternative hypothesis H_1 (a signal is present in the data). This allows to build maximum likelihood ratio test [73]. While the distinction from the presented developments is notably important for the detection of gravitational-wave signals, it is not significative in the restrained context of signal reconstruction.

The beam pattern vector asymmetry renders the inverse problem ill posed, in particular for the *cross* component $h_\times$. Depending on the assumptions we have about the signal being sought, regularization constraints can be added to the likelihood functional. This insures that the reconstructed signal will have desired physical properties. Regularizations have been already proposed in the form of polarization constraints [41, 73]. h_+, $h_\times$ and their quadrature parts (i.e. Hilbert transforms) are parametrized with respect to polarization parameters (e.g. ellipticity, orientation) and inverse problem solutions are derived depending on the values imposed to the polarization parameters [41, 73]. We generalize and extend those schemes by using the framework introduced for bivariate signal representations.

4.2.2 Regularization with polarization constraint

Motivated by the differences in the signal and noise polarization patterns described in Section 4.1.2, we propose a Tikhonov regularization [74] based on polarization priors. The quadratic constraint is of the form

[74]: Willoughby (1979), *Solutions of Ill-Posed Problems (A. N. Tikhonov and V. Y. Arsenin)*

$$\Omega(h) = \sum_{\omega,\tau} \frac{1}{2} \left\| L_{-\boldsymbol{\mu}(\omega,\tau)} H(\omega,\tau) \right\|_2^2 \tag{4.16}$$

where $L_{-\boldsymbol{\mu}(\omega,\tau)}$ is the Jones matrix of a polarizer [75] of axis

[75]: Gil et al. (2022), *Polarized Light and the Mueller Matrix Approach*

$$-\boldsymbol{\mu}(\omega,\tau) = (s_1(\omega,\tau), s_2(\omega,\tau), s_3(\omega,\tau)) \,, \tag{4.17}$$

such that

$$L_{-\boldsymbol{\mu}(\omega,\tau)} = \frac{1}{2} \begin{bmatrix} 1 + s_1(\omega,\tau) & s_2(\omega,\tau) + \boldsymbol{i} s_3(\omega,\tau) \\ s_2(\omega,\tau) - \boldsymbol{i} s_3(\omega,\tau) & 1 - s_1(\omega,\tau) \end{bmatrix} . \tag{4.18}$$

$L_{-\boldsymbol{\mu}(\omega,\tau)} H(\omega,\tau)$ corresponds to the quasi-projection of the polarization axis of $H(\omega,\tau)$ on $-\boldsymbol{\mu}(\omega,\tau)$. For a signal h with an orthogonal polarization state $\boldsymbol{\mu}_h(\omega,\tau) = \boldsymbol{\mu}(\omega,\tau)$, the output of the filter is $L_{\boldsymbol{\mu}(\omega,\tau)} H(\omega,\tau) = [0,0]^T$. The signal is unchanged if $\boldsymbol{\mu}_h(\omega,\tau) = -\boldsymbol{\mu}(\omega,\tau)$. Thus the regularization term (4.16) is penalizing polarizations different from the targetted axis $\boldsymbol{\mu}(\omega,\tau)$. λ is viewed as the power of the polarizing filter and can be different in each bin $(\omega,\tau) \in \Gamma$.

The linearity of the inverse problem (4.2) is preserved by the Tikhonov regularization, resulting in a closed-form solution

of the inverse problem, such that

$$\hat{H}(\omega,\tau) = \left(\tilde{F}^T(\omega)\tilde{F}(\omega) + \lambda L^T_{-\boldsymbol{\mu}(\omega,\tau)} L_{-\boldsymbol{\mu}(\omega,\tau)}\right)^{-1} \tilde{F}^T(\omega)\tilde{X}(\omega,\tau) \tag{4.19}$$

for all time-frequency bins.

Standard regularization used by Coherent Waveburst is a penalization on the *cross* component [73], and results in a soft constraint that reconstructs the maximum likelihood solution $\hat{h}_\times$ with a penalty factor. This is equivalent to choose a constant polarization prior in (4.16) with $\boldsymbol{\mu} = (1,0,0)$, i.e. a linear polarization (horizontal) prior with a constraint on the *cross* component, justified by (4.11). This standard linear polarization prior favors high signal power and near edge on sources (i.e. sources with an inclination $\iota \approx \pi/2$) with a polarization angle near ψ^{DPF} or $\psi^{\mathrm{DPF}} + \pi/2$.

A hard polarization constraint is achieved by the quasi-projection of the polarization state of the solution to the least square problem by the polarizer[12] $L_{\boldsymbol{\mu}(\omega,\tau)}$, such that

$$\hat{H}(\omega,\tau) = L_{\boldsymbol{\mu}(\omega,\tau)}\tilde{F}^\dagger(\omega)\tilde{X}(\omega,\tau), \tag{4.20}$$

where $\boldsymbol{\mu}(\omega,\tau)$ corresponds to the targeted polarization state. For example, choosing $\boldsymbol{\mu} = (1,0,0)$ will reconstruct $\hat{h}_+$ as the solution of the least square problem (given by (4.15)) and $\hat{h}_\times \equiv 0$.

12: Notice that for the hard constraint the sign of $\boldsymbol{\mu}$ is unchanged, while the polarizer is defined with respect to $-\boldsymbol{\mu}$ for the soft constraint.

4.2.3 Regularization with polarization and sparsity constraints

Gravitational-wave signals are supposed to be decomposed in a small number of time-frequency bins [76]. Based on this assumption, the proposed reconstruction method can be refined by including additional regularization terms, notably on the number and distribution of the time-frequency coefficients of the desired signal.

[76]: Bammey et al. (2018), *Sparse Time-Frequency Representation of Gravitational-Wave signals in Unions of Wilson Bases*

A sparsity prior can be included by an additional regularization term with the non smooth functional $\Phi(H(\omega,\tau)) = \|H(\omega,\tau)\|_1$. In this case, the objective functional becomes

$$\sum_{(\omega,\tau)\in\Gamma} \frac{1}{2}\left\|\tilde{X}(\omega,\tau) - \tilde{F}(\omega)H(\omega,\tau)\right\|_2^2 + \frac{\lambda_2}{2}\left\|L_{\boldsymbol{\mu}(\omega,\tau)}H(\omega,\tau)\right\|_2^2 + \lambda_1\left\|H(\omega,\tau)\right\|_1, \tag{4.21}$$

where the regularization constants λ_1 and λ_2 can be functions of (ω, τ).

The Iterative Shrinkage-Thresholding Algorithm (ISTA) [77] is often used for the resolution of the Lasso: $\arg\min_h \Psi(h) + \lambda\Phi(h)$. Combettes et al. [78] have extended ISTA to the case of general non smooth regularizer. For a non smooth function Φ taking finite dimensional complex entries, a forward-backward algorithm is defined with a proximity operator given by

$$\text{prox}_\Phi(z) = \arg\min_u \frac{1}{2}\|z-u\|_2^2 + \Phi(u), \tag{4.22}$$

where z is a finite dimension complex vector. The general algorithm is given in the context of a least square data fidelity term and a polarization prior in Algorithm 1[13].

[77]: Beck et al. (2009), *A Fast Iterative Shrinkage-Thresholding Algorithm for Linear Inverse Problems*

[78]: Combettes et al. (2005), *Signal Recovery by Proximal Forward-Backward Splitting*

13: Algorithm 1 takes the part of representing the quadratic part of (4.21) as a single quadratic operator $Q(H(\omega,\tau)) = \Psi(H(\omega,\tau)) + \lambda_2\Gamma(H(\omega,\tau))$ in order to simplify the reading.

Algorithm 1: ISTA

$H^{(1)} \in \mathbb{C}^{M,N}$, $k = 1$, $\lambda_{1,2} \in \mathbb{R}_+$

$\Xi(\omega,\tau) = \left(\tilde{F}^T(\omega)\tilde{F}(\omega) + \lambda_2 L^*_{\boldsymbol{\mu}(\omega,\tau)} L_{\boldsymbol{\mu}(\omega,\tau)}\right)$;

$\gamma(\omega,\tau) = \|\Xi(\omega,\tau)\Xi^*(\omega,\tau)\|$;

repeat

  $\nabla Q^{(k)}(\omega,\tau) = \Xi(\omega,\tau)H^{(k)}(\omega,\tau) - \tilde{F}^T(\omega)\tilde{X}(\omega,\tau)$;

  $H^{(k+1)}(\omega,\tau) =$

  $\text{prox}_{\frac{\lambda_1}{\gamma(\omega,\tau)}\Phi}\left(H^{(k)}(\omega,\tau) - \frac{1}{\gamma(\omega,\tau)}\nabla Q^{(k)}(\omega,\tau)\right)$;

  $k = k+1$;

until *convergence*;

In the case of a sparsity prior (4.21), the proximity operator of Algorithm 1 is given by the soft-thresholdling operator, i.e. $\text{prox}_{\frac{\lambda_1}{\gamma(\omega,\tau)}\Phi} = \mathbb{S}_{\frac{\lambda_1}{\gamma(\omega,\tau)}}$, where

$$\mathbb{S}_\lambda(H(\omega,\tau)) = H(\omega,\tau)\max\left(1 - \frac{\lambda}{|H(\omega,\tau)|}, 0\right). \tag{4.23}$$

As a generalization of the Lasso, structured/social sparsity regularization [79, 80] has shown promizing results on several applications [81–83] including gravitational-wave reconstruction [84]. Contrarily to the Lasso regularization, this approach amounts to impose a prior on the repartition of the time-frequency coefficients of the signal. The regularization is achieved by the introduction of mixed norms and expansion operators [80].

[79]: Kowalski et al. (2009), *Structured Sparsity: from Mixed Norms to Structured Shrinkage*

[80]: Kowalski et al. (2013), *Social Sparsity! Neighborhood Systems Enrich Structured Shrinkage Operators*

[81]: Costa et al. (2017), *Bayesian EEG source localization using a structured sparsity prior*

[82]: Jia et al. (2012), *Robust and Practical Face Recognition via Structured Sparsity*

[83]: Siedenburg et al. (2014), *Audio declipping with social sparsity*

[84]: Feng et al. (2018), *Structured sparsity regularization for gravitational- wave polarization reconstruction*

For these methods, solutions are constructed by adapting the proximity operator of the general proximal gradient descent method presented in Algorithm 1. For instance, the Persistent Empirical Wiener (PEW) proximity operator [83] is given by

$$\mathbb{S}_{\lambda}^{\mathrm{PEW}}(H(\omega,\tau)) = H(\omega,\tau)\max\left(1 - \frac{\lambda^2}{\sqrt{\sum_{(\omega',\tau')\in\Gamma_{\omega,\tau}} C_{\omega,\tau}(\omega',\tau')\,|H(\omega',\tau')|^2}}, 0\right), \tag{4.24}$$

where $\Gamma(\omega,\tau)$ is a set of indices forming a neighborhood of the time-frequency bin (ω,τ) and $C_{\omega,\tau} \in \mathbb{C}^{2\times|\Gamma_{\omega,\tau}|}$ is a collection of weights over the neighborhood such that $\|C_{\omega,\tau}\|_2 = 1$. That is, for each (ω,τ), the neighborhood time-frequency bins are involved in the shrinkage operator. This tends to discard isolated large coefficients and keep coefficients with an appropriate neighborhood. Different weights correspond to different clustering effects. The exponentiation of λ tends to preserve energetic coefficients $H(\omega,\tau)$, which leads to better performances in this one step reconstruction procedure [83].

4.2.4 Results

The proposed regularization methods with a polarization promoting prior are implemented and tested on realistic synthetic data. For each LIGO and Virgo detectors, we considered a noisy data segment of the third observing run [68]. The data segment start from January 29, 2020 at 06 : 54 GMT and last ~ 7 sec.

A gravitational-wave signal is generated using SEOBNRv4 [58] for a black hole binary with non spinning bodies of masses $20\,M_\odot$ each, at a distance of 500 Mpc, see Figure 4.5. The binary is viewed face-on ($\iota = \varphi_0 = 0$) which corresponds to a constant circular polarization (see section 4.3).

The position of the source in the sky is fixed to $(\delta,\phi) = (\pi/4,\pi/4)$. The polarization angle of the injected signal corresponds to the DPF polarization angle. Both the noise and the signal are filtered with an high-pass filter with a cutting frequency of 25 Hz. The network SNR is 20, it is 13, 14 and 5 for the LIGO Livingston, LIGO Hanford and Virgo detectors

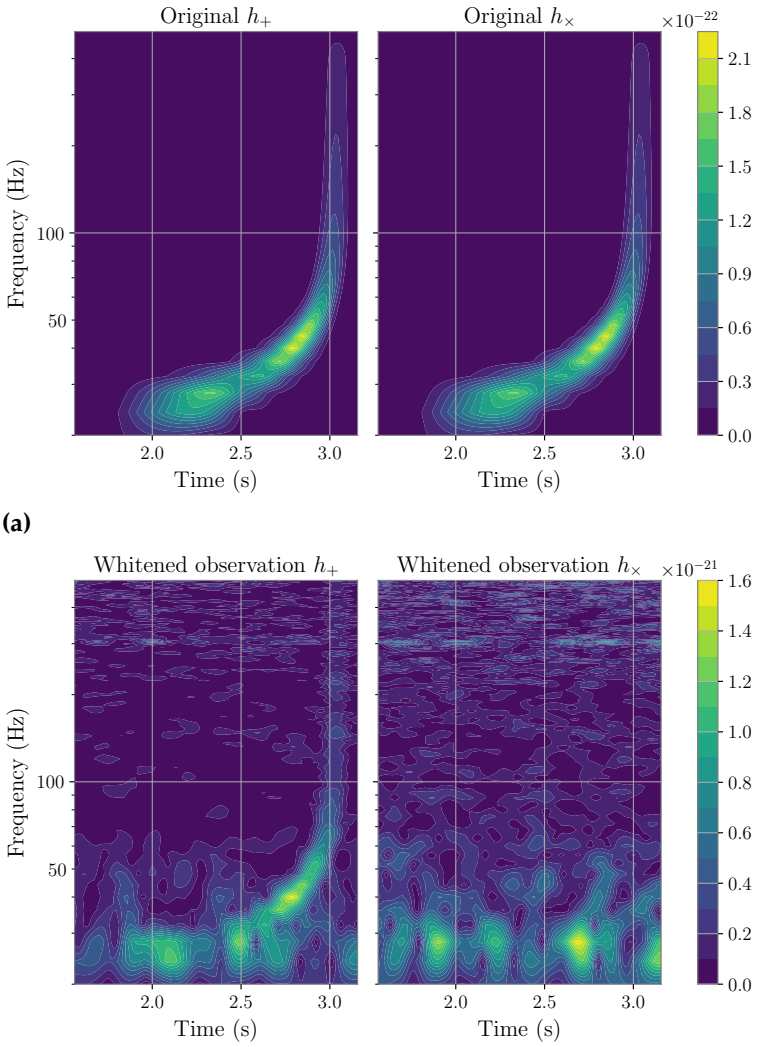

Figure 4.5: Injected signal (energy spectrogram) **(a)** and whitened observations **(b)** in the wave plane.

respectively. For the reconstruction, a time-frequency region Γ is roughly selected around the event (see the time-frequency region corresponding to Figure 4.5).

Polarization prior In this example, the injected waveform is circularly polarized and a high circular polarization regularization leads to better a result. However, in order to illustrate the variability offered by the penalization coefficient λ_2, the reconstruction result is presented for $\lambda_2 = 0.1$ and $\boldsymbol{\mu} = (0, 0, -1)$ in Figure 4.7. The effect of the constraint is seen from row **(a)** to row **(b)**, where the polarization of the signal has partially changed. In addition, the ridge of the signal is partially reconstructed. For real applications, λ_2 should be adapted to the degree of confidence in favor of a given polarization state.

Structured sparsity and polarization prior For simplicity, the polarization prior and the weights of the PEW operator are fixed over the time-frequency bins. The weights are defined such that

$$C = \begin{bmatrix} 0 & 0 & 1 \\ 0 & 1 & 0 \\ 1 & 0 & 0 \end{bmatrix}, \tag{4.25}$$

which favors diagonal time-frequency clusters. The reconstruction result is presented for $\lambda_2 = 2$, $\lambda_1 = 3$ and $\boldsymbol{\mu} = (0, 0, -1)$ in Figures 4.6 and 4.7. This defined a strong (not hard) constraint on both the structure of the time-frequency clusters and the reconstructed polarization. The ridge of the signal is selected by the structured sparsity prior. The end of the ridge is not selected as it is vertical and does not correspond to the prior given by C.

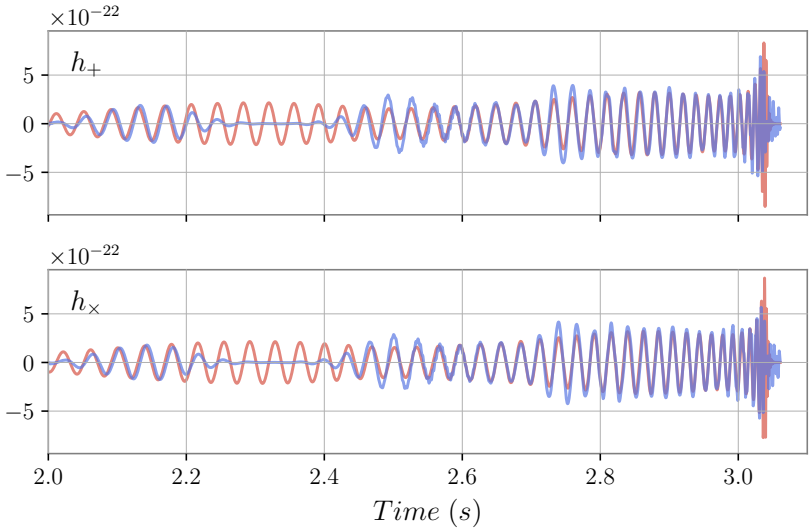

Figure 4.6: Original (red) and reconstructed (blue) polarization waveforms h_+ and $h_\times$ for a circular polarization prior ($\lambda_2 = 2$) and a structured sparsity prior ($\lambda_1 = 3$). This corresponds to Figure 4.7c.

The reconstruction accuracy is measured with the mismatch metric ϵ defined in Equation (3.5) for both the injected bivariate gravitational-wave signal h and the two polarization waveforms h_+ and $h_\times$. The different results are summarized in Table 4.1.

As highlighted by the results, the polarization constraint can help to retrieve faint signals or faint polarization waveform (e.g. $h_\times$) without imposing a strong constraint for the reconstruction. The structured sparsity addition includes a physical prior on the selected time-frequency regions, which performs better than a fixed truncation.

The hyperparameters of the presented methods (e.g. the weights of the PEW operator and others) can be empirically adjusted on a large dataset of injected signals. They can be adapted in time and frequency in order to correspond to the different phases of the waveform (inspiral, merger, ringdown).

Table 4.1: Reconstruction accuracy of the bivariate signal h and the mode waveforms h_+, $h_\times$ for different methods. The "truncated least square" and "circular polarization prior with truncation" methods involve a truncation of the time-frequency coefficients with a threshold defined by the 99.5% quantile of $S_0(\omega, \tau)$.

Reconstruction method	$\varepsilon(h, \hat{h})$	$\varepsilon(h_+, \hat{h}_+)$	$\varepsilon(h_\times, \hat{h}_\times)$
Least square	0.61	0.34	0.81
Truncated least square	0.63	0.39	0.73
Circular polarization prior ($\boldsymbol{\mu} = (0, 0, -1)$, $\lambda_2 = 2$)	0.26	0.26	0.26
Linear polarization prior ($\boldsymbol{\mu} = (1, 0, 0)$, $\lambda_2 = 2$)	0.58	0.27	0.85
Circular polarization prior with truncation ($\boldsymbol{\mu} = (0, 0, -1)$, $\lambda_2 = 2$)	0.15	0.15	0.15
Polarization prior and sparsity ($\boldsymbol{\mu} = (0, 0, -1)$, $\lambda_2 = 2, \lambda_1 = 3$)	0.14	0.12	0.15
Polarization prior and structured sparsity ($\boldsymbol{\mu} = (0, 0, -1)$, $\lambda_2 = 2, \lambda_1 = 3$)	0.13	0.14	0.13

Such weakly modelled method can retrieve faint signals with a few assumptions (e.g. with a circular polarization prior).

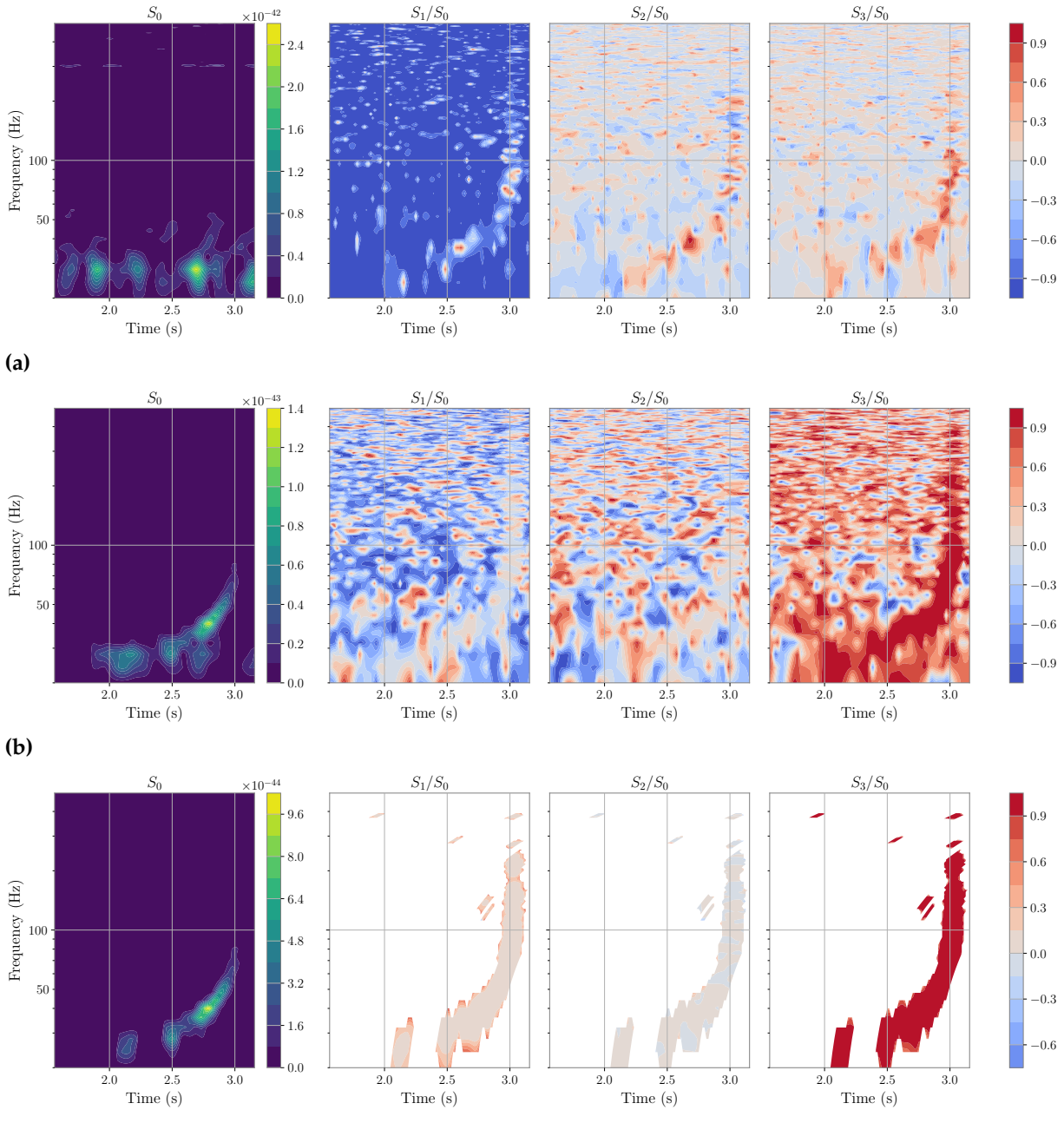

Figure 4.7: Energy and polarization spectrograms of the reconstructed signal for different methods.**(a)**: the weighted least square reconstruction, i.e. the whitened observations of the gravitational-wave signal in noisy data. **(b)**: the penalized weighted least square with a polarization prior such that $\lambda_2 = 0.1$ and $\boldsymbol{\mu} = (0, 0, -1)$. **(c)**: the penalized weighted least square with a polarization and structured sparsity prior such that $\lambda_2 = 2$, $\lambda_1 = 3$ and $\boldsymbol{\mu} = (0, 0, -1)$.

4.3 Gravitational-wave polarization

Recent results shown that gravitational-waves emitted by BBHs are non stationary polarized signals whose polarization state can be expressed with respect to the orientation of the orbital plane [72]. In this section, previous results are generalized to provide a decomposition of gravitational waveforms as the sum of polarized components with a "model-independent" approach[14].

14: The approach does not lie in a particular waveform model as presented in Section 3.2.2.

4.3.1 Co-precessing source frame

Binaries assembled dynamically in dense stellar environments are likely to contain black holes with isotropic random spin orientations. As discussed in Chapter 3, this causes the orbital angular momentum of the system $\vec{L}(t)$ and the spins of the objects $\vec{S}_1(t)$, $\vec{S}_2(t)$ to precess around the total angular momentum $J(t)$. The motion of the orbital plane is described by the normal to the orbital plane i.e. the Newtonian orbital angular momentum $\vec{L}_N(t)$, see Figure 3.12.

A co-precessing frame P is attached to the Newtonian orbital angular momentum. At each instant, a basis of the precessing frame $(\vec{e}_1^P(t), \vec{e}_2^P(t), \vec{e}_3^P(t))$ is such that $\vec{e}_3^P(t)$ is aligned with $\vec{L}_N(t)$. $\vec{e}_1^P(t)$, $\vec{e}_2^P(t)$ are chosen to satisfy a minimal rotation condition [47]. In the co-precessing frame, the effect of precession on the waveform modes is minimized.

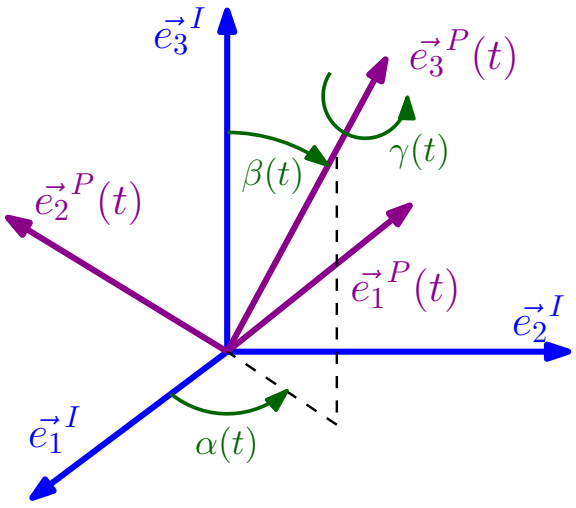

Figure 4.8: Euler angles (α, β, γ) of the rotation from the inertial frame I to the co-precessing frame P.

At $t = t_0$, where t_0 is the reference time from which the inertial frame I is defined (see Section 3.4), the precessing and inertial frames are identified. The motion of the orbital plane is parametrized by three Euler angles $(\alpha(t), \beta(t), \gamma(t))$

which correspond to the rotation from the inertial frame to the co-precessing frame with the convention zyz as illustrated in Figure 4.8. We will refer to $\beta(t)$ the opening angle between the z axis of the I and P frames as the precession angle. $\beta(t)$ and $\alpha(t)$ track the motion of $\vec{L}_N(t)$ while $\gamma(t)$ is a phase term insuring the minimal rotation condition [47].

Since the choice of the inertial frame is arbitrary, the developments presented in this chapter apply for any inertial frame I. For example, one could define an inertial frame as aligned to the total angular momentum $\vec{J}(t_0)$ and so use the corresponding definition of the triplet $(\alpha(t), \beta(t), \gamma(t))$.

Waveform modes in the co-precessing frame

In the EOB formalism, gravitational waveforms from precessing binaries are first computed in the co-precessing source frame P introduced in Section 4.3.1, such that

$$h(t) = \frac{M}{D} \sum_{l=2}^{\infty} \sum_{m=-l}^{l} h^P_{l,m}(t) {}_{-2}Y_{l,m}(\Theta(t)), \tag{4.26}$$

where $\Theta(t)$ is the time varying line of sight in the frame P.

In this frame, precession modulations of the waveform modes are limited. The precessing modes are symmetrized such that the following symmetry holds

$$h^P_{l,m}(t) = (-1)^l \overline{h^P_{l,-m}}(t) \tag{4.27}$$

as in the non-precessing case [51].

The waveform modes can be rotated with the Wigner D-matrices in order to build inertial modes, such that

$$h^I_{l,m}(t) = \sum_{m'=-l}^{l} h^P_{l,m'}(t) D^l_{m',m}(-\gamma(t), -\beta(t), -\alpha(t)), \tag{4.28}$$

from which $h(t)$ is expanded as (3.4).

4.3.2 Gravitational waveforms as a sum of polarized waveforms

The precessing modes are modeled as amplitude and frequency modulated signals, which from the conjugate sym-

metry (4.27) verify $h_{l,m}(t) = a_{l,m}(t)e^{-\boldsymbol{i}\varphi_{l,m}(t)}$ and $h_{l,-m}(t) = (-1)^l a_{l,m}(t)e^{\boldsymbol{i}\varphi_{l,m}(t)}$.

Without loss of generality, one can choose l to be even and denote $\mathfrak{h}_{l,m}$ the restriction of the gravitational waveform to the $(l, \pm m)$ precessing modes, such as

$$\mathfrak{h}_{l,m}(t) = h^P_{l,m}(t)\,{}_{-2}Y_{l,m}(\Theta(t)) + h^P_{l,-m}(t)\,{}_{-2}Y_{l,-m}(\Theta(t)). \quad (4.29)$$

One has $\mathfrak{h}_{l,m}(t) = a(t)U(t)\cos\varphi(t) - \boldsymbol{i}a(t)V(t)\sin\varphi(t)$, where

$$U(t) = {}_{-2}Y_{l,m}(\Theta(t)) + (-1)^l\,{}_{-2}Y_{l,-m}(\Theta(t)) \quad (4.30)$$

$$V(t) = {}_{-2}Y_{l,m}(\Theta(t)) - (-1)^l\,{}_{-2}Y_{l,-m}(\Theta(t)). \quad (4.31)$$

The quaternion embedding of $\mathfrak{h}_{l,m}$ is given by

$$\begin{aligned}\mathfrak{h}_{l,m\,\mathbb{H}}(t) = {} & a(t)U(t)\cos\varphi(t) + \mathscr{H}_j\left\{a_{l,m}(t)U(t)\cos\varphi_{l,m}(t)\right\}\boldsymbol{j} \\ & - \boldsymbol{i}a_{l,m}(t)V(t)\sin\varphi_{l,m}(t) - \mathscr{H}_j\left\{\boldsymbol{i}a_{l,m}(t)V(t)\sin\varphi_{l,m}(t)\right\}\boldsymbol{j}\end{aligned}$$

by linearity of the quaternion Hilbert transform $\mathscr{H}_j$. We admit that the bedrosian theorem holds such that

$$\mathscr{H}_j\left\{a_{l,m}(t)U(t)\cos\varphi(t)\right\} = a_{l,m}(t)U(t)\mathscr{H}_j\left\{\cos\varphi_{l,m}(t)\right\}$$

and that the phase verifies $\mathscr{H}_j\left\{\cos\varphi_{l,m}(t)\right\} = \sin\varphi(t)$, then

$$\mathfrak{h}_{l,m\,\mathbb{H}}(t) = a_{l,m}(t)(U(t) + V(t)\boldsymbol{k})e^{\boldsymbol{j}\varphi_{l,m}(t)}. \quad (4.32)$$

$U(t)$ and $V(t)$ can be developed with respect to the rotation from the inertial frame I to the precessing frame P given by $(\alpha(t), \beta(t), \gamma(t))$ and the line of sight in the inertial frame (ι, φ_0). To do so, we use a specific property of the spin weighted harmonics, such that

$${}_{-2}Y_{l,m}(\Theta(t)) = \sum_{m'=-l}^{l} D^l_{m,m'}(\alpha(t), \beta(t), \gamma(t))\,{}_{-2}Y_{l,m'}(\iota, \varphi_0). \quad (4.33)$$

As shown in Appendix B, we have in particular

$$\mathfrak{h}_{l,m\,\mathbb{H}}(t) = a_{l,m}(t)\left[\tilde{U}(\varphi_0 + \alpha(t), \iota, \beta(t)) + \tilde{V}(\varphi_0 + \alpha(t), \iota, \beta(t))\boldsymbol{k}\right]e^{\boldsymbol{j}(\varphi_{l,m}(t) - m\gamma(t))} \quad (4.34)$$

which states that the instantaneous phase of $\mathfrak{h}_{l,m\,\mathbb{H}}$, as defined in (1.9), is given by

$$\varphi = \varphi_{l,m}(t) - m\gamma(t). \quad (4.35)$$

The instantaneous Stokes parameters of $\mathfrak{h}_{l,m}$ can be computed with (1.17). The calculation is as follows[15]

$$\begin{aligned} |\mathfrak{h}_{l,m\,\mathbb{H}}(t)|^2 &= a_{l,m}^2(t)\left|\tilde{U}(t)+\tilde{V}(t)\boldsymbol{k}\right|^2 \\ &= a_{l,m}^2(t)\left(\left|\tilde{U}(t)\right|^2+\left|\tilde{V}(t)\right|^2\right) \end{aligned} \tag{4.36}$$

and

$$\begin{aligned} \mathfrak{h}_{l,m\,\mathbb{H}}(t)\mathfrak{h}_{l,m\,\mathbb{H}}{}^{*j}(t) &= a_{l,m}^2(t)(\tilde{U}(t)+\tilde{V}(t)\boldsymbol{k})(\tilde{U}(t)+\tilde{V}(t)\boldsymbol{k})^{*j} \\ &= a_{l,m}^2(t)\left(\tilde{U}(t)\tilde{U}(t)^{*j}+2\mathrm{Re}\left\{\tilde{U}(t)\overline{\tilde{V}(t)}\right\}\boldsymbol{k}-\tilde{V}(t)\tilde{V}(t)^{*k}\right), \end{aligned} \tag{4.37}$$

which gives the instantaneous Stokes parameters as

$$\begin{aligned} S_0(t) &= a_{l,m}^2(t)\left(\left|\tilde{U}(t)\right|^2+\left|\tilde{V}(t)\right|^2\right) \\ S_1(t) &= a_{l,m}^2(t)\left(\mathrm{Re}\left\{\tilde{U}(t)\right\}^2-\mathrm{Re}\left\{\tilde{V}(t)\right\}^2-\mathrm{Im}\left\{\tilde{U}(t)\right\}^2+\mathrm{Im}\left\{\tilde{V}(t)\right\}^2\right) \\ S_2(t) &= 2a_{l,m}^2(t)\left(\mathrm{Re}\left\{\tilde{U}(t)\right\}\mathrm{Im}\left\{\tilde{U}(t)\right\}-\mathrm{Re}\left\{\tilde{V}(t)\right\}\mathrm{Im}\left\{\tilde{V}(t)\right\}\right) \\ S_3(t) &= -2a_{l,m}^2(t)\mathrm{Re}\left\{\tilde{U}(t)\overline{\tilde{V}(t)}\right\} \end{aligned} \tag{4.38}$$

Equations (4.38) are still valid with $U(t)$ and $V(t)$. Here the distinction is made to stress that the normalized Stokes parameters are functions of $\varphi_0+\alpha(t)$, ι and $\beta(t)$.

The instantaneous polarization state (given by the normalized Stokes parameters $s_i(t)=S_i(t)/S_0(t)$, see Chapter 1) is such that $\boldsymbol{\mu}_{\mathfrak{h}_{l,m}}(\varphi_0+\alpha(t),\iota,\beta(t))$, i.e. it is only determined by the orientation of the line of sight in the co-precessing frame. The instantaneous frequency of $\mathfrak{h}_{l,m}(t)$ is computed from (1.34). Thus the waveform can be decomposed as a sum of AM-FM-PM components with different frequencies[16] $\omega_{\mathfrak{h}_{l,m}}\approx\dot{\varphi}_{l,m}(t)$.

As an illustration, Figure 4.9 shows the time-frequency transform of a simulated signal for a precessing binary. The brightest ridge of the energy spectrogram corresponds to $\mathfrak{h}_{2,2}$ and other ridges correspond to subdominant polarized components. The ridge curves are given by the instantaneous frequencies of the polarized components. Values of the Stokes parameters along the ridges are given by (4.38) and their variations are due to the precession of the orbital plane.

15: Here we abreviated $\tilde{U}(\varphi_0-\alpha(t),\beta(t),\iota)$ by $\tilde{U}(t)$ and respectively for $\tilde{V}(t)$. The calculations are always valid with $U(t)$ and $V(t)$.

16: Note that this result depends on three assumptions. The conjugate symmetry of the co-precessing modes should hold. The Bedrosian theorem requires that $\varphi_{l,m}(t)$ has sufficently high variations compared to the other parameters. More technically, the Hilbert transform requires a particular structure of $\varphi_{l,m}(t)$ in order to create a quadrature part of $\cos\varphi_{l,m}(t)$.

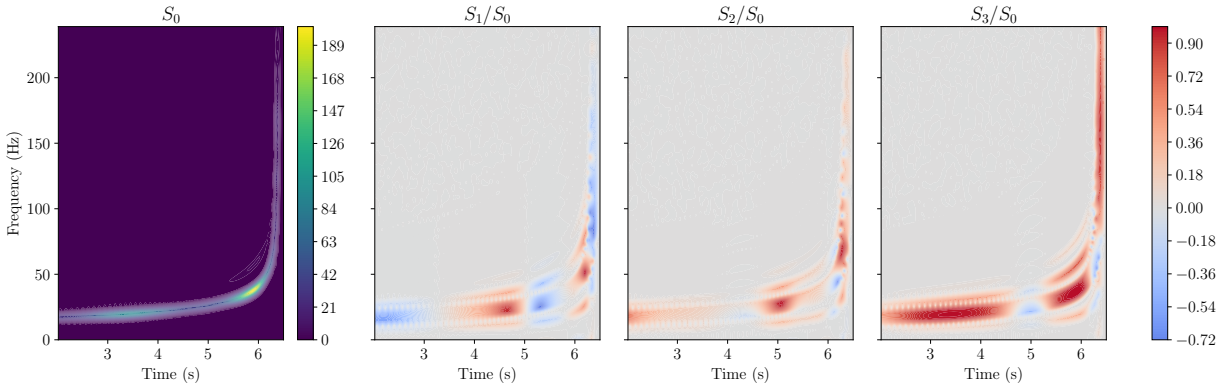

Figure 4.9: Energy and polarization spectrogram of a simulated gravitational waveform with SEOBNRv4PHM including $(2, \pm 2)$, $(2, \pm 1)$, $(3, \pm 3)$, $(4, \pm 4)$ and $(5, \pm 5)$ precessing modes. The source is a precessing binary inclined at 80 deg with bodies of masses $m_1 = 29.7\,M_\odot$, $m_2 = 8.4\,M_\odot$ and spins $\chi_x = (0.5, 0.2, 0.2)$, $\chi_y = (0.2, 0.2, 0.5)$ ($\chi_p = 0.5$).

4.3.3 The dominant polarized component $\mathfrak{h}_{2,2}$

As for spin-aligned BBHs, the $(2, \pm 2)$ modes are dominant in the co-precessing frame [85].

[85]: Babak et al. (2017), *Validating the effective-one-body model of spinning, precessing binary black holes against numerical relativity*

The restriction of the gravitational waveform to the dominant $(2, \pm 2)$ co-precessing mode is given by

$$\mathfrak{h}_{2,2}(t) = h^P_{2,2}(t)\,{}_{-2}Y_{2,2}(\Theta(t)) + h^P_{2,-2}(t)\,{}_{-2}Y_{2,-2}(\Theta(t)).$$

We present here an illustration of the previous method on the dominant AM-FM-PM component $\mathfrak{h}_{2,2}(t)$. Consider a face-on binary in the inertial frame, i.e. $\iota = \varphi_0 = 0$. Then, one obtains that:

$$\begin{aligned} {}_{-2}Y_{2,2}(\Theta(t)) &= \sum_{m'=-2}^{2} \overline{D^2_{2,m'}}(\alpha(t), \beta(t), \gamma(t))\,{}_{-2}Y_{2,m'}(0,0) \\ &= \frac{1}{2}\sqrt{\frac{5}{\pi}} \cos^4 \frac{\beta(t)}{2} e^{2i(\alpha(t)+\gamma(t))} \end{aligned} \tag{4.39}$$

and

$$\begin{aligned} {}_{-2}Y_{2,-2}(\Theta(t)) &= \sum_{m'=-2}^{2} \overline{D^2_{-2,m'}}(\alpha(t), \beta(t), \gamma(t))\,{}_{-2}Y_{2,m'}(0,0) \\ &= \frac{1}{2}\sqrt{\frac{5}{\pi}} \sin^4 \frac{\beta(t)}{2} e^{2i(\alpha(t)-\gamma(t))}. \end{aligned} \tag{4.40}$$

Knowing that $\gamma(t)$ is only involved in the instantenous phase

of $\mathfrak{h}_{2,2}$, it is dropped to gives the following terms[17]

$$\tilde{U}(t) = \frac{1}{2}\sqrt{\frac{5}{\pi}} e^{2i\alpha(t)} \left(\cos^4 \frac{\beta(t)}{2} + \sin^4 \frac{\beta(t)}{2}\right) \tag{4.41}$$

$$\tilde{V}(t) = \frac{1}{2}\sqrt{\frac{5}{\pi}} e^{2i\alpha(t)} \left(\cos^4 \frac{\beta(t)}{2} - \sin^4 \frac{\beta(t)}{2}\right) \tag{4.42}$$

Then, the expressions of the Stokes parameters are

$$\begin{aligned}
S_0(t) &= \frac{a_{2,2}^2(t)}{2}\frac{5}{\pi}\left(\sin^8 \frac{\beta(t)}{2} + \cos^8 \frac{\beta(t)}{2}\right), \\
S_1(t) &= \frac{a_{2,2}^2(t)}{16}\frac{5}{\pi}\sin^4\beta(t)\cos 4\alpha(t), \\
S_2(t) &= \frac{a_{2,2}^2(t)}{16}\frac{5}{\pi}\sin^4\beta(t)\sin 4\alpha(t), \\
S_3(t) &= \frac{a_{2,2}^2(t)}{2}\frac{5}{\pi}\left(\sin^8 \frac{\beta(t)}{2} - \cos^8 \frac{\beta(t)}{2}\right).
\end{aligned} \tag{4.43}$$

For instance, when the orbital plane is face-on ($\beta(t) = 0$), $\mathfrak{h}_{2,2}$ is counter-clockwise circularly polarized with $s_1(t) = s_2(t) = 0$ and $s_3(t) = -1$. When the orbital plane is edge-on ($\beta(t) = \pi/2$), $\mathfrak{h}_{2,2}$ is linearly polarized with $s_3(t) = 0$ (horizontal for $\alpha = 0$ and vertical for $\alpha = \pi/4$). For $0 < \beta < \pi/2$, $\mathfrak{h}_{2,2}$ is elliptically polarized.

We have a closed form expression of the instantaneous Stokes parameters of $\mathfrak{h}_{2,2}(t)$ and its instantaneous phase (which is $\varphi(t) = \varphi_{2,2}(t) - 2\gamma(t)$) with respect to the rotation parameters $(\alpha(t), \beta(t), \gamma(t))$ and the amplitude and phase of the co-precessing mode $(a_{2,2}(t), \varphi_{2,2}(t))$. The instantaneous frequency of the dominant polarized component can be computed from (1.34), such that

$$\omega(t) = \dot{\varphi}_{2,2}(t) - 2\dot{\gamma}(t) + 2\dot{\alpha}(t)\frac{\sin^8(\beta(t)/2) - \cos^8(\beta(t)/2)}{\sin^8(\beta(t)/2) + \cos^8(\beta(t)/2)}. \tag{4.44}$$

While we content ourselves to the dominant polarized component, the same straightforward derivation applies to subdominant polarized components $\mathfrak{h}_{l,m}$: the instantaneous polarization parameters and the instantaneous frequency are expressed with respect to the orientation of the line of sight and the amplitude and phase of the waveform modes in the co-processing source frame.

17: In this particular case, the expression of $\mathfrak{h}_{2,2}$ from (4.39) and (4.40) is quite simple. However we want to illustrate the appropriateness of the Stokes parameters derivation presented in the last section.

4.4 Precession induced variations of waveform polarization state

Section 4.3 shown that gravitational waves emitted by the coalescence of compact objects are a sum of non stationary polarized signals whose polarizations depend on the orientation of the line of sight with respect to the orbital plane. A variation of polarization state over time is characteristic of a precession movement of the orbital plane. This suggests a methodology for the detection of precession effects, which would consist to detect time variations of the normalized Stokes parameters/polarization state of a polarized component.

4.4.1 Sensitivity of the normalized Stokes parameters

For precessing BHHs, the instantaneous polarization state of the polarized components only depends on the triplet $(\alpha(t), \beta(t), \gamma(t))$ parametrizing the precession motion with respect to an inertial source frame, and the orientation of the observer in this frame (ι, φ_0). At a given time t, $\beta(t)$ is the opening angle between the Newtonian orbital angular momentum $\vec{L}_N(t)$ and a given reference inertial vector[18], which we defined as $\vec{L}_N(t_0)$.

18: A small variation of $\beta(t)$ corresponds to a small precession and conversely a large $\beta(t)$ corresponds to a high precession.

During the coalescence, the spins of the two objects tend to align themselves [49, 50] and thus limit the precession effects during the last stages of the coalescence, when the signal is in the observable bandwith. At this date, hints of precession are reported [36] but there is no confident detection of a precessing binary. From this status, this section considers the influence of small precession effects, i.e. small variations of $\beta(t)$, on the instantaneous Stokes parameters. The objective is to evaluate which configurations are more or less favorable to the detection of precession.

First order approximation

For each polarized component, the Taylor series of the normalized Stokes parameters with respect to the precession angle $\beta(t)$ can be computed from (4.38). In particular, this leads to

$$
\begin{aligned}
s_1(t) &= \frac{\sin^4\iota}{\sin^4\iota + 8\cos^2\iota} + 16\frac{\sin\iota\cos\iota(\cos^4\iota - 1)\cos(\varphi_0 + \alpha(t))}{(\cos^4\iota + 6\cos^2\iota + 1)^2}\beta(t) + \mathcal{O}(\beta^2(t)) \\
s_2(t) &= 4\frac{\sin^3\iota\sin(\varphi_0 + \alpha(t))}{\sin^4\iota + 8\cos^2\iota}\beta(t) + \mathcal{O}(\beta^2(t)) \\
s_3(t) &= -4\frac{\cos\iota(1 + \cos^2\iota)}{\cos^4\iota + 6\cos^2\iota + 1} - 4\frac{\sin^7\iota\cos(\varphi_0 + \alpha(t))}{(\cos^4\iota + 6\cos^2\iota + 1)^2}\beta(t) + \mathcal{O}(\beta^2(t))
\end{aligned}
\tag{4.45}
$$

for the dominant polarized component $\mathfrak{h}_{2,2}$.

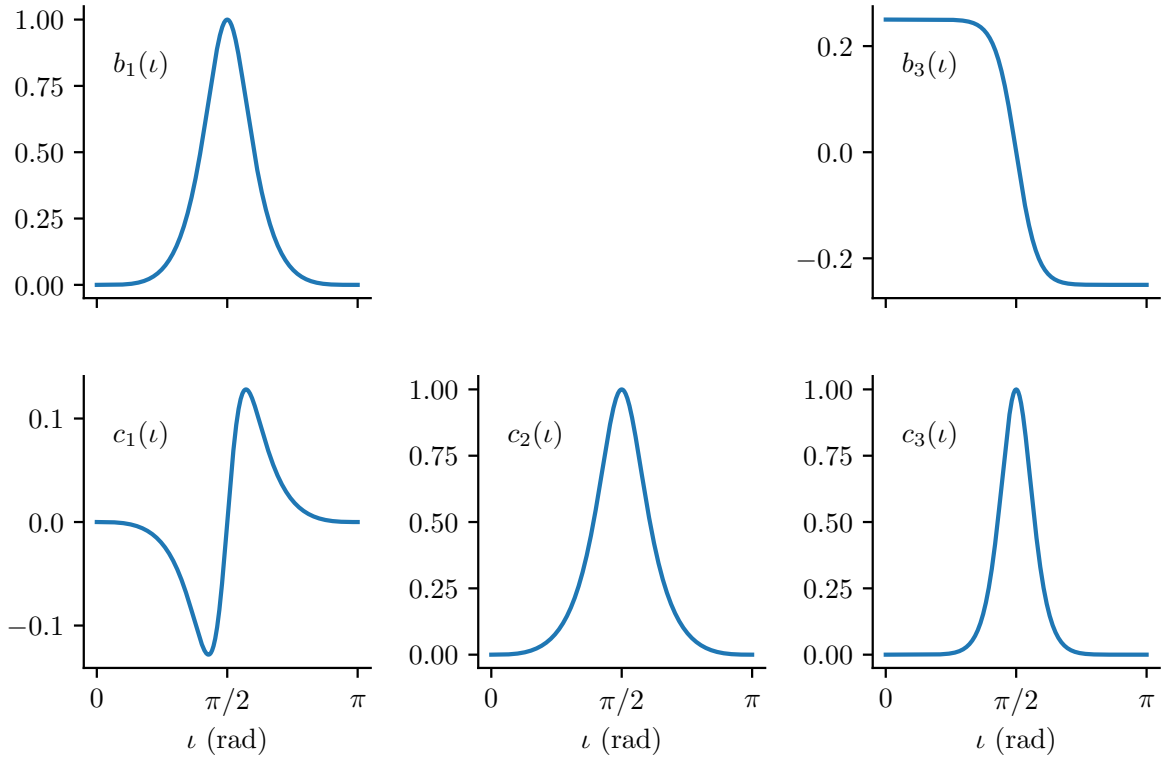

Figure 4.10: First coefficients of the expansion of the Stokes of the (2,2) precessing modes.

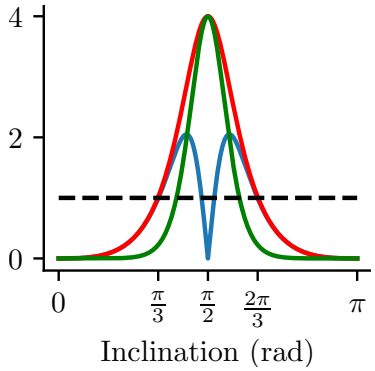

Figure 4.11: Second order coefficients of the Taylor series of the normalized Stokes parameters: (blue) $16\,|c_1(\iota)|$, (red) $4\,|c_2(\iota)|$, (green) $4\,|c_3(\iota)|$. The dashed line corresponds to a threshold value of 1.

Equation (4.45) reveals that the inclination ι is leading the dependence of the Stokes parameters with respect to $\beta(t)$. Moreover, for almost all inclinations $s_1(t), s_2(t)$ and $s_3(t)$ linearly depends on $\beta(t)$. Exceptions are notably the face-on ($\iota = 0$) and face-off ($\iota = \pi$) cases for which none of them has a linear dependence, and the edge-on ($\iota = \pi/2$) case for which the first order coefficient of $s_1(t)$ is vanishing.

In order to differentiate between the different terms of the expansions, Equation (4.45) is shortened as

$$
\begin{aligned}
s_1(t) &= b_1(\iota) + 16c_1(\iota)\cos(\varphi_0 + \alpha(t))\beta(t) + \mathcal{O}(\beta^2), \\
s_2(t) &= 4c_2(\iota)\cos(\varphi_0 + \alpha(t))\beta(t) + \mathcal{O}(\beta^2), \\
s_3(t) &= -4b_3(\iota) - 4c_3(\iota)\cos(\varphi_0 + \alpha(t))\beta(t) + \mathcal{O}(\beta^2),
\end{aligned}
\tag{4.46}
$$

where zero and first order coefficients of the normalized Stokes parameters are shown in Figure 4.10.

Without precession, the values of the normalized instantaneous Stokes parameters are given by[19] $s_1 = b_1(\iota)$, $s_2 = 0$, $s_3 = -4b_3(\iota)$. Depending on the amplitude of the first order coefficients $16\,|c_1(\iota)|$, $4\,|c_2(\iota)|$ and $4\,|c_3(\iota)|$, the normalized Stokes parameters are more or less sensitive to small variations of $\beta(t)$. The amplitude of the first order coefficients is drawn as a function of ι in Figure 4.11. For $\iota \in [\pi/3, 2\pi/3]$ (inclinations between 60 and 120 degrees), variations of $s_1(t)$, $s_2(t)$, $s_3(t)$ are of the same order as variations of $\beta(t)$ (expect for $s_1(t)$ on a small interval around $\iota = \pi/2$). Outside this interval variations of $s_1(t)$, $s_2(t)$, $s_3(t)$ are much smaller than actual variations of $\beta(t)$. The normalized Stokes parameters are thus more sensitive to variations of the orbital plane for near edge-on binaries.

One could expand (4.45) up to the second order. Doing so, we see that for $\iota = \pi/2$, none of $s_1(t)$, $s_2(t)$, $s_3(t)$ exhibit a quadratic dependence on $\beta(t)$. In the face-on and face-off cases, the second order terms of $s_2(t)$, $s_3(t)$ vanish. The approximation (4.45) is thus more accurate for near edge-on binaries.

19: Here we work in the wave source frame. That is, the polarization angle is null.

Probability distributions of Δs_1, Δs_2, Δs_3

Considering a given distribution of the line of sight in the source frame, one can predict the expected distribution of Stokes variations for the upcoming signals (4.45). This defines a goal for the accuracy of Stokes parameters estimation.

For an isotropic distribution of the line of sight, the inclination distribution is given by $g(\iota) = \sin(\iota)/2$ for $\iota \in [0, \pi]$, see Figure 4.12. Based on the difference of amplitude of the waveform for different inclinations[20], Schutz [86] estimated a distribution of detectable inclination as

$$f(\iota) = 0.076076(1 + 6\cos^2\iota + \cos^4\iota)^{\frac{3}{2}} \sin\iota, \tag{4.47}$$

see Figure 4.12.

We define $\beta_{\max}$ as the opening angle of the cone drawn by the Newtonian angular momentum $\vec{L}_N(t)$ (see Figure 3.12), i.e. the maximum precession angle of the binary. For a given

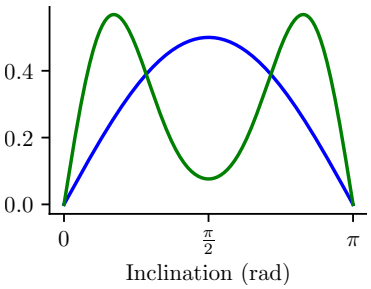

Figure 4.12: Uniform inclination (blue) and detectable inclination (green) distributions.

20: Without precession, $\beta(t)$ can be replaced by ι in (4.43). Then S_0 gives the power of the signal as a function of the inclination angle.

[86]: Schutz (2011), *Networks of gravitational wave detectors and three figures of merit*

$\beta_{\max} \ll 1$ and a given inclination ι,

$$\begin{aligned} \Delta s_1(\iota, \beta_{\max}) &= 16\,|c_1(\iota)|\,\beta_{\max} \\ \Delta s_2(\iota, \beta_{\max}) &= 4\,|c_2(\iota)|\,\beta_{\max} \\ \Delta s_3(\iota, \beta_{\max}) &= 4\,|c_3(\iota)|\,\beta_{\max} \end{aligned} \tag{4.48}$$

are the first order variations of the normalized Stokes parameters induced by a low precession of the orbital plane.

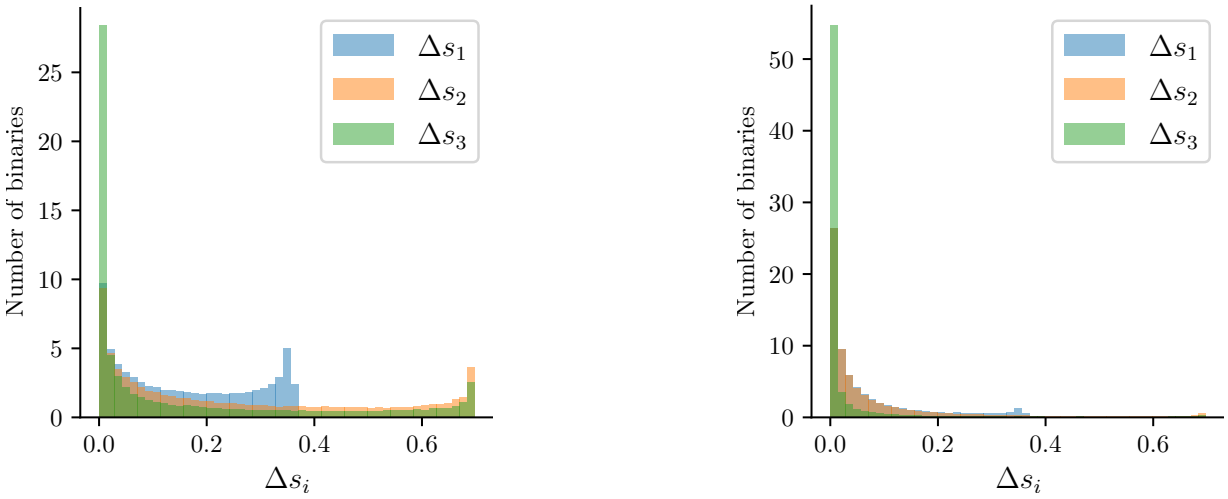

(a) **(b)**

Figure 4.13: Histogram of Δs_i for a uniform distribution of inclinations **(a)** and for a distribution of detectable inclinations **(b)**.

Table 4.2: Quantiles of the distribution of Δs_i associated to $\beta_{\max} = 5\,\text{deg}$ for the uniform distribution of inclination **(a)** and the detectable distribution of inclination **(b)**.

	$q_{5\%}$	$q_{50\%}$	$q_{95\%}$
Δs_1	2.8×10^{-3}	1.3×10^{-1}	3.5×10^{-1}
Δs_2	2.9×10^{-3}	1.7×10^{-1}	6.8×10^{-1}
Δs_3	3.8×10^{-6}	3.8×10^{-2}	6.7×10^{-1}

(a)

	$q_{5\%}$	$q_{50\%}$	$q_{95\%}$
Δs_1	4.5×10^{-4}	2.6×10^{-2}	3×10^{-1}
Δs_2	4.4×10^{-4}	2.6×10^{-2}	4.3×10^{-1}
Δs_3	5.1×10^{-8}	6.1×10^{-4}	2.6×10^{-1}

(b)

For a given $\beta_{\max}$ and a distribution of inclination ($g(\iota)$ or $f(\iota)$), we draw the distribution of Δs_1, Δs_2 and Δs_3. The results are illustrated in Figure 4.13 for $\beta_{\max} = 5\,\text{deg}$. The quantiles of the Δs_i are given in Table 4.2. For a precession angle of 5 deg, the maximum value of Δs_i are given by $4\beta_{\max} \approx 0.34$ for s_2 and s_3. Considering the uniform distribution, this means that for half of the binaries $\Delta s_2 \in [0.17, 0.34]$ and $\Delta s_3 \in [0.038, 0.34]$. It goes to $\Delta s_2 \in [0.026, 0.34]$ and $\Delta s_3 \in [6.1 \times 10^{-4}, 0.34]$ for detectable binaries.

Δs_1, Δs_2 and Δs_3 are figures of merit for the detection of low precession in the detector network observations. They define the sensitivity that a method detecting precession

should have with respect to the inclination of a binary and the precession level.

4.4.2 Towards the detection of precession

Section 4.4.1 introduced Δs_1, Δs_2 and Δs_3 as characterizing the level of variation of the normalized Stokes parameters depending on the inclination and precession angle. This suggests a strategy for the detection of precession which consists to detect two distinct polarization states at different instants in the signal observations. For example by comparing gains of Hermitian filters [3] with distinct polarization axes. As a first step, this proposed approach supposes to detect the polarization state of the signal in noisy data.

The polarization SNR

In order to measure the detectability of the polarization state of a given gravitational waveform, we propose a polarization SNR as the power spectral density of the filtered signal, with a whitening and unpolarizing filter as defined by Flamant [3]. The polarization SNR writes

$$\rho_{\text{polar}} = \int \left|\tilde{H}(\omega)\right|^2 \mathrm{d}\omega \tag{4.49}$$

where $H(\omega) \in \mathbb{H}$ is the quaternion Fourier transform of the waveform h, and

$$\tilde{H}(\omega) = K(\omega)\left(H(\omega) + \eta(\omega)\boldsymbol{\mu}_n(\omega)H(\omega)\boldsymbol{j}\right) \tag{4.50}$$

is its filtered version with a quaternion Hermitian filter [3] corresponding to statistical properties of the noise. The polarizing power of the filter is such that

$$\eta(\omega) = \frac{1 - \sqrt{1 - \Phi_n^2(\omega)}}{\Phi_n^2(\omega)} \tag{4.51}$$

where $\Phi_n(\omega)$ is the polarization degree of the noise at frequency ω. $\boldsymbol{\mu}_n(\omega)$ is the noise main polarization axis and the homogenous gain is

$$K^2(\omega) = \frac{1}{2S_{0,n}(\omega)} \frac{\Phi_n^2(\omega)}{\left(1 - \Phi_n^2(\omega)\right)\left(1 - \sqrt{1 - \Phi_n^2(\omega)}\right)} \tag{4.52}$$

where $S_{0,n}(\omega)$ is the power spectral density of the noise.

ρ_{polar} measures the detectability of the polarization state of a signal in an additive Gaussian noise. It depends on the ratio between the signal energy and the noise power spectral density and on the correlation between the noise and signal polarization axis [3].

A precession SNR

For a signal with a sufficient polarization SNR, one expect to detect variations of the polarization state. As for compact binaries, the polarization state of the gravitational-wave signal is determined by the orientation of the orbital plane. Detect a variation of polarization state remains to detect precession effects in the gravitational waveform. To do so, we compute a dominant polarization axis as the polarization axis which maximizes the energy of the output of a polarizer, such that

$$\hat{\boldsymbol{\mu}} = \arg\max_{\mu} \int \left| h_{\mathbb{H}}(t) + \boldsymbol{\mu} h_{\mathbb{H}}(t) \boldsymbol{j} \right|^2 \mathrm{d}t, \tag{4.53}$$

where $h_{\mathbb{H}}$ is the quaternion embedding of h, and define the precession SNR as

$$\rho_p = \int \left| \tilde{h}_{\mathbb{H}\,-\hat{\boldsymbol{\mu}}}(t) \right|^2 \mathrm{d}t, \tag{4.54}$$

where

$$h_{\mathbb{H}\,-\hat{\boldsymbol{\mu}}}(t) = h_{\mathbb{H}}(t) + \hat{\boldsymbol{\mu}} h_{\mathbb{H}}(t) \boldsymbol{j} \tag{4.55}$$

is the output of a polarizer of axis $-\hat{\boldsymbol{\mu}}$ and $\tilde{h}_{\mathbb{H}\,-\hat{\boldsymbol{\mu}}}(t)$ is defined as in (4.50) with respect to noise properties.

ρ_p measures the energy of h that corresponds to polarization states distinct from $\hat{\boldsymbol{\mu}}$. For a given signal with a fixed polarization axis over time $\boldsymbol{\mu}_h$, $\hat{\boldsymbol{\mu}} = \boldsymbol{\mu}_h$ and thus $\rho_p = 0$, whereas $\rho_p > 0$ for a signal with a varying polarization axis.

A polarization stability measure

In order to quantify the variability of the polarization of a given deterministic signal h, we define a polarization stability measure as

$$0 \leqslant D_h = 1 - \Phi_h \leqslant 1, \tag{4.56}$$

where

$$\Phi_h = \frac{\sqrt{\mathcal{S}_1{}^2 + \mathcal{S}_2{}^2 + \mathcal{S}_3{}^2}}{\mathcal{S}_0} \tag{4.57}$$

is the deterministic version of the polarization degree for stochastic processes and $\mathcal{S}_i = \int S_i(t)\mathrm{d}t$ are the averaged Stokes parameters of h. One can compute the polarization stability measure as

$$D_h = 1 - \frac{\left|\int h_{\mathbb{H}}(t) h_{\mathbb{H}}(t)^{*j}\mathrm{d}t\right|}{\int |h_{\mathbb{H}}(t)|^2\,\mathrm{d}t}. \tag{4.58}$$

D_h is a measure of stability of the polarization axis of h. For a given signal h with a fixed polarization axis $\boldsymbol{\mu} = (s_1, s_2, s_3)$, we have $\mathcal{S}_i = s_i \mathcal{S}_0$ for $i = 1, 2, 3$ and then $D_h = 0$. Conversely, for signals with a constant energy S_0 in a given interval $[1, T]$ and such that $\boldsymbol{\mu}(t) = (\cos(\alpha t), \sin(\alpha t), 0)$ with a constant angular velocity α, we have $D_h = 1$. For precessing binaries D_h quantifies the level of polarization modulations induced by precession for a given waveform.

4.5 Summary

Gravitational-wave reconstruction require the resolution of an ill-posed inverse problem. This results from the bad conditioning of the mixing matrix, as from the noise properties. A regularization method is proposed for the reconstruction of non stationary polarized signals. Based on a polarization prior, the reconstruction problem is penalized by the energy of the signal on a given polarization axis. The proposed regularization is a weak polarization constraint which allows for weakly modelled reconstruction of gravitational-wave signals. A refined method is proposed with a structured sparsity prior selecting time-frequency clusters with a physical prior. The proposed reconstruction methods are implemented and evaluated on realistic synthetic data.

While the polarization state of the dominant precessing modes $(2, \pm 2)$ was first computed by Flamant [7], we demonstrate as a more general result that gravitational waveforms are a sum of AM-FM-PM components $\mathfrak{h}_{l,m}$ with different instantaneous frequencies. The instantaneous Stokes parameters and the instantaneous frequency of the polarized components are derived. We found that the instantaneous polarization state of a polarized component is determined by

the orientation of the orbital plane compared to the observer. Thus a variation of the instantaneous polarization state of the waveform is characteristic of a precession of the orbital plane.

The main assumption on the gravitational waveform is that the conjugate symmetry must hold ; this is true for a range of sources [87]. Efforts are made by the data analysis community to move data analysis pipelines in the time-frequency domain [88] and these results can be particularly important for waveform modelling. As a perspective, the decomposition of gravitational waveforms in polarized components could be generalized to gravitational theories alternative from general relativity, which may result in additional polarizations (up to 6 polarization modes).

[87]: Thompson et al. (2020), *Modeling the gravitational wave signature of neutron star black hole coalescences*

[88]: Cornish (2020), *Time-frequency analysis of gravitational wave data*

For compact star mergers, the sensitivity of the normalized Stokes parameters with respect to a variation of inclination of the orbital plane is characterized. For an opening angle of the cone drawn by the Newtonian orbital angular momentum $\beta_{\max} = 5\,\mathrm{deg}$, we computed a distribution of the deviation of the normalized Stokes parameters Δs_i for two different population of binaries. Finally, different quantities are introduced: the polarization SNR ρ_{polar}, which is a contrast measure between the signal and noise polarizations ponderated by their respective energies ; the precession SNR ρ_p, which measures the detectability of polarization modulations ; the polarization stability measure D_h, which depends on the variation of the instantaneous polarization of a given signal h. In particular the precession SNR can be used as a detection statistics for precession effects.

Conclusion and perspectives

The field of polarimetric analysis of non stationary bivariate signals is in its infancy. It still essentially relies and borrows from the techniques developed for the univariate signals, applied trivially to each component separately, and thus missing the important geometrical information shared by the two. This field has recently regain interest with the successful application of polarimetric analysis over different contexts, e.g. oceanography [8] and gravitational wave analysis [72].

Flamant introduced a quaternion formalism [3] based in an embedding of a complex-valued signals in a four dimensional space. Each of the signal variables are analysed in two separate dimensions, and the polarimetric analysis methods derive from quaternion calculus. On the other hand, the approach of Lilly is more conventional [10, 12]. It lies in a vectorial representation of bivariate signals from which the same methods can be derived. The latter leads to less straightforward calculations but it remains adapted to multivariate signals with more than two variables.

This thesis connects the previous work of Flamant [7] and that of Lilly [10, 12] on the representation problem of oscillating and non stationary bivariate signals. Chapter 1 reviewed representations of non stationary polarized signals throughout the quaternion formalism introduced in [7]. It is shown that contrarily to what suggested Lilly and Flamant, the Euler angle parametrization of a bivariate signal is indeed well suited in a synthesis scheme, but it is not generally the case in an analysis scheme. A parametrization is proposed, defined with time-frequency observables, namely the instantaneous Stokes parameters and the instantaneous frequency.

This initial work was motivated by the main application presented in this thesis, i.e. gravitational-wave data analysis. Gravitational wave astronomy is a new field which has significantly benefited from the development of dedicated mathematical and signal processing tools [89, 90]. This thesis follows this line of research, with a focus on the not still developed polarimetric analysis of gravitational waves. The technical limitations encountered for this type of study are about to disappear with the extension of the network of second generation detectors spreading around the globe.

Based on a judicious choice of representation, generative machine learning models of gravitational waveforms are built in order to shorten estimation time of compact binary parameters. A model is proposed for both spin-aligned and precessing black hole binaries. They both are evaluated on EOB waveforms [21]. While the proposed generative model shows operational results for current and future observations of spin-aligned binaries, technical difficulties prevented the proper evaluation of the model for precessing binaries.

A new regularization method based on a polarization prior is introduced in the resolution scheme of the reconstruction denoising problem of a signal embedded in an additive Gaussian noise. The proposed regularization method is found to be more versatile than existing methodologies [41]. An application is shown on realistic synthetic data.

The observation and characterization of precessing binaries is one of the interesting challenges in gravitational-wave data analysis. These sources are of particular interest regarding the developments made in Chapter 1. As described in Chapter 4, they produce a signal which is a sum of waveforms whose amplitude, frequency and polarization are modulated over time. The instantaneous Stokes parameters and instantaneous frequency of the polarized components are expressed as a function of the amplitude and phase of co-precessing modes and rotation parameters describing the precession of the orbital plane.

The dependence of the normalized instantaneous Stokes parameters with respect to the precession angle is characterized. It is shown that in the case of low precession angles, the normalized instantaneous Stokes parameters linearly depend on this angle. Regarding a distribution of compact binary inclinations, a distribution of first order variations of the normalized instantaneous Stokes parameters is drawn. Indicators on the intrinsic and detectable level of polarization modulations of a generic bivariate signal are introduced, paving the way towards the non modelled or poorly modelled detection of precession.

This work introduces a number of mathematical tools that can be hopefully usefull for the future of gravitational-wave astronomy. The availability of additional detectors, in particular KAGRA in Japan and LIGO India, will be a game changer for this question. Within this scope, several developments can be foreseen. The most straightforward possible development is the construction of a generative model in the case of precessing black hole binaries. Technical limitations encountered in this work can be overcome by using more computing power for the training and evaluation of the model. The waveform attributes can be computed without the need to implement a Hilbert transform, using expressions of the waveform parameters given in Chapter 4. The model could be constructed in the spectral domain as in the time-frequency/wavelet domain with a stationary phase approximation. Secondly, the proposed polarization targeting prior can be included in data analysis pipeline which already uses the same inverse problem approach. Another important line of work is the use and evaluation of the polarization SNR and precession SNR for actual and future observations. From the perspective of waveform approximants, Chapter 1 and 4 suggest to synthesize the waveform modes as AM-FM-PM signals. So far, the waveform modes are modelled as AM-FM signals and thus waveform approximants focus on the computation (in time or frequency domain) of the modes' amplitude and phase possibly modulated by the effect of orbital precession. For precessing binaries, the computed amplitudes and phases are not interpretable and highly oscillating (e.g. as in Figure 1.8). Modelling the modes as AM-FM-PM signals would remain to compute the (more regular) amplitude, orientation, ellipticity and phase of the Euler angle representation. Such change of consideration would lead to a major evolution in the standard way of thinking about gravitational-wave signals.

Beyond gravitational-wave astronomy, the presented methodological work is of general purpose and is a contribution to the newly introduced field of non stationary bivariate signals analysis. It raises several questions that are left for future work. For instance, starting from the work of Brosseau [1] on the polarimetric analysis of stochastic signals, is there a proper manner to directly detect/estimate the polarization state of a non stationary signal from noisy observations without having to estimate the signal at first? For a given

application, one might be interested in estimating the instantaneous parameters of the Euler angle parametrization even if the signal goes through circular polarization states. This raises the question of the structure that should be imposed on the instantaneous orientation and instantaneous phase of the signal, and under which conditions they can be retrieved. A question that emerges concerns the decomposition of non stationary bivariate signals on a system of "basic" polarized waveforms. A mathematically motivated decomposition of any bivariate signal as a sum of polarized atoms (more general than the decomposition in rotatory components of Section 1.3.1) would impact a range of applications. By analogy with the chirplet transform [91] which generalizes the classic wavelet transform [92] with chirp-like atoms (chirplets), is it possible to build a transform which decomposes a bivariate signal on a system of (non uniformly) polarized atoms? Besides the direct implications of such transform (e.g. reconstruction and synthesis of polarized signals), this would lead to a deeper comprehension of the nature of non-stationary polarized signals.

A The quaternion formalism

A.1 Quaternions

Quaternions form a generalisation of complex numbers in four dimensions. The set of quaternions $\mathbb{H}$ forms an algebra over the real numbers. The main difference with complex numbers is that multiplication is associative but non-commutative. Similarly to complex numbers, a quaternion $q \in \mathbb{H}$ has a unique cartesian expression

$$q = a + \boldsymbol{i}b + \boldsymbol{j}c + \boldsymbol{k}d, \tag{A.1}$$

with $a, b, c, d \in \mathbb{R}$ and $\boldsymbol{i}, \boldsymbol{j}, \boldsymbol{k}$ three distinct roots of -1. The cartesian form (A.1) allows to define the addition in a simple way. For a given quaternion $p = e + \boldsymbol{i}f + \boldsymbol{j}g + \boldsymbol{k}h$, the addition $p + q$ gives

$$p + q = (a + e) + \boldsymbol{i}(b + f) + \boldsymbol{j}(c + g) + \boldsymbol{k}(d + h).$$

Multiplication rules for the three imaginary units define cyclic relations. They read

$$\begin{aligned} \boldsymbol{i}^2 = \boldsymbol{j}^2 = \boldsymbol{k}^2 &= -1, \\ \boldsymbol{i}\boldsymbol{j} = -\boldsymbol{j}\boldsymbol{i} &= \boldsymbol{k}, \\ \boldsymbol{k}\boldsymbol{i} = -\boldsymbol{i}\boldsymbol{k} &= \boldsymbol{j}, \\ \boldsymbol{j}\boldsymbol{k} = -\boldsymbol{k}\boldsymbol{j} &= \boldsymbol{i}. \end{aligned} \tag{A.2}$$

Thanks to the distributivity of multiplication, (A.2) directly gives the following results for the multiplication of p and q

$$\begin{aligned} qp = ae - (bf + cg + dh) + a(\boldsymbol{i}f + \boldsymbol{j}g + \boldsymbol{k}h) + e(\boldsymbol{i}b + \boldsymbol{j}c + \boldsymbol{k}d) \\ + \boldsymbol{i}(ch - dg) + \boldsymbol{j}(df - bh) + \boldsymbol{k}(bg - cf). \end{aligned} \tag{A.3}$$

The non-commutativity of quaternion product, which is evident from (A.3), comes from multiplication rules (A.2). Thus in general

$$qp \neq pq.$$

Due to the non-commutativity of the product, the position of each element is important in the definition of quaternionic operators. For example, position of the exponential and imaginary component $\boldsymbol{j}$ in the quaternion Fourier and Hilbert

Definions of this section are taken from [13]. One may refer to [93] for a deeper introduction on the subject.

[93]: Altmann (2005), *Rotations, quaternions, and double groups; Corrected ed.*

transforms are important. In an analogous way to complex numbers, for q defined in (A.1), a denotes its real part and $\boldsymbol{i}b + \boldsymbol{j}c + \boldsymbol{k}d$ its imaginary part. Thus the conjugate of q is

$$\bar{q} = a - \boldsymbol{i}b - \boldsymbol{j}c - \boldsymbol{k}d.$$

The modulus of a quaternion is as expected

$$|q| = \sqrt{q\bar{q}} = \sqrt{a^2 + b^2 + c^2 + d^2}.$$

q is a unit quaternion if $|q| = 1$. It is a pure unit quaternion if and only if $q^2 = -1$.
An involution by a pure unit quaternion $\boldsymbol{\mu}$ is defined as

$$\bar{q}^{\mu} = \bar{\boldsymbol{\mu}} q \boldsymbol{\mu}.$$

In this manuscript we mainly use the combination of a conjugation and a canonical involution of axis $\boldsymbol{j}$

$$q^{*j} = \overline{\bar{q}^j} = \overline{\bar{q}}^j = a + \boldsymbol{i}b - \boldsymbol{j}c + \boldsymbol{k}d.$$

In particular, one directly has

$$\overline{qp} = \bar{p}\bar{q} \text{ and } \overline{qp}^j = \bar{q}^j \bar{p}^j.$$

One may verify that its inverse is

$$q^{-1} = \frac{\overline{q}}{|q|^2}.$$

The widely used quaternion exponential is defined, as for real numbers, as a series expansion

$$e^q = \sum_{n=0}^{\infty} \frac{q^n}{n!}. \tag{A.4}$$

A direct calculation shows that $e^q = e^a e^{\boldsymbol{i}b+\boldsymbol{j}c+\boldsymbol{k}d} = e^a \left(\sum_{n=0}^{\infty} \frac{\mathrm{Im}\{q\}^n}{n!} \right)$, where we denoted the imaginary part $\mathrm{Im}\{q\} = \boldsymbol{i}b + \boldsymbol{j}c + \boldsymbol{k}d$. Then one show that $e^q = e^a \left(\cos|\mathrm{Im}\{q\}| + \widetilde{\mathrm{Im}\{q\}} \sin|\mathrm{Im}\{q\}| \right)$ with $\mathrm{Im}\{q\} = |\mathrm{Im}\{q\}| \widetilde{\mathrm{Im}\{q\}}$ and $\widetilde{\mathrm{Im}\{q\}} = \mathrm{Im}\{q\} / |\mathrm{Im}\{q\}|$. In the particular case of pure unit quaternion $\boldsymbol{\mu}$ i.e. a quaternion without real part and with modulus equal to 1, and a given real value ϕ, then

$$e^{\phi\boldsymbol{\mu}} = \cos\phi + \boldsymbol{\mu}\sin\phi. \tag{A.5}$$

Thus Equation (A.5) is in particular valid for $\boldsymbol{\mu} = \boldsymbol{i}, \boldsymbol{j}$ and $\boldsymbol{k}$.

The logarithm of a quaternion is defined such that

$$\ln(q) = \ln|q| + \frac{\mathrm{Im}\{q\}}{|\mathrm{Im}\{q\}|} \arccos \frac{\mathrm{Re}\{q\}}{|q|}. \tag{A.6}$$

There are several decompositions of quaternion: cartesian form (A.1) is only one of the symplectic forms, while polar forms derive from Equation (A.5).

A.2 Quaternion spectral analysis

The quaternionic analysis of polarized bivariate signals is based on a recent formalism proposed by Flamant [3]. This formalism uses frequency and time-frequency analysis techniques on the space of quaternions to study spectral and time-frequency polarization properties of bivariate signals. Since the notion of polarization is linked to the notion of cycle when scanning an ellipse, spectral analysis is a keystone in the analysis of polarized signals.

The definition of a quaternion Fourier transform (QFT) is a basis for our analysis of bivariate signals[1]. There are several equivalent ways to define the quaternionic Fourier transform because of the non commutativity of the product in $\mathbb{H}$. This requires to differentiate the transformation with exponential on the right-hand side from the one with exponential on the left. The axis of the transformation is also a degree of freedom and we follow here the convention used in the work of Flamant [3].

Definition A.2.1 (Quaternion Fourier transform) *We define the quaternion Fourier transform (of axis $\boldsymbol{j}$) as the linear application which associates to $f \in L^2(\mathbb{R}, \mathbb{H})$*

$$\mathcal{F}\{f\}(\omega) = \frac{1}{\sqrt{2\pi}} \int f(t) e^{-j\omega t} \mathrm{d}t \quad \forall \omega \in \mathbb{R} \tag{A.7}$$

and we denote $\mathcal{F}\{f\} = \hat{f} \in L^2(\mathbb{R}, \mathbb{H})$.

As in the complex case we can demonstrate the existence of an inverse for the QFT, with $f(t) = \frac{1}{\sqrt{2\pi}} \int \mathcal{F}\{f\}(\omega) e^{j\omega t} \mathrm{d}\omega$

1: The construction of the quaternionic Fourier transform on the Hilbert space $L^2(\mathbb{R}, \mathbb{H})$ is similar to the construction of the classic Fourier transform on $L^2(\mathbb{R}, \mathbb{C})$. One can find such a construction in [94].

[94]: Jamison (1970), *Extension of some theorems of complex functional analysis to linear spaces over the quaternions and Cayley numbers*

as well as other properties like the Parseval-Plancherel identities

$$\int |f(t)|^2 \, \mathrm{d}t = \int |\mathcal{F}\{f\}(\omega)|^2 \mathrm{d}\omega, \tag{A.8}$$

$$\int f(t) f(t)^{*j} \mathrm{d}t = \int \mathcal{F}\{f\}(\omega) \mathcal{F}\{f\}(\omega)^{*j} \mathrm{d}\omega. \tag{A.9}$$

It follows that $|\mathcal{F}\{f\}(\omega)|^2$ and $\mathcal{F}\{f\}(\omega)\mathcal{F}\{f\}(\omega)^{*j}$ can be seen as spectral domain densities.

An important point for the analysis of bivariate signals is the $\boldsymbol{i}$-Hermitian symmetry[2]: for all $f \in L^2(\mathbb{R}, \mathbb{H})$ such that $f(t) \in \mathbb{C}_{\boldsymbol{i}}$ we have

$$\mathcal{F}\{f\}(-\omega) = \overline{\mathcal{F}\{f\}(\omega)}^{\boldsymbol{i}} \quad \forall \omega \in \mathbb{R}. \tag{A.10}$$

2: This justifies the choice of $\boldsymbol{j}$ as the axis of the QFT (it is sufficient to choose an axis orthogonal to $\boldsymbol{i}$).

The $\boldsymbol{i}$-Hermitian symmetry implies that the information carried by the negative frequencies is redundant, the signal can be described only with its positive frequencies. In this way, we associate to a signal its counterpart made up only of positive frequencies.

The spectral Stokes parameters are defined as

$$\begin{aligned} |\mathcal{F}\{f\}(\omega)|^2 &= S_0(\omega), \\ \mathcal{F}\{f\}(\omega)\mathcal{F}\{f\}(\omega)^{*j} &= S_1(\omega) + \boldsymbol{i} S_2(\omega) - \boldsymbol{k} S_3(\omega). \end{aligned} \tag{A.11}$$

They are the energetic and geometric content preserved by the quaternion Fourier transform. While $S_0(\omega)$ is the energy of the two components at frequency ω: $S_0(\omega) = |X(\omega)|^2 + |Y(\omega)|^2$, the other Stokes parameters are constructed with cross-correlation products:

$$\begin{aligned} S_1(\omega) &= |X(\omega)|^2 - |Y(\omega)|^2 , \\ S_2(\omega) &= 2\left(\mathrm{Re}\{X(\omega)\}\,\mathrm{Re}\{Y(\omega)\} + \mathrm{Im}\{X(\omega)\}\,\mathrm{Im}\{Y(\omega)\}\right), \\ S_3(\omega) &= 2\left(\mathrm{Im}\{X(\omega)\}\,\mathrm{Re}\{Y(\omega)\} - \mathrm{Re}\{X(\omega)\}\,\mathrm{Im}\{Y(\omega)\}\right). \end{aligned}$$

The invocation of quaternions is motivated by the fact that polarization is revealed by correlation of signal components, thus in the first time it becomes necessary to apply a spectral analysis of each component separately. Classical methods such as the complex Fourier transform mix the two dimensions of a complex-valued signal, whereas quaternions allow us to construct a Fourier transform that analyzes them separately and brings out their relationships in a natural way. This is because they allow to associate two different axes to the frequency representation of each signal component. A

bivariate signal of the form $z(t) = x(t) + \boldsymbol{i}y(t)$ has its first component $x(t)$ analysed on axes $\{\mathbf{1}, \boldsymbol{j}\}$ while its second component $y(t)$ is analysed on $\{\boldsymbol{i}, \boldsymbol{k}\}$. A fortiori the number of dimension is equal to the number of degree of freedom for polarized signals. A deeper discussion of these aspects can be found in [3] .

A.3 Discrete quaternion embedding

We considered so far continuous-time signals, building fundations on which we rely to analyse finite discrete time signals. A major concern when estimating the instantaneous parameters of a bivariate discrete-time signal is the discrete Hilbert transform and the discrete computation of the quaternion embedding. For infinite duration signals, problems arise from the impossibility to process all the signal at once. For finite duration signals, the periodicity of the discrete-time quaternion Fourier transform prevents to define a signal with strictly zero negative frequencies. Instead we consider a quaternion embedding-like signal with the idea of removing redundancy of the negative frequencies in each spectral period. These considerations are well discussed in the signal processing litterature in the context of discrete real-valued signals and the associated analytic-like signals [15][95, 96]. Section 1.2.2 introduced the continuous Hilbert transform as an ideal filter of frequency response $-\boldsymbol{j}\sin\omega$ which is used in order to compute the quaternion embedding $z_{\mathbb{H}}$. This filter should be approximated for digital applications.

[95]: Oppenheim et al. (2009), *Discrete-Time Signal Processing*
[96]: Reilly et al. (1994), *Analytic signal generation-tips and traps*

Finite duration signals Let us assume that $z[n] = x[n] + \boldsymbol{i}y[n]$ is a sampled version of a band-limited continuous-time bivariate signal i.e. $z[n] = z(nT)$ with $T \in \mathbb{R}_+$ the sampling interval in seconds and $n \in \{0, \ldots, N-1\}$. We suppose that the continuous-time signal has been low-pass filtered or T has been chosen (zero padding) so that there is no aliasing and apply the same derivation for finite duration discrete-time bivariate signals as the one used in section 1.2.2. The discrete-time quaternionic Fourier transform of $z[n]$

$$Z[m] = \sum_{n=0}^{N-1} z[n] e^{-2\pi \boldsymbol{j} mnT}$$

exhibits a periodic structure such as in the discrete real-valued case[3]. It is convenient that the discrete quaternion

3: See Figure 1 of [15] for example. This came from the definition of the discrete quaternion Fourier transform which derives from a discretization of the quaternion Fourier transform of periodic signals.

embedding $z_{\mathbb{H}}[n]$ fulfils basic properties that its continuous version verifies. For instance, the fact that its projection on $\mathbb{C}_{\boldsymbol{i}}$ gives back the original analyzed signal: $P_{\mathbb{C}_i}\left\{z_{\mathbb{H}}\right\}[n] = z[n]$. Also, by definition of the continuous Hilbert transform $\mathscr{H}$ as a filter of frequency response $-\boldsymbol{j}\,\mathrm{sign}(\omega)$, the $\boldsymbol{i}$-Hermitian symmetry implies that: $\langle z, \mathscr{H}\{z\}\rangle_{\mathbb{H}} = 0$. This derives from simple manipulations noting that

$$\begin{aligned}
\int z(t)\overline{\mathscr{H}\{z\}(t)}\mathrm{d}t &= \int Z(\omega)\overline{(-\boldsymbol{j}\,\mathrm{sign}(\omega)Z(\omega))}\mathrm{d}\omega \\
&= -\int_{\mathbb{R}_+} Z(\omega)\overline{(\omega)}\mathrm{d}\omega + \int_{\mathbb{R}_+} \overline{\hat{z}(\omega)}^{\boldsymbol{i}}\boldsymbol{j}\overline{Z(\omega)}^{\boldsymbol{i}}\,\mathrm{d}\omega \\
&= \int_{\mathbb{R}_+} |Z(\omega)|^2\,\boldsymbol{j}\mathrm{d}\omega - \int_{\mathbb{R}_+} |Z(\omega)|^2\,\boldsymbol{j}\mathrm{d}\omega \\
&= 0.
\end{aligned}$$

Similarly to what Marple showed for real-valued signals [15], (if N is even) the discrete quaternion embedding should be defined as the signal such that

$$Z_{\mathbb{H}}[m] = \begin{cases} Z[m], & \text{for } m = 0 \text{ and } m = N/2. \\ 2Z[m], & \text{for } 1 \leqslant m \leqslant N/2 - 1. \\ 0, & \text{for for } 1N/2 + 1 \leqslant m \leqslant N - 1. \end{cases}$$

This definition implies that the two previous conditions are satisfied: $\mathbb{C}_{\boldsymbol{i}}$-projection and orthogonality conditions. The special coefficient applied to the null and Nyquist frequency ($m = 0$ and $m = N/2$ respectively) terms are motivated by the periodicity of the discrete Fourier transform which involves that those are shared between the negative and positive frequency halves of the periodic spectrum. Usual discrete Fourier transform considerations appear in the usage of the quaternion embedding: aliasing can be limited by filtering or zero padding and the signal should be periodic. If these conditions are not satisfied the estimated instantaneous parameters $\left[\hat{a}[n],\ \hat{\theta}[n],\ \hat{\chi}[n],\ \hat{\varphi}[n]\right]$ (see Section 1.2.2) exhibit artificial oscillations. These oscillations are notably important because they are added to the instrumental gimbal lock.

Infinite duration signals The case of infinite duration discrete signals is beyond the scope of this work. Since the classical results for real-valued signals analysis applied for the quaternion Hilbert transform, we restrict ourselves to a brief conclusion of the given references [95, 96]. For infinite duration signal the previous approach is not relevant because

the signal should be truncated on finite time intervals. This may cause aliasing if the size of the window (time intervals) is not well chosen. In addition the signal will not be periodic in each window. Such procedure may construct strongly biased approximation of the quaternion embedding. Oppenheim and Schafer [95] present several possible real-valued Finite Impulse Response (FIR) filters in order to approximate the ideal Hilbert filter impulse response

$$h[n] = \begin{cases} 0, & \text{for } n = 0. \\ 2\sin(n\pi/2)/n\pi, & \text{for } n \neq 0. \end{cases}$$

Reilly an Frazer [96] have shown that a complex filter (which transposes into a quaternion $\boldsymbol{j}$-filter in our case) have better properties than real-valued ones. It is constructed with a low pass filter that cut at $f_s/4$ (where f_s is the sampling frequency) which is modulated by a complex exponential (quaternion exponential in our case) in order for the stop band to cover the whole negative frequency spectrum. In contrast to real-valued filters, in this approach the original signal $z[n]$ is alterated by filtering, thus the projection of $z_{\mathbb{H}}[n]$ on $\mathbb{C}_{\boldsymbol{i}}$ is different from $z[n]$ (but the orthogonality property between z and $\mathcal{H}\{z\}$ holds).

A.4 Instantaneous frequency of an AM-FM-PM signal

The computation of the first instantaneous moment of the energy density, i.e. the instantaneous frequency, is done from its definition in Equation (1.30). One develops the left side of (1.30) using the differentiation property of the Fourier transform, i.e. $\mathcal{F}\left\{\dot{f}\right\}(\omega) = \omega F(\omega)\boldsymbol{j}$, and the Parceval-Plancherel identity (A.9), such as

$$\begin{aligned} \int \omega \left|Z_{\mathbb{H}}(\omega)\right|^2 \mathrm{d}\omega &= \int \omega Z_{\mathbb{H}}(\omega)\overline{Z_{\mathbb{H}}(\omega)}\mathrm{d}\omega \\ &= \int \mathcal{F}\left\{\dot{z}_{\mathbb{H}}\right\}(\omega)\boldsymbol{j}^{-1}\overline{Z_{\mathbb{H}}(\omega)}\mathrm{d}\omega \\ &= \int \dot{z}_{\mathbb{H}}(t)\boldsymbol{j}^{-1}\overline{z_{\mathbb{H}}(t)}\mathrm{d}t \\ &= \int \dot{z}_{\mathbb{H}}(t)\boldsymbol{j}^{-1}\left(z_{\mathbb{H}}(t)\right)^{-1}\left|z_{\mathbb{H}}(t)\right|^2 \mathrm{d}t. \end{aligned} \tag{A.12}$$

Then $\omega_z(t)$ is deduced from (A.12) by

$$
\begin{aligned}
\omega_z(t) =& \mathrm{Re}\left\{\dot{z}_{\mathbb{H}}(t)\boldsymbol{j}^{-1}\left(z_{\mathbb{H}}(t)\right)^{-1}\right\} \\
=& \mathrm{Re}\Big\{\Big(\dot{a}(t)e^{\boldsymbol{i}\theta(t)}e^{-\boldsymbol{k}\chi(t)}e^{\boldsymbol{j}\varphi(t)} + a(t)\boldsymbol{i}\dot{a}(t)e^{\boldsymbol{i}\theta(t)}e^{-\boldsymbol{k}\chi(t)}e^{\boldsymbol{j}\varphi(t)} \\
&+ a(t)e^{\boldsymbol{i}\theta(t)}\boldsymbol{k}^{-1}\dot{\chi}(t)e^{-\boldsymbol{k}\chi(t)}e^{\boldsymbol{j}\varphi(t)} + a(t)e^{\boldsymbol{i}\theta(t)}e^{-\boldsymbol{k}\chi(t)}\boldsymbol{j}\dot{\varphi}(t)e^{\boldsymbol{j}\varphi(t)}\Big) \\
&\times \boldsymbol{j}^{-1}a^{-1}(t)e^{-\boldsymbol{j}\varphi(t)}e^{\boldsymbol{k}\chi(t)}e^{-\theta(t)}\Big\} \\
=& \mathrm{Re}\Big\{\frac{\dot{a}(t)}{a(t)}e^{\boldsymbol{i}\theta(t)}e^{-\boldsymbol{k}\chi(t)}\boldsymbol{j}^{-1}e^{\boldsymbol{k}\chi(t)}e^{-\boldsymbol{i}\theta(t)} + \boldsymbol{i}\dot{a}(t)e^{\boldsymbol{i}\theta(t)}e^{-\boldsymbol{k}\chi(t)}\boldsymbol{j}^{-1}e^{\boldsymbol{k}\chi(t)}e^{-\boldsymbol{i}\theta(t)} \\
&+ e^{\boldsymbol{i}\theta(t)}\boldsymbol{k}^{-1}\dot{\chi}(t)e^{-\boldsymbol{k}\chi(t)}\boldsymbol{j}^{-1}e^{\boldsymbol{k}\chi(t)}e^{-\boldsymbol{i}\theta(t)}\Big\} + \dot{\varphi}(t) \\
=& \dot{\varphi}(t) + \dot{a}(t)\sin 2\chi(t).
\end{aligned}
\tag{A.13}
$$

The same procedure is used to compute the first moment of the spectral polarization density, such that

$$
\begin{aligned}
\int \omega \left|Z_{\mathbb{H}}(\omega)\right|^2 \mathrm{d}\omega &= \int \omega Z_{\mathbb{H}}(\omega)\overline{Z_{\mathbb{H}}(\omega)}\mathrm{d}\omega \\
&= \int \mathcal{F}\left\{\dot{z}_{\mathbb{H}}\right\}(\omega)\boldsymbol{j}^{-1}\boldsymbol{j}^{-1}\overline{Z_{\mathbb{H}}(\omega)}\boldsymbol{j}\mathrm{d}\omega \\
&= \int \mathcal{F}\left\{\dot{z}_{\mathbb{H}}\right\}(\omega)\overline{Z_{\mathbb{H}}(\omega)}\mathrm{d}\omega\boldsymbol{j}^{-1} \\
&= \int \dot{z}_{\mathbb{H}}(t)\overline{z_{\mathbb{H}}(t)}\mathrm{d}t\boldsymbol{j}^{-1} \\
&= \int \dot{z}_{\mathbb{H}}(t)\left(z_{\mathbb{H}}(t)\right)^{-1}\left|z_{\mathbb{H}}(t)\right|^2\mathrm{d}t\boldsymbol{j}^{-1}.
\end{aligned}
\tag{A.14}
$$

Denoting $P_{\mathrm{span}\{\mathbf{1},i,\boldsymbol{k}\}}$ the projection operator on the axes $\mathbf{1}$, $\boldsymbol{i}$

and $\boldsymbol{k}$, we compute $\nu_z(t)$ such as

$$
\begin{aligned}
\nu_z(t) =& P_{\text{span}\{\mathbf{1},\boldsymbol{i},\boldsymbol{k}\}} \left\{ \dot{z}_{\mathbb{H}}(t) \left(z_{\mathbb{H}}(t)\right)^{-1} \boldsymbol{j}^{-1} \right\} \\
=& P_{\text{span}\{\mathbf{1},\boldsymbol{i},\boldsymbol{k}\}} \Big\{ \Big(\dot{a}(t) e^{\boldsymbol{i}\theta(t)} e^{-\boldsymbol{k}\chi(t)} e^{j\varphi(t)} + a(t)\boldsymbol{i}\dot{a}(t) e^{\boldsymbol{i}\theta(t)} e^{-\boldsymbol{k}\chi(t)} e^{j\varphi(t)} \\
& + a(t) e^{\boldsymbol{i}\theta(t)} \boldsymbol{k}^{-1} \dot{\chi}(t) e^{-\boldsymbol{k}\chi(t)} e^{j\varphi(t)} + a(t) e^{\boldsymbol{i}\theta(t)} e^{-\boldsymbol{k}\chi(t)} \boldsymbol{j}\dot{\varphi}(t) e^{j\varphi(t)} \Big) \\
& \times a^{-1}(t) e^{-j\varphi(t)} e^{\boldsymbol{k}\chi(t)} e^{-\theta(t)} \boldsymbol{j}^{-1} \Big\} \\
=& P_{\text{span}\{\mathbf{1},\boldsymbol{i},\boldsymbol{k}\}} \Big\{ -\frac{\dot{a}(t)}{a(t)} \boldsymbol{j} - \dot{a}(t)\boldsymbol{k} - \boldsymbol{i}\dot{\chi}(t)\cos 2\theta(t) + \dot{\chi}(t)\sin 2\theta(t) \\
& + \dot{\varphi}(t) e^{\boldsymbol{i}\theta(t)} e^{-2\boldsymbol{k}\chi(t)} e^{\boldsymbol{i}\theta(t)} \Big\} \\
=& \dot{\varphi}(t) s_1(t) + \dot{\chi}(t)\sin 2\theta(t) + \boldsymbol{i}\left(\dot{\varphi}(t) s_2(t) - \dot{\chi}(t)\cos 2\theta(t)\right) \\
& - \boldsymbol{k}\left(\dot{\varphi}(t) s_3(t) + \dot{a}(t)\right).
\end{aligned}
\tag{A.15}
$$

B The spin-weighted spherical functions

B.1 Spin weighted functions

Spin-weighted spherical functions are functions of both a point on the sphere and a choice of frame in the tangent space at this point [97]. A Hilbert basis of the s spin-weighted square integrable functions on the unit sphere is given by the s-spin-weighted spherical harmonics. Applications of spin-weighted spherical functions are found in gravitational-wave astronomy [25] [98] and cosmic microwave background measurement [99].

[97]: Boyle (2016), *How should spin-weighted spherical functions be defined?*

[98]: Boyle (2013), *Angular velocity of gravitational radiation from precessing binaries and the corotating frame*

[99]: Marinucci et al. (2011), *Random Fields on the Sphere: Representation, Limit Theorems and Cosmological Applications*

Let be f a function defined on a space of dimension three with the norm associated to the Euclidean scalar product. For a given direction represented by the unit vector n, we consider an orthonormal basis formed with the right-handed triplet (a, b, n). For v a rotation angle with respect to n, and a vector $m = (a + \boldsymbol{i} b)/\sqrt{2}$, we define the rotated complex vector $m_v = e^{\boldsymbol{i} s v} m$. Then f is said to be of spin weight s if it transforms as

$$f(m_v, n) = e^{\boldsymbol{i} s v} f(m, n). \tag{B.1}$$

For instance, denoting $h(t) = h_+(t) + \boldsymbol{i} h_\times(t)$ the gravitational waveform defined for a zero polarization angle (see Section 2.2.1) and $h_\psi(t)$ the one defined for a polarization angle ψ, then

$$h_\psi(t) = e^{-2\boldsymbol{i}\psi} h(t). \tag{B.2}$$

Which came from the definition of the waveform h as a spin weighted function with $s = -2$.

We refer to [97, 98] [100] for a detailed introduction to spin weighted spherical functions and spin weighted spherical harmonics.

[100]: Torres del Castillo (2003), *3-D Spinors, Spin-Weighted Functions and their Applications*

B.2 Wigned D-matrices

Wigner D-matrices [101] form an irreducible representation of the rotation groups $SU(2)$ and $SO(3)$ with finite dimensional matrices.

[101]: Wigner (1960), *Group Theory and Its Application to the Quantum Mechanics of Atomic Spectra*

The Wigner D-matrices are given by

$$D^l_{m,m'}(\alpha,\beta,\gamma) = e^{im'\alpha} d^l_{m,m'}(\beta) e^{im\gamma}, \tag{B.3}$$

where $d^l_{m,m'}(\beta)$ is the Wigner d-matrix defined as

$$\begin{aligned} d^l_{m,m'}(\beta) = \sum_n (-1)^n \frac{\sqrt{(l+m)!(l-m)!(l+m')!(l-m')!}}{(l+m-n)!n!(l-m'-n)!(n-m+m')!} \\ \times \left(\cos\frac{\beta}{2}\right)^{2l-2n+m-m'} \left(\sin\frac{\beta}{2}\right)^{2n+m'-m} \end{aligned} \tag{B.4}$$

where n belongs to $\max(0, m-m') \leqslant n \leqslant \min(l+m, l-m')$.

For example we get

$$d^2_{2,2}(\beta) = \cos^4\frac{\beta}{2} \quad \text{and} \quad d^2_{-2,2}(\beta) = \sin^4\frac{\beta}{2} \tag{B.5}$$

that are used in the computation of $\mathfrak{h}_{2,2}(t)$ in Chapter 4. Other Wigner d-matrices defined whith the same conventions can be found in [102]. In particular, the relation

$$d^l_{-m,-m'}(\beta) = (-1)^{m-m'} d^l_{m,m'}(\beta) = d^l_{m',m}(\beta) \tag{B.6}$$

allows to retrieve additional Wigner d-matrices.

[102]: Pratten et al. (2021), *Computationally efficient models for the dominant and subdominant harmonic modes of precessing binary black holes*

B.3 Spin-weighted spherical harmonics

Spin-weighted spherical harmonics are a special case of Wigner D-matrices forming a basis of spin weighted functions on the sphere [103]. For a given function $f(\iota, \varphi_0)$, the spin weighted spherical harmonics expansion takes the form[1]

$$f(\iota,\varphi_0) = \sum_{l,m} f_{l,m}\, {}_{-s}Y_{l,m}(\iota,\varphi_0), \tag{B.7}$$

such as what is used to compute gravitational waveforms.

Our conventions of spin weighted spherical harmonics and Wigner d-matrices are in accordance with [104]. This leads to the definition of the spin weighted spherical harmonics as

$${}_{-s}Y_{l,m}(\iota,\varphi_0) = (-1)^s \sqrt{\frac{2l+1}{4\pi}} d^l_{m,s}(\iota) e^{im\varphi_0}, \tag{B.8}$$

where the $d^l_{m,s}(\iota)$ are the Wigner d-matrices.

[103]: Goldberg et al. (1967), *Spin-s Spherical Harmonics and ð*

1: As for the spin weighted functions introduced in Appendix B.1, the spin weighted spherical harmonics are functions on the sphere whose position is given by (ι, φ_0). The tangent basis is fixed by convention with a rotation angle equal to zero.

[104]: Ajith et al. (2007), *Data formats for numerical relativity waves*

For a rotation parametrized by the triplet (α, β, γ), one can rotate to the spin weighted spherical harmonics as [98]

$$ {}_{-s}Y_{l,m}(\Theta(t)) = \sum_{m'=-l}^{l} D^{l}_{m,m'}(\alpha, \beta, \gamma) {}_{-s}Y_{l,m'}(\iota, \varphi_0). \tag{B.9} $$

A sample of spin weighted spherical harmonics is given in Table B.1 for $s = 2$ and $l = 2$. Those are used in the computation of the dominant polarized component $\mathfrak{h}_{2,2}$ presented in Section 4.3.3.

m	${}_{-2}Y_{2,m}(\iota, \varphi_0)$
2	$\frac{1}{8}\sqrt{\frac{5}{\pi}}(1+\cos\iota)^2 e^{2i\varphi}$
1	$\frac{1}{4}\sqrt{\frac{5}{\pi}}(1+\cos\iota)\sin\iota\, e^{i\varphi}$
0	$\frac{\sqrt{6}}{8}\sqrt{\frac{5}{\pi}}\sin^2\iota$
−1	$\frac{1}{4}\sqrt{\frac{5}{\pi}}(1-\cos\iota)\sin\iota\, e^{-i\varphi}$
−2	$\frac{1}{8}\sqrt{\frac{5}{\pi}}(1-\cos\iota)^2 e^{-2i\varphi}$

Table B.1: Spin weighted spherical harmonics ${}_{-2}Y_{2,m}$ for $m = -2, -1, 0, 1, 2$.

B.4 Development of polarized components

In order to prove (4.34), we need to verify that $\mathfrak{h}_{l,m}(t, \Theta(t))$ is such that

$$ \mathfrak{h}_{l,m}(t; \Theta(t)) = \mathfrak{h}_{l,m}(t; \varphi_0 + \alpha(t), \iota, \beta(t), \varphi_{l,m}(t) - m\gamma(t)). \tag{B.10} $$

This is done by developing the expression of $\mathfrak{h}_{l,m}$ from (4.29). It is known that for any couple (l, m), one have $h^{P}_{l,m}(t) = a_{l,m}(t)e^{-i\varphi_{l,m}(t)}$ and $h^{P}_{l,-m}(t) = (-1)^l a_{l,m}(t)e^{i\varphi_{l,m}(t)}$. The latter is the only assumption needed to compute the instantaneous Stokes parameters and instantaneous frequency in Section 4.3.2.

From the definition of -2 spin weighted spherical harmonics

and Wigner D-matrices in Appendices B.2 and B.3, we get

$$\begin{aligned}
\mathfrak{h}_{l,m}(t) =& h^P_{l,m}(t)\,{}_{-2}Y_{l,m}(\Theta(t)) + h^P_{l,-m}(t)\,{}_{-2}Y_{l,-m}(\Theta(t)) \\
=& a_{l,m}(t) \sum_{m'=-l}^{l} \Big[e^{-\boldsymbol{i}\varphi_{l,m}(t)} D^l_{m,m'}(\alpha(t),\beta(t),\gamma(t))\,{}_{-2}Y_{l,m'}(\iota,\varphi_0) \\
&+ (-1)^l e^{\boldsymbol{i}\varphi_{l,m}(t)} D^l_{-m,m'}(\alpha(t),\beta(t),\gamma(t))\,{}_{-2}Y_{l,m'}(\iota,\varphi_0) \Big] \\
=& a_{l,m}(t) \sqrt{\frac{2l+1}{4\pi}} \sum_{m'=-l}^{l} d^l_{m',2}(\iota) \\
&\times \Big[e^{-\boldsymbol{i}(\varphi_{l,m}(t)-m\gamma(t))} e^{\boldsymbol{i}m'(\alpha(t)+\varphi_0)} d^l_{m,m'}(\beta(t)) \\
&+ (-1)^l e^{\boldsymbol{i}(\varphi_{l,m}(t)-m\gamma(t))} e^{\boldsymbol{i}m'(\alpha(t)+\varphi_0)} d^l_{-m,m'}(\beta(t)) \Big].
\end{aligned} \tag{B.11}$$

The rest of the demonstration consists in applying the Hilbert transform to (B.11).

Bibliography

[1] Christian Brosseau. *Fundamentals of polarized light : a statistical optics approach*. eng. New York [etc: John Wiley Sons, 1998 (cited on pages 4, 6, 15, 84, 110).

[2] Peter J. Schreier and Louis L. Scharf. *Statistical Signal Processing of Complex-Valued Data: The Theory of Improper and Noncircular Signals*. Cambridge University Press, 2010 (cited on pages 4, 21).

[3] Julien Flamant. 'A general approach for the analysis and filtering of bivariate signals'. 2018 (cited on pages 4, 6, 9, 11–14, 17, 22, 25, 28, 30, 105, 106, 109, 115, 117).

[4] R. McAulay and T. Quatieri. 'Speech analysis/Synthesis based on a sinusoidal representation'. In: *IEEE Transactions on Acoustics, Speech, and Signal Processing* 34.4 (1986), pp. 744–754. DOI: 10.1109/TASSP.1986.1164910 (cited on page 7).

[5] Patrick Flandrin. *Explorations in Time-Frequency Analysis*. Cambridge University Press, 2018 (cited on pages 7, 8).

[6] Bernard Picinbono. 'On Instantaneous Amplitude and Phase of Signals'. In: *IEEE Transactions on Signal Processing* 45 (1997), pp. 552–560 (cited on pages 8, 15, 17, 18).

[7] Julien Flamant, Nicolas Le Bihan, and Pierre Chainais. 'Time–frequency analysis of bivariate signals'. In: *Applied and Computational Harmonic Analysis* 46.2 (2019), pp. 351–383. DOI: https://doi.org/10.1016/j.acha.2017.05.007 (cited on pages 10, 12–14, 17, 27, 46, 107, 109).

[8] J. M. Lilly and J.-C. Gascard. 'Wavelet ridge diagnosis of time-varying elliptical signals with application to an oceanic eddy'. In: *Nonlinear Processes in Geophysics* 13.5 (2006), pp. 467–483. DOI: 10.5194/npg-13-467-2006 (cited on pages 11, 17, 21, 27, 109).

[9] Leon Cohen, Patrick Loughlin, and David Vakman. 'On an ambiguity in the definition of the amplitude and phase of a signal'. In: *Signal Processing* 79.3 (1999), pp. 301–307. DOI: https://doi.org/10.1016/S0165-1684(99)00103-6 (cited on page 12).

[10] Jonathan M. Lilly and Sofia C. Olhede. 'Bivariate Instantaneous Frequency and Bandwidth'. In: *IEEE Transactions on Signal Processing* 58.2 (2010), pp. 591–603. DOI: 10.1109/TSP.2009.2031729 (cited on pages 17, 21, 27, 109).

[11] Evan G. Hemingway and Oliver M. O'Reilly. 'Perspectives on Euler angle singularities, gimbal lock, and the orthogonality of applied forces and applied moments'. In: *Multibody System Dynamics* 44 (2018), pp. 31–56. DOI: 10.1007/s11044-018-9620-0 (cited on page 18).

[12] Jonathan M. Lilly and Sofia C. Olhede. 'Analysis of Modulated Multivariate Oscillations'. In: *IEEE Transactions on Signal Processing* 60.2 (2012), pp. 600–612. DOI: 10.1109/TSP.2011.2173681 (cited on pages 22, 25–28, 30, 46, 109).

[13] Todd Ell, Nicolas Le Bihan, and Stephen Sangwine. *Quaternion Fourier Transforms for Signal and Image Processing*. Wiley-ISTE, May 2014, p. 160 (cited on pages 22–24, 113).

[14] J Ville. 'Théorie et Applications de la Notion de Signal Analytique'. In: *Câbles et Transmissions* 2 A (1) (1948), pp. 61–74 (cited on pages 25, 28).

[15] L. Marple. 'Computing the discrete-time "analytic" signal via FFT'. In: *IEEE Transactions on Signal Processing* 47.9 (1999), pp. 2600–2603. DOI: 10.1109/78.782222 (cited on pages 25, 117, 118).

[16] N. Delprat et al. 'Asymptotic wavelet and Gabor analysis: extraction of instantaneous frequencies'. In: *IEEE Transactions on Information Theory* 38.2 (1992), pp. 644–664. DOI: 10.1109/18.119728 (cited on page 25).

[17] Peter Petersen. *Riemannian Geometry*. Third. Springer Cham, 2016 (cited on page 31).

[18] B. P. Abbott et al. 'Observation of Gravitational Waves from a Binary Black Hole Merger'. In: *Phys. Rev. Lett.* 116 (6 2016), p. 061102. DOI: 10.1103/PhysRevLett.116.061102 (cited on pages 32, 39, 42, 79).

[19] R. Abbott et al. 'GWTC-3: Compact Binary Coalescences Observed by LIGO and Virgo During the Second Part of the Third Observing Run'. In: (Nov. 2021) (cited on pages 32, 39, 42).

[20] R. Abbott et al. 'GWTC-2: Compact binary coalescences observed by LIGO and Virgo during the first half of the 3rd observing run'. arXiv:2010.14527. 2020 (cited on page 32).

[21] A. Buonanno and T. Damour. 'Effective one-body approach to general relativistic two-body dynamics'. In: *Phys. Rev. D* 59 (8 Mar. 1999), p. 084006. DOI: 10.1103/PhysRevD.59.084006 (cited on pages 32, 53, 109).

[22] A. Einstein. 'Die Grundlage der allgemeinen Relativitätstheorie'. In: *Das Relativitätsprinzip: Eine Sammlung von Abhandlungen*. Wiesbaden: Vieweg+Teubner Verlag, 1923, pp. 81–124. DOI: 10.1007/978-3-663-19510-8_7 (cited on page 32).

[23] Albert A. Michelson and Edward W. Morley. 'LVIII. On the relative motion of the earth and the luminiferous Æther'. In: *The London, Edinburgh, and Dublin Philosophical Magazine and Journal of Science* 24.151 (1887), pp. 449–463. DOI: 10.1080/14786448708628130 (cited on page 32).

[24] T Accadia et al. 'Virgo: a laser interferometer to detect gravitational waves'. In: *Journal of Instrumentation* 7.03 (2012), P03012–P03012. DOI: 10.1088/1748-0221/7/03/p03012 (cited on page 35).

[25] M. Maggiore. *Gravitational Waves: Volume 1: Theory and Experiments*. OUP Oxford, 2007 (cited on pages 36, 39, 44, 45, 123).

[26] F. Acernese et al. 'Advanced Virgo: a second-generation interferometric gravitational wave detector'. In: *Class. Quant. Grav.* 32.2 (2015), p. 024001. DOI: 10.1088/0264-9381/32/2/024001 (cited on page 38).

[27] F. Acernese et al. 'Advanced Virgo Status'. In: *Journal of Physics: Conference Series* 1342.1 (2020), p. 012010. DOI: 10.1088/1742-6596/1342/1/012010 (cited on page 38).

[28] T Accadia et al. *Advanced Virgo Technical Design Report*. Tech. rep. VIR-0128A-12. Virgo Technical documentation system, 2012 (cited on page 38).

[29] B. P. Abbott et al. 'Prospects for observing and localizing gravitational-wave transients with Advanced LIGO, Advanced Virgo and KAGRA'. In: *Living Reviews in Relativity* 23.3 (t 2020), pp. 1433–8351. DOI: 10.1007/s41114-020-00026-9 (cited on pages 40, 41).

[30] Stephen Fairhurst. 'Localization of transient gravitational wave sources: beyond triangulation'. In: *Classical and Quantum Gravity* 35.10 (2018), p. 105002. DOI: 10.1088/1361-6382/aab675 (cited on page 41).

[31] B. P. Abbott et al. 'GW170817: Observation of Gravitational Waves from a Binary Neutron Star Inspiral'. In: *Phys. Rev. Lett.* 119 (16 Oct. 2017), p. 161101. DOI: 10.1103/PhysRevLett.119.161101 (cited on page 43).

[32] B. P. Abbott et al. 'Multi-messenger Observations of a Binary Neutron Star Merger'. In: *ApJ* 848.2 (2017), p. L12. DOI: 10.3847/2041-8213/aa91c9 (cited on page 43).

[33] B. P. Abbott et al. 'A gravitational-wave standard siren measurement of the Hubble constant'. In: *Nature* 551.7678 (Nov. 2017), pp. 85–88. DOI: 10.1038/nature24471 (cited on page 43).

[34] B. P. Abbott et al. 'Tests of General Relativity with GW170817'. In: *Phys. Rev. Lett.* 123 (1 July 2019), p. 011102. DOI: 10.1103/PhysRevLett.123.011102 (cited on page 43).

[35] R. Abbott et al. 'Observation of Gravitational Waves from Two Neutron Star–Black Hole Coalescences'. In: *The Astrophysical Journal Letters* 915.1 (2021), p. L5. DOI: 10.3847/2041-8213/ac082e (cited on page 43).

[36] R. Abbott et al. 'GW190412: Observation of a binary-black-hole coalescence with asymmetric masses'. In: *Phys. Rev. D* 102 (4 Aug. 2020), p. 043015. DOI: 10.1103/PhysRevD.102.043015 (cited on pages 43, 101).

[37] Chase Kimball et al. 'Evidence for Hierarchical Black Hole Mergers in the Second LIGO–Virgo Gravitational Wave Catalog'. In: *The Astrophysical Journal Letters* 915.2 (2021), p. L35. DOI: 10.3847/2041-8213/ac0aef (cited on page 47).

[38] The LIGO Scientific Collaboration, The Virgo Collaboration, and The KAGRA Collaboration. 'Tests of general relativity with GWTC-3'. English. In: *Physical Review D (Particles, Fields, Gravitation and Cosmology)* (Apr. 2022). Not yet published as of 06/06/2022 (cited on page 47).

[39] The LIGO Scientific Collaboration, The Virgo Collaboration, and The KAGRA Collaboration. 'The population of merging compact binaries inferred using gravitational waves through GWTC-3'. In: *arXiv e-prints*, arXiv:2111.03634 (Nov. 2021), arXiv:2111.03634 (cited on page 47).

[40] S Klimenko and G Mitselmakher. 'A wavelet method for detection of gravitational wave bursts'. In: *Classical and Quantum Gravity* 21.20 (2004), S1819–S1830. DOI: 10.1088/0264-9381/21/20/025 (cited on pages 48, 86).

[41] S. Klimenko et al. 'Method for detection and reconstruction of gravitational wave transients with networks of advanced detectors'. In: *Phys. Rev. D* 93 (4 Feb. 2016), p. 042004. DOI: 10.1103/PhysRevD.93.042004 (cited on pages 48, 86, 87, 109).

[42] Samantha A Usman et al. 'The PyCBC search for gravitational waves from compact binary coalescence'. In: *Classical and Quantum Gravity* 33.21 (2016), p. 215004. DOI: 10.1088/0264-9381/33/21/215004 (cited on pages 48, 50).

[43] Kipp Cannon et al. 'Toward early detection of gravitational waves from compact binary coalescence'. In: *The Astrophysical Journal* 748.2 (2012), p. 136. DOI: 10.1088/0004-637x/748/2/136 (cited on page 48).

[44] Neil J Cornish and Tyson B Littenberg. 'Bayeswave: Bayesian inference for gravitational wave bursts and instrument glitches'. In: *Classical and Quantum Gravity* 32.13 (2015), p. 135012. DOI: 10.1088/0264-9381/32/13/135012 (cited on page 50).

[45] E. Thrane and C. Talbot. 'An introduction to Bayesian inference in gravitational-wave astronomy: Parameter estimation, model selection, and hierarchical models'. In: *PASA* 36 (2019), e010. DOI: 10.1017/pasa.2019.2 (cited on pages 50, 64).

[46] J. Veitch et al. 'Parameter estimation for compact binaries with ground-based gravitational-wave observations using the LALInference software library'. In: *Phys. Rev. D* 91 (4 Feb. 2015), p. 042003. DOI: 10.1103/PhysRevD.91.042003 (cited on page 50).

[47] Yi Pan et al. 'Inspiral-merger-ringdown waveforms of spinning, precessing black-hole binaries in the effective-one-body formalism'. In: *Phys. Rev. D* 89 (8 Apr. 2014), p. 084006. DOI: 10.1103/PhysRevD.89.084006 (cited on pages 51, 95, 96).

[48] M Mapelli. 'Binary Black Hole Mergers: Formation and Populations'. In: *Front. Astron. Space Sci.* 7:38 (2020). DOI: 10.3389/fspas.2020.00038 (cited on page 51).

[49] Carl L. Rodriguez et al. 'Illuminating black hole binary formation channels with spins in advanced LIGO'. In: *The Astrophysical Journal* 832.1 (2016), p. L2. DOI: 10.3847/2041-8205/832/1/l2 (cited on pages 51, 101).

[50] Davide Gerosa et al. 'Spin orientations of merging black holes formed from the evolution of stellar binaries'. In: *Phys. Rev. D* 98 (8 Oct. 2018), p. 084036. DOI: 10.1103/PhysRevD.98.084036 (cited on pages 51, 101).

[51] Serguei Ossokine et al. 'Multipolar effective-one-body waveforms for precessing binary black holes: Construction and validation'. In: *Phys. Rev. D* 102 (4 Aug. 2020), p. 044055. DOI: 10.1103/PhysRevD.102.044055 (cited on pages 52, 71, 96).

[52] LIGO Scientific Collaboration. *LIGO Algorithm Library - LALSuite*. DOI: 10.7935/GT1W-FZ16. 2018 (cited on pages 52, 59, 63).

[53] Patricia Schmidt. 'Gravitational Waves From Binary Black Hole Mergers: Modeling and Observations'. In: *Frontiers in Astronomy and Space Sciences* 7 (2020). DOI: 10.3389/fspas.2020.00028 (cited on pages 52, 56, 58, 60).

[54] Luc Blanchet. 'Gravitational Radiation from Post-Newtonian Sources and Inspiralling Compact Binaries'. In: *Living Reviews in Relativity* 17.2 (2014), pp. 1433–8351. DOI: 10.12942/lrr-2014-2 (cited on page 53).

[55] M. Boyle et al. 'The SXS collaboration catalog of binary black hole simulations'. In: *Class. Quantum Grav.* 36.19 (2019), p. 195006. DOI: 10.1088/1361-6382/ab34e2 (cited on page 53).

[56] Tanja Hinderer and Stanislav Babak. 'Foundations of an effective-one-body model for coalescing binaries on eccentric orbits'. In: *Phys. Rev. D* 96 (10 Nov. 2017), p. 104048. DOI: 10.1103/PhysRevD.96.104048 (cited on page 53).

[57] P Ajith et al. 'A phenomenological template family for black-hole coalescence waveforms'. In: *Classical and Quantum Gravity* 24.19 (2007), S689–S699. DOI: 10.1088/0264-9381/24/19/s31 (cited on page 53).

[58] Alejandro Bohé et al. 'Improved effective-one-body model of spinning, nonprecessing binary black holes for the era of gravitational-wave astrophysics with advanced detectors'. In: *Phys. Rev. D* 95 (4 Feb. 2017), p. 044028. DOI: 10.1103/PhysRevD.95.044028 (cited on pages 54–56, 58, 63, 90).

[59] K. Chatziioannou et al. 'Constructing Gravitational Waves from Generic Spin-Precessing Compact Binary Inspirals'. In: *Phys. Rev. D* 95.10 (2017), p. 104004. DOI: 10.1103/PhysRevD.95.104004 (cited on page 55).

[60] The LIGO Scientific Collaboration, The Virgo Collaboration, and The KAGRA Collaboration. 'GWTC-3: Compact Binary Coalescences Observed by LIGO and Virgo During the Second Part of the Third Observing Run'. In: *arXiv e-prints*, arXiv:2111.03606 (Nov. 2021), arXiv:2111.03606 (cited on page 55).

[61] M. Pürrer. 'Frequency domain reduced order model of aligned-spin effective-one-body waveforms with generic mass-ratios and spins'. In: *Phys. Rev. D* 93.6 (2016), p. 064041. DOI: 10.1103/PhysRevD.93.064041 (cited on page 56).

[62] B. D. Lackey et al. 'Surrogate model for an aligned-spin effective one body waveform model of binary neutron star inspirals using Gaussian process regression'. In: *Phys. Rev. D* 100.2 (2019), p. 024002. DOI: 10.1103/PhysRevD.100.024002 (cited on page 56).

[63] S. Schmidt et al. 'Machine learning gravitational waves from binary black hole mergers'. In: *Phys. Rev. D* 103 (4 2021), p. 043020. DOI: 10.1103/PhysRevD.103.043020 (cited on pages 56–60, 62, 63).

[64] S. Khan and R. Green. 'Gravitational-wave surrogate models powered by artificial neural networks'. In: *Phys. Rev. D* 103 (6 Mar. 2021), p. 064015. DOI: 10.1103/PhysRevD.103.064015 (cited on page 56).

[65] A. J. K. Chua et al. 'Reduced-Order Modeling with Artificial Neurons for Gravitational-Wave Inference'. In: *Phys. Rev. Lett.* 122 (21 May 2019), p. 211101. DOI: 10.1103/PhysRevLett.122.211101 (cited on page 56).

[66] F. Pedregosa et al. 'Scikit-learn: Machine Learning in Python'. In: *J. Mach. Learn. Res.* 12 (2011), pp. 2825–2830 (cited on pages 57, 61).

[67] T. Hastie et al. *The elements of statistical learning*. 2nd. Springer, 2017 (cited on pages 57, 60, 71).

[68] Rich Abbott et al. 'Open data from the first and second observing runs of Advanced LIGO and Advanced Virgo'. In: *SoftwareX* 13 (2021), p. 100658. DOI: https://doi.org/10.1016/j.softx.2021.100658 (cited on pages 64, 90).

[69] Gregory Ashton et al. 'Bilby: A User-friendly Bayesian Inference Library for Gravitational-wave Astronomy'. In: *The Astrophysical Journal Supplement Series* 241.2 (2019), p. 27. DOI: 10.3847/1538-4365/ab06fc (cited on page 64).

[70] Lucy M. Thomas, Geraint Pratten, and Patricia Schmidt. 'Accelerating multimodal gravitational waveforms from precessing compact binaries with artificial neural networks'. In: (May 2022) (cited on page 70).

[71] Patricia Schmidt, Frank Ohme, and Mark Hannam. 'Towards models of gravitational waveforms from generic binaries: II. Modelling precession effects with a single effective precession parameter'. In: *Phys. Rev. D* 91 (2 Jan. 2015), p. 024043. DOI: 10.1103/PhysRevD.91.024043 (cited on page 72).

[72] Julien Flamant et al. 'Non-parametric characterization of gravitational-wave polarizations'. In: *2018 26th European Signal Processing Conference (EUSIPCO)*. 2018, pp. 2658–2662. DOI: 10.23919/EUSIPCO.2018.8552942 (cited on pages 79, 95, 109).

[73] S. Klimenko et al. 'Constraint likelihood analysis for a network of gravitational wave detectors'. In: *Phys. Rev. D* 72 (12 Dec. 2005), p. 122002. DOI: 10.1103/PhysRevD.72.122002 (cited on pages 81, 86–88).

[74] Ralph A. Willoughby. 'Solutions of Ill-Posed Problems (A. N. Tikhonov and V. Y. Arsenin)'. In: *SIAM Review* 21.2 (1979), pp. 266–267. DOI: 10.1137/1021044 (cited on page 87).

[75] Jose Gil and Razvigor Ossikovski. *Polarized Light and the Mueller Matrix Approach*. 2nd Edition. 2022, p. 516 (cited on page 87).

[76] Quentin Bammey et al. 'Sparse Time-Frequency Representation of Gravitational-Wave signals in Unions of Wilson Bases'. In: *2018 26th European Signal Processing Conference (EUSIPCO)*. 2018, pp. 1755–1759. DOI: 10.23919/EUSIPCO.2018.8553079 (cited on page 88).

[77] Amir Beck and Marc Teboulle. 'A Fast Iterative Shrinkage-Thresholding Algorithm for Linear Inverse Problems'. In: *SIAM Journal on Imaging Sciences* 2.1 (2009), pp. 183–202. DOI: 10.1137/080716542 (cited on page 89).

[78] Patrick L. Combettes and Valérie R. Wajs. 'Signal Recovery by Proximal Forward-Backward Splitting'. In: *Multiscale Modeling & Simulation* 4.4 (2005), pp. 1168–1200. DOI: 10.1137/050626090 (cited on page 89).

[79] Matthieu Kowalski and Bruno Torrésani. 'Structured Sparsity: from Mixed Norms to Structured Shrinkage'. In: *SPARS'09 - Signal Processing with Adaptive Sparse Structured Representations*. Ed. by Rémi Gribonval. Inria Rennes - Bretagne Atlantique. Saint Malo, France, Apr. 2009 (cited on page 89).

[80] Matthieu Kowalski, Kai Siedenburg, and Monika Dörfler. 'Social Sparsity! Neighborhood Systems Enrich Structured Shrinkage Operators'. In: *IEEE Transactions on Signal Processing* 61.10 (2013), pp. 2498–2511. DOI: 10.1109/TSP.2013.2250967 (cited on page 89).

[81] Facundo Costa et al. 'Bayesian EEG source localization using a structured sparsity prior'. In: *NeuroImage* 144 (2017), pp. 142–152. DOI: https://doi.org/10.1016/j.neuroimage.2016.08.064 (cited on page 89).

[82] Kui Jia, Tsung-Han Chan, and Yi Ma. 'Robust and Practical Face Recognition via Structured Sparsity'. In: *Computer Vision – ECCV 2012*. Ed. by Andrew Fitzgibbon et al. Berlin, Heidelberg: Springer Berlin Heidelberg, 2012, pp. 331–344 (cited on page 89).

[83] Kai Siedenburg, Matthieu Kowalski, and Monika Dörfler. 'Audio declipping with social sparsity'. In: *2014 IEEE International Conference on Acoustics, Speech and Signal Processing (ICASSP)*. 2014, pp. 1577–1581. DOI: 10.1109/ICASSP.2014.6853863 (cited on pages 89, 90).

[84] Fangchen Feng et al. 'Structured sparsity regularization for gravitational- wave polarization reconstruction'. In: *2018 26th European Signal Processing Conference (EUSIPCO)*. 2018, pp. 1750–1754. DOI: 10.23919/EUSIPCO.2018.8553009 (cited on page 89).

[85] Stanislav Babak, Andrea Taracchini, and Alessandra Buonanno. 'Validating the effective-one-body model of spinning, precessing binary black holes against numerical relativity'. In: *Phys. Rev. D* 95 (2 Jan. 2017), p. 024010. DOI: 10.1103/PhysRevD.95.024010 (cited on page 99).

[86] Bernard F Schutz. 'Networks of gravitational wave detectors and three figures of merit'. In: *Classical and Quantum Gravity* 28.12 (2011), p. 125023. DOI: 10.1088/0264-9381/28/12/125023 (cited on page 103).

[87] Jonathan E. Thompson et al. 'Modeling the gravitational wave signature of neutron star black hole coalescences'. In: *Phys. Rev. D* 101 (12 June 2020), p. 124059. DOI: 10.1103/PhysRevD.101.124059 (cited on page 108).

[88] Neil J. Cornish. 'Time-frequency analysis of gravitational wave data'. In: *Phys. Rev. D* 102 (12 Dec. 2020), p. 124038. DOI: 10.1103/PhysRevD.102.124038 (cited on page 108).

[89] V Necula, S Klimenko, and G Mitselmakher. 'Transient analysis with fast Wilson-Daubechies time-frequency transform'. In: *Journal of Physics: Conference Series* 363 (2012), p. 012032. DOI: 10.1088/1742-6596/363/1/012032 (cited on page 109).

[90] Archana Pai, Éric Chassande-Mottin, and Olivier Rabaste. 'Best network chirplet chain: Near-optimal coherent detection of unmodeled gravitational wave chirps with a network of detectors'. In: *Phys. Rev. D* 77 (6 Mar. 2008), p. 062005. DOI: 10.1103/PhysRevD.77.062005 (cited on page 109).

[91] S. Mann and S. Haykin. 'The chirplet transform: physical considerations'. In: *IEEE Transactions on Signal Processing* 43.11 (1995), pp. 2745–2761. DOI: 10.1109/78.482123 (cited on page 111).

[92] Stphane Mallat. *A Wavelet Tour of Signal Processing, Third Edition: The Sparse Way*. 3rd. USA: Academic Press, Inc., 2008 (cited on page 111).

[93] Simon L Altmann. *Rotations, quaternions, and double groups; Corrected ed.* Dover Books on Mathematics. Mineola, N.Y: Dover Publ., 2005 (cited on page 113).

[94] James E. Jamison. 'Extension of some theorems of complex functional analysis to linear spaces over the quaternions and Cayley numbers'. PhD thesis. University of Missouri–Rolla, 1970 (cited on page 115).

[95] Alan V. Oppenheim and Ronald W. Schafer. *Discrete-Time Signal Processing*. 3rd. USA: Prentice Hall Press, 2009 (cited on pages 117–119).

[96] A. Reilly, G. Frazer, and B. Boashash. 'Analytic signal generation-tips and traps'. In: *IEEE Transactions on Signal Processing* 42.11 (1994), pp. 3241–3245. DOI: 10.1109/78.330385 (cited on pages 117–119).

[97] Michael Boyle. 'How should spin-weighted spherical functions be defined?' In: *Journal of Mathematical Physics* 57.9 (2016), p. 092504. DOI: 10.1063/1.4962723 (cited on page 123).

[98] Michael Boyle. 'Angular velocity of gravitational radiation from precessing binaries and the corotating frame'. In: *Phys. Rev. D* 87 (10 May 2013), p. 104006. DOI: 10.1103/PhysRevD.87.104006 (cited on pages 123, 125).

[99] Domenico Marinucci and Giovanni Peccati. *Random Fields on the Sphere: Representation, Limit Theorems and Cosmological Applications*. London Mathematical Society Lecture Note Series. Cambridge University Press, 2011 (cited on page 123).

[100] Gerardo Torres del Castillo. '3-D Spinors, Spin-Weighted Functions and their Applications'. In: (Jan. 2003). DOI: 10.1007/978-0-8176-8146-3 (cited on page 123).

[101] E. P. Wigner. 'Group Theory and Its Application to the Quantum Mechanics of Atomic Spectra'. In: *American Journal of Physics* 28.4 (1960), pp. 408–409. DOI: 10.1119/1.1935822 (cited on page 123).

[102] Geraint Pratten et al. 'Computationally efficient models for the dominant and subdominant harmonic modes of precessing binary black holes'. In: *Phys. Rev. D* 103.10 (2021), p. 104056. DOI: 10.1103/PhysRevD.103.104056 (cited on page 124).

[103] J. N. Goldberg et al. 'Spin-s Spherical Harmonics and ð'. In: *Journal of Mathematical Physics* 8.11 (1967), pp. 2155–2161. DOI: 10.1063/1.1705135 (cited on page 124).

[104] P. Ajith et al. *Data formats for numerical relativity waves*. 2007. DOI: 10.48550/ARXIV.0709.0093. URL: https://arxiv.org/abs/0709.0093 (cited on page 124).